

AD-A264 635

INTATION PAGE

Form Approved  
OMB No 0704-0188

Noted to average 1 hour per response, including the time for reviewing instructions, searching existing data sources, reviewing the collection of information, sending comments regarding this burden estimate or any other aspect of this burden, to Washington Headquarters Service, Directorate for Information Operations and Reports, 1215 Jefferson Office of Management and Budget, Paperwork Reduction Project (0704-0188), Washington, DC 20503

1. REPORT DATE Jan 93		3. REPORT TYPE AND DATES COVERED Interim Report, 1 Feb 92-31 Jan 93	
4. TITLE AND SUBTITLE Subpicosecond Electrooptic Sampling		5. FUNDING NUMBERS 2301/AS	
6. AUTHOR(S) David M. Bloom		7. PERFORMING ORGANIZATION NAME(S) AND ADDRESS Edward L. Ginzton Laboratory W. W. Hansen Laboratories of Physics Stanford University Stanford, CA 94305-4028	
8. PERFORMING ORGANIZATION REPORT NUMBER F49620-85-0016		9. SPONSORING / MONITORING AGENCY NAME(S) AND ADDRESS(ES) Department of the Air Force Air Force Office of Scientific Research (AFSC) Bolling Air Force Base, DC 20332-6448	
10. SPONSORING / MONITORING AGENCY REPORT NUMBER AFOSR-TR-93-0258		11. SUPPLEMENTARY NOTES	
12a. DISTRIBUTION / AVAILABILITY STATEMENT Unlimited		12b. DISTRIBUTION CODE	
13. ABSTRACT (Maximum 200 words) <p>The electro-optic sampling system developed under AFOSR contract no. F49620-85-0016 has been the workhorse for high speed measurements made in this lab. This report documents the continuing effort to improve this tool and highlights its most recent uses. In addition, we report the development of a time-lens, a new tool that gives us electronic control of the shape of optical pulses.</p> <p>The development of a time-lens has opened up a new field of research. It is a tool to electronically control the temporal characteristics of optical pulses just like glass lenses control the spatial characteristics. Our results to date include the creation of 7 ps pulses from a CW laser, active focusing (compression) of 55 ps pulses down to 2 ps, and demonstration of the time-reversal properties of time-lenses.</p> <p>A Ph.D. thesis detailing the Stanford time-lens and pulse compression experiments is included as an appendix.</p>			
14. SUBJECT TERMS Electro-optic sampling, time-lens, erbium doped fiber amplifiers			
15. PRICE CODE 13		16. PRICE CODE	
17. SECURITY CLASSIFICATION OF REPORT Unclassified		18. SECURITY CLASSIFICATION OF THIS PAGE Unclassified	
19. SECURITY CLASSIFICATION OF ABSTRACT Unclassified		20. LIMITATION OF ABSTRACT Unlimited	

93-10686



Edward L. Ginzton Laboratory  
W. W. Hansen Laboratories of Physics  
Stanford University  
Stanford, California 94305-4028

Interim Report  
to the  
Air Force Office of Scientific Research  
of  
a Program of Research  
in  
Subpicosecond Electrooptic Sampling  
Contract # F49620-92-J-0099

Principal Investigator:

David M. Bloom  
Associate Professor of Electrical Engineering

January 1993

Accession For	
NTIS CRA&I	<input checked="" type="checkbox"/>
DTIC TAB	<input checked="" type="checkbox"/>
Unannounced	<input type="checkbox"/>
Justification	
By	
Distribution /	
Availability Codes	
Dist	Avail and/or Special
A-1	

## **Summary**

The electro-optic sampling system developed under AFOSR contract no. F49620-85-0016 has been the workhorse for high speed measurements made in this lab. This report documents the continuing effort to improve this tool and highlights its most recent uses. In addition, we report the development of a time-lens, a new tool gives us electronic control of the shape of optical pulses.

Improvements to electro-optic sampling have been pursued in two areas, new techniques and new pulsed laser sources. In the area of new techniques, the idea of "slow optics - fast electronics", which uses a CW laser and high speed electrical receiver instead of a pulsed laser, has been explored. A slow optics system consisting of a 1.5  $\mu\text{m}$  laser diode and erbium doped fiber amplifier has been constructed and used to make electro-optic tests on GaAs circuits. It appears that the measurement sensitivity using this approach is not as good as originally believed, and is inferior to that possible with the original technique.

Our work towards an optical synthesizer, a broadly wavelength tunable and precisely controlled laser source has ended because of problems obtaining the fundamental building blocks of our proposed system.

In the area of new sources two ideas have been studied. The first is the use of erbium doped fiber lasers to produce short optical pulses, and the second, and more exciting is the development of a "time-lens" to control and focus the temporal shape of optical pulses.

The development of a time-lens has opened up a new field of research. It is a tool to electronically control the temporal characteristics of optical pulses just like glass lenses control the spatial characteristics. Our results to date include the creation of 7 ps pulses from a CW laser, active focusing (compression) of 55 ps pulses down to 2 ps, and demonstration of the time-reversal properties of time-lenses.

A PhD thesis detailing the Stanford time-lens and pulse compression experiments is included as an appendix.

## **REPORT**

### **The electro-optic sampling system as a useful tool**

The electro-optic sampling system has been used as a key tool in several research projects done by our group. It continues to be the workhorse for the majority of our high speed measurements. Several students are using the system to excite and measure the turn-on characteristics of short gate length MODFETs. Another student used the system to develop a high speed photodetector and microwave detector to build an optoelectronic autocorrelator. This system can replace conventional optical autocorrelators using second harmonic generation to measure short optical pulse widths down to 2 ps.

### **New Techniques for Electro-optic testing**

In order to build a more commercially practical electro-optic testing system, a new technique was pursued. This technique is a "slow optics - fast electronics" approach. In the conventional "fast optics - slow electronics" electro-optic sampling system, short optical pulses, and a slow photodetector are used to measure the GaAs circuit waveforms using equivalent time sampling. The drawback to this system is the complex laser needed to generate the short pulses. In the new approach, a simple, commercially available CW laser diode is used to probe the circuit under test. The laser is modulated directly by the circuit waveform, and the modulation is detected by a fast photodiode and electrical receiver. The advantage of this system is that it is less complex, and all components are commercially available. It was seen as a way of making electro-optic testing commercially feasible.

To test this idea, we built an electro-optic testing system around the laser diode and fast receiver. A key component to this system is an optical amplifier to boost optical signal level before photodetection. We built an erbium doped fiber amplifier with greater than 30dB of optical gain and good noise performance. The system was tested with an electrical spectrum analyzer as the electrical receiver. This would allow spectrum or frequency domain

characterization of the circuit under test. Such a receiver is characterized by a small electrical filter, so that the received noise level is minimized. The system performed as expected, with a bandwidth of 22GHz, limited by the photodetector and spectrum analyzer used as the receiver.

The more interesting type of system, and the type we have with the traditional approach, is one in which the time domain is measured. To build such a system, we used an electrical receiver which uses a sampler to measure the time domain. The fundamental problem to this type of system, and the one which prevented our system from working as originally hoped, is the increased receiver noise level in the sampling electrical receiver. The sampling receiver has an equivalent noise bandwidth which is many times larger than the noise bandwidth of the spectrum analyzer. This increased noise level overwhelms the received signal. Without major changes to the commercial sampling receiver, this approach to electro-optic sampling simply will not work.

Our work has lead us to the conclusion that the sampling process should be done with optics, rather than with electronics. While both techniques rely on mixing between the sampling pulses and circuit waveforms, there is a distinct advantage to doing this mixing in the optical domain. In the electrical sampling approach, the circuit waveform is imprinted on the CW laser beam. The sampling is done after the light beam has been detected; the photocurrent has an AC component proportional to the circuit voltage. The electrical sampling pulses turn a sampling bridge on and off to downconvert the frequency of the high speed fluctuations to a lower frequency. The key is that the sampling bridge is passive: the diodes in the sampling bridge are either conducting or not conducting. When the diodes are conducting, the RF line is connected to the IF line. The voltage on the IF side of the sampling bridge is never more than that on the RF side, and in practice is lower because of losses. Therefore, the amount of signal power converted to the IF side is proportional to the amount of time that the sampling switch is closed. The longer it is closed, the more power is transferred to the IF port. Since there is always a finite amount of noise in the IF circuitry, the signal to noise ratio at this port is proportional to the amount of time that the switch is closed. To get high time resolution, however, the switch should only be on for a

small amount of time. This is the fundamental limitation of sampling in the electrical domain: time resolution is maximized at the expense of signal to noise ratio.

The story is different when sampling in the optical domain. Here, the pulsed laser is modulated by the circuit voltage. The AC component of the detected photocurrent is proportional to the average optical power, and is independent of the pulse duration or repetition rate. Therefore, we can get more signal power by increasing the average optical power, and not suffer a loss in time resolution.

We conclude that in electro-optic testing systems, high time resolution measurements should be made by sampling with pulsed laser sources, rather than by sampling electrically. Later, we discuss a new measurement technique which may combine the high time resolution of electro-optic sampling with high spatial resolution.

### **New Sources**

We pursued two ideas to find new pulsed laser sources. The first was to build a pulsed laser source by modelocking an erbium doped fiber (EDF) laser. These EDF lasers could serve as compact pulsed sources at the 1.5 micron wavelength. We first characterized the pump absorption and gain of a heavily-doped EDF using a Ti-Sapphire laser and then assembled a one-meter-long EDF with a 100 mW, 980 nm pump diode laser. We achieved a 35% input coupling of pump light into the fiber, resulting in a CW output power of about 2 to 3 mW for a simple linear-cavity laser design. We proceeded to investigate other configurations such as those incorporating a fiber loop reflector. For optimal performance and large bandwidth, we discovered that fusion splices and a ring laser design were needed to minimize reflections. For our first efforts at mode-locking, we designed and developed a bulk-crystal  $\text{LiNbO}_3$  piezo-electric strain-optic (PESO) optical modulator. The PESO modulator could be operated at an acoustic resonance ranging from 1 to about 100 MHz and gave a maximum modulation of 10% for 1.55 micron light. For higher-speed mode-locked operation, we used a commercial 3-GHz integrated Mach-Zender fiber modulator. We generated 300 ps pulses at a 500 MHz repetition rate using a 14 m-

long, all-fiber ring laser (13.6 MHz fundamental resonance). The total average output power was about 1 mW.

The more interesting and fruitful approach to new sources led us into a new field of time-lenses.

### **Time Lens**

We have developed a tool which gives us electronic control over the temporal shape of optical pulses, much like a glass lens allows us to control the spatial shape of optical beams. This type of control has not been previously available, and should open a new field of research as all the capabilities of such a system are explored.

The theoretical basis for this type of system is the fact that the differential equations which describe propagation and diffraction of light beams are similar to those describing the dispersion of light pulses. This similarity has been known since the 1960's and led Kolner to complete the analogy between spatial diffraction and temporal dispersion. This analogy can be extended to include spatial lenses and time lenses. In this case, the temporal analog of a spatial lens ( which provides a spatially varying phase shift ) is a phase modulator ( which provides a time varying phase shift. ) It is relatively easy to build a strong spatial lens by grinding a more rounded glass surface. This results in many radians of phase shift across the face of the lens. It has been very difficult, however, to build phase modulators with much peak phase shift. The key to our work was the development of a new optical phase modulator which provides 13 radians of phase shift for 1W of microwave drive power.

The details of the space-time analogy and construction of our time lens are in the included Ph.D. thesis by Asif Godil, and are only summarized here. Our time lens is an optical phase modulator operating at 5.2GHz, producing a peak phase modulation of 13 radians for a microwave drive power of 1W, and 50 radians for 13W of microwave power.

After developing the time lens, we did experiments to confirm the analogy between space and time. We did the same operations on optical pulses that are done on spatial beams: focusing

and magnification. In the time domain, focusing a long pulse yields a short pulse, and magnifying a pulse with a single time lens yields a longer, time-reversed pulse.

We were able to focus the 55 ps pulses from a modelocked Nd:YAG laser to 6.7 ps with 1 W of microwave drive power, and 1.9 ps with 13 W of microwave power. These numbers match the calculated temporal resolution of the system. The focused pulse results are shown in Figure 1.

The time lens can also be used to create a pulse train from CW light. When used this way, the sinusoidal phase modulation can be thought of as a series of positive and negative time lenses, occurring at twice the microwave drive frequency. Since only the positive lenses can form pulses, the pulse repetition rate is the microwave drive frequency. With this technique, optical pulses can be generated from a CW laser without losing average power. In addition, the method is stable; since there is electronic control of the light. The results are easily predicted by simple theory, unlike laser modelocking, which still is largely an art form. Our results are shown in Figure 2. The pulses repeat at the 5.2 GHz microwave drive frequency. The measured pulse width is a detector limited 20 ps. The theoretical pulse width is 6.7 ps.

When focusing with a spatial lens, decentering the lens with respect to the object being focused should not affect the location of the focused spot. The temporal analogy means that pulse timing jitter should be removed when focusing. This experiment was done by focusing the 55 ps laser pulses to 6.7 ps and measuring the pulse timing jitter before and after focusing. The results are shown in Figure 3. Pulse timing jitter is reduced by an average of 80%. The fundamental limitation is lens aberration, caused by the fact that the phase modulator gives sinusoidal phase vs. time, when quadratic phase vs. time is the ideal.

### **Optical Synthesized Source**

We have stopped working in this area due to difficulties in obtaining the fundamental technology needed to build such a system. The idea was to use surface emitting lasers (SELs) to build an optical source tunable over 100 GHz with a kilohertz linewidth. SELs are a key



component because of their ability to smoothly tune wavelength, unlike distributed feedback lasers which undergo mode hops.

We collaborated with Sandia National Laboratories to build the SELs. We were not able to build lasers with uniform lasing characteristics such as laser threshold current. We have concluded that SEL technology is not yet mature enough to make the fundamental measurements needed to build the optical sweep synthesizer.

### **Related Work**

While our work to improve the electro-optic sampling system has been narrowed to the single, exciting topic of time-microscopy, additional work in our lab should be interesting to those needing high speed, high resolution circuit testing methods. This work was supported by ONR/DARPA under contract N00014-92-J-1769. Our new approach combines the high spatial resolution inherent in scanning force microscopy (SFM) with our experience in high speed electrical pulse generation to yield a new ultrafast technique, that is theoretically sensitive enough to map an electric potential profile with better than 1 picosecond time resolution and submicron lateral resolution. It is a non-invasive technique which does not require vacuum. Our efforts are aimed at the challenging task of characterizing high-speed nanometer-scale devices. Presently, no one measurement technique simultaneously addresses the requirements of ultrahigh speed and ultrasmall scale. On-wafer microwave probes and optical sampling systems have limited lateral resolution. Although electron beams can yield high resolution, such systems operate in vacuum and are significantly slower.

A scanning force microscope operates by sensing the minute deflections of a cantilever to which is attached an atomically sharp tip. In the non-contact SFM mode of operation, longer range forces (such as an attractive electric force) cause the cantilever to bend.

Suppose that a voltage  $V$  is present between a conductive SFM tip and the sample device. There will then be an attractive force  $F$  experienced by the tip. If we simply model the tip and the device as two plates of a parallel plate capacitor, we obtain:

$$F = -\frac{\epsilon_0 AV^2}{2z^2}$$

where  $\epsilon_0$  is the permittivity of vacuum, A is the effective area, and z is the effective distance. The key point is that the force is dependent on the square of the voltage. We take advantage of this nonlinearity to extend the measurement bandwidth far beyond the mechanical resonance of the cantilever, unlike past capacitance and potentiometry measurements using an SFM, which were limited by the slow cantilever response and feedback electronics. We avoid this problem by using the square-law force interaction present between the SFM and sample for mixing and sampling. The high-speed signal under test is downconverted to a much lower intermediate frequency. The tip acts as an extremely high-speed mixer/sampler. That is, if two voltages, a signal voltage and an applied sampling voltage, appear between the tip and the sample, there will be a force term corresponding to the product of the two voltages.

We have conducted preliminary mixing experiments using a commercial scanning probe microscope (Park Scientific Instruments' Autoprobe) and an available supply of silicon nitride cantilevers which were coated with gold. Our initial results confirm the principles of high-speed operation. We have demonstrated sampling with a time resolution of about 100 ps and mixing for input frequencies up to 20 GHz, above which we were constrained by package and input cable losses. We believe that future high-speed performance will not be restricted by the inherent speed of the nonlinearity or by the extremely small tip-to-sample capacitance but by stray capacitances in the system, which will be critical for measurement frequencies exceeding several hundred gigahertz. In the future, we intend to improve time and lateral resolution by integrating high-speed circuitry with a microfabricated cantilever and tip.

### **Publications and Oral Disclosures**

A. A. Godil, A. S. Hou, B. A. Auld, and D. M. Bloom, "Harmonic mode locking of a Nd:BEL laser using a 20GHz dielectric resonator / optical modulator," Opt. Lett., vol. 16, pp. 1765-1767, 1991.

A. A. Godil, A. S. Hou, B. A. Auld, and D. M. Bloom, "Harmonic mode locking of a Nd:BEL laser using a 20GHz dielectric resonator / optical modulator," IEEE Lasers and Electro-Optics Society Annual Meeting, San Jose, CA, 1991.

A. A. Godil, B. A. Auld, and D. M. Bloom, "Time-Lens Producing 1.9 psec Optical Pulses", accepted by Appl. Phys. Lett.

A. A. Godil, B.A. Auld, and D. M. Bloom, "Time-Lens Producing Picosecond Optical Pulses," presented at IEEE Lasers and Electro-Optics Society 1992 Annual Meeting, Boston, MA, November 16-19, 1992, Invited Paper.

A. A. Godil, E. A. Auld, and D. M. Bloom, "Time-Lensing", submitted to Journal Quant. Elec., Jan. 1993.

M. T. Kauffman, A. A. Godil, W. C. Banyai, and D. M. Bloom, "Applications of time-lens optical systems," 1993 Topical Meeting on Ultrafast Electronics and Optoelectronics, San Francisco, CA, January 25-27, 1993.

### **Patents and Invention Disclosures**

Although this information is detailed in form DD 882, we note here that invention disclosures or patents have been filed on three items produced under this contract. The patented item has already been licensed to industry.

Invention disclosures were filed for the following:

Dielectric Resonator Optical Modulator.

Time-lens.

A patent has been applied for:

Resonant Microwave Optical Modulator. This device has been licensed to New Focus, Inc.

# Figure 1. Temporal Focusing of Pulses

- Increased microwave power to 13 W at 10 % duty cycle
- Compressed pulsewidth = 1.9 psec

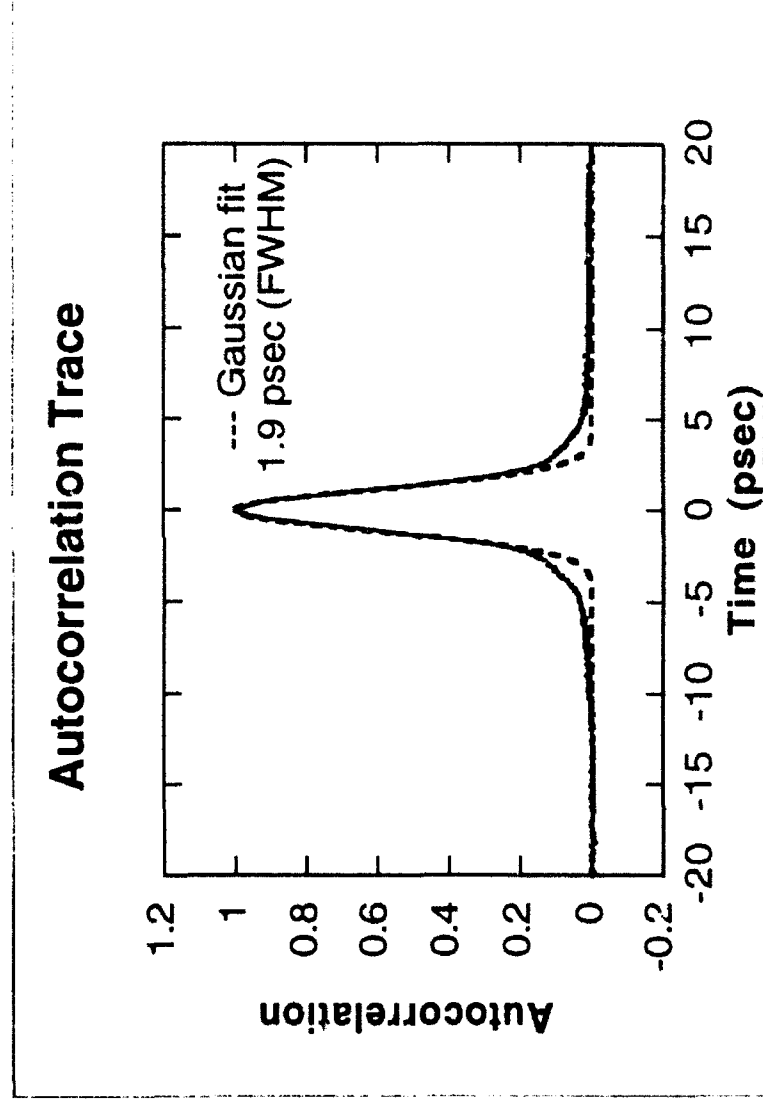


## Figure 2. Generating Pulses from CW Light.

- Phase modulator followed by 4-pass grating dispersion.
- 1 W microwave power, Measurement is detector limited.

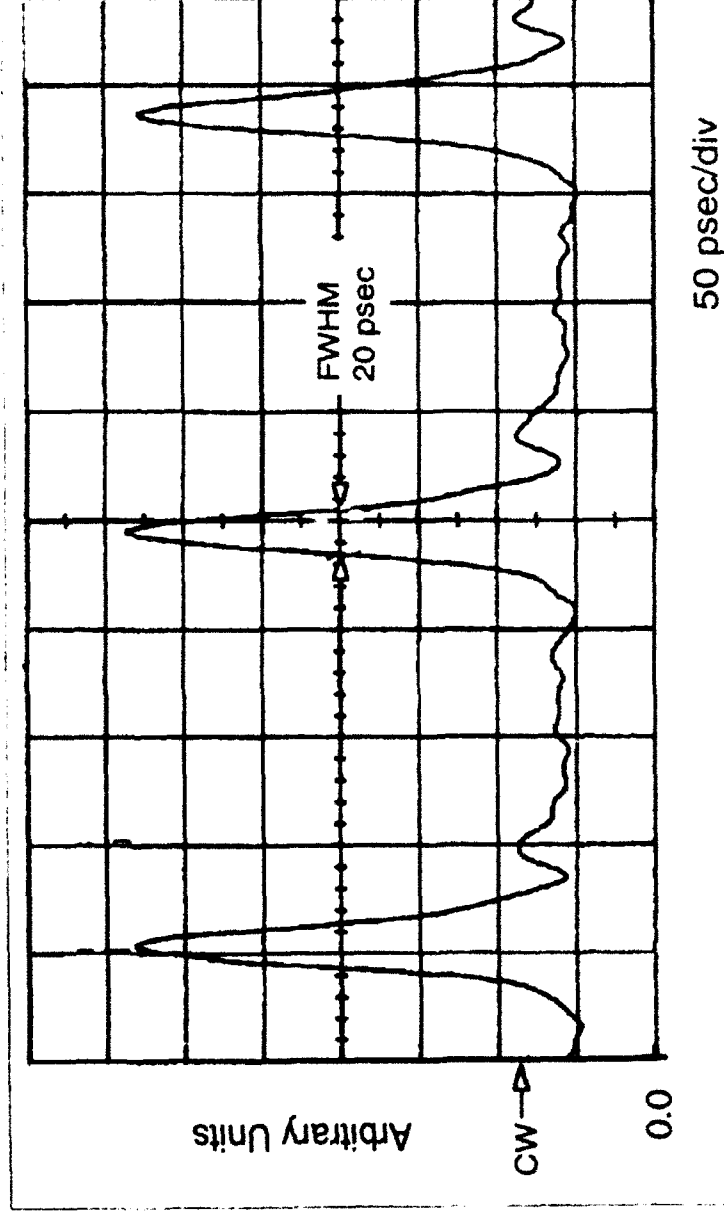
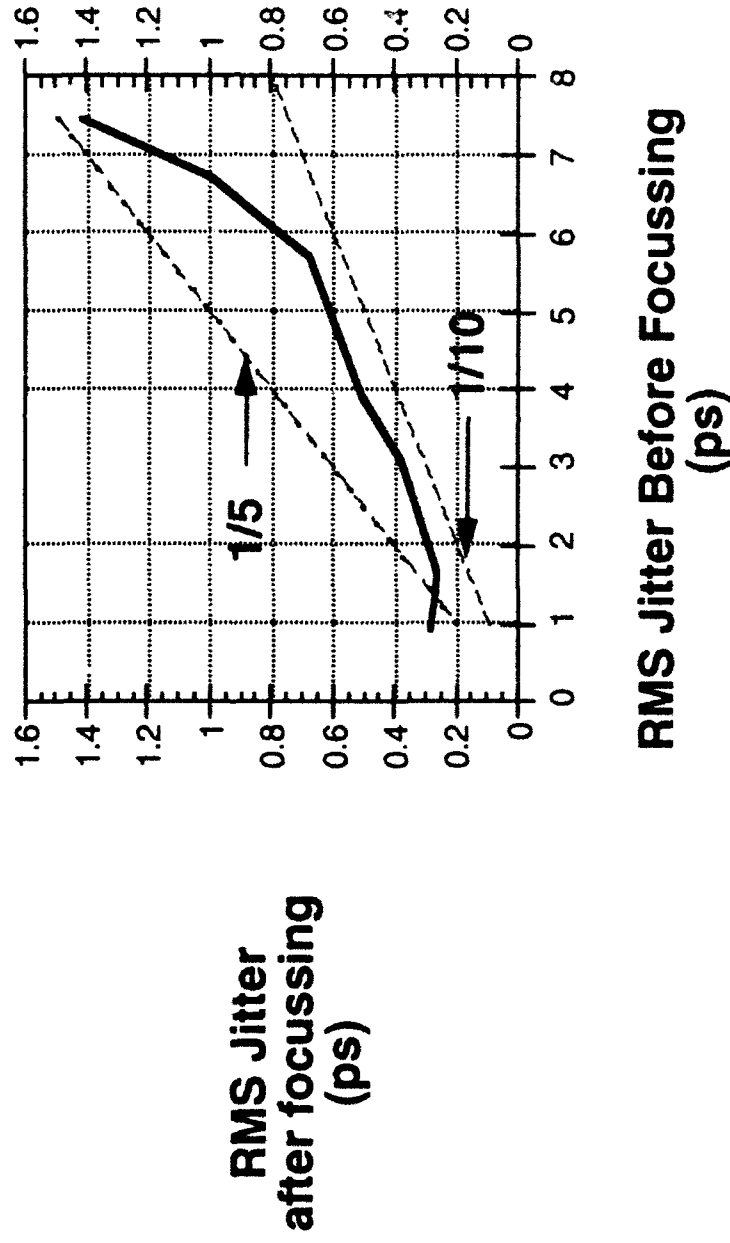


# Figure 3. Measured Jitter Suppression

- Better than 5x reduction
- Abberations prevent total cancellation



## APPENDIX

**HARMONIC MODE-LOCKING OF DIODE-PUMPED LASERS  
AND  
TIME-LENSES WITH PICOSECOND RESOLUTION**

**A DISSERTATION  
SUBMITTED TO THE DEPARTMENT OF ELECTRICAL ENGINEERING  
AND THE COMMITTEE ON GRADUATE STUDIES  
OF STANFORD UNIVERSITY  
IN PARTIAL FULFILLMENT OF THE REQUIREMENTS  
FOR THE DEGREE OF  
DOCTOR OF PHILOSOPHY**


**By  
Asif A. Godil  
December 1992**



© Copyright by Asif A. Godil, 1992

All rights reserved

I certify that I have read this dissertation and that in my opinion it is fully adequate, in scope and quality, as a dissertation for the degree of Doctor of Philosophy.



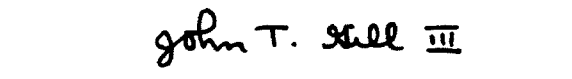
David M. Bloom  
(Electrical Engineering)  
(Principal Advisor)

I certify that I have read this dissertation and that in my opinion it is fully adequate, in scope and quality, as a dissertation for the degree of Doctor of Philosophy.



Bertram A. Auld  
(Applied Physics)

I certify that I have read this dissertation and that in my opinion it is fully adequate, in scope and quality, as a dissertation for the degree of Doctor of Philosophy.



John T. Gill  
(Electrical Engineering)

Approved for the University Committee on Graduate Studies:



*I dedicate this dissertation to my brother Afzal Godil*

## Abstract

In recent years there has been great interest in short pulsed lasers for applications in communication, fast temporally resolved measurements (electro-optic sampling), and as a means for obtaining higher peak powers. In contrast to argon ion pumped mode-locked Ti:sapphire lasers, there is a need for compact, economical, low-noise, diode-pumped, infrared wavelength short-pulsed sources. This need is addressed in the first part of the thesis, where a 20 GHz dielectric resonator/ optical modulator (DROM) is introduced and developed for harmonic mode-locking of a diode-pumped Nd:BEL laser. Depending on the mode-locker drive frequency, two distinct regimes of mode-locking were observed: (1) 2.9 psec pulses at the cavity repetition-rate of 238 MHz, (2) 3.9 psec pulses at the repetition-rate of 20 GHz. These are the shortest pulses yet reported for active mode-locking of a Nd laser. After the short pulses are created, it is desirable to have a means for controlling them. This leads to the concept of temporal imaging and time-lenses. There is an interesting analogy between the spatial problem of Fresnel diffraction and the temporal problem of first order dispersion. This can be extended to introduce the idea of a time-lens as a dual of a spatial lens (regular lens). The time-lens is simply a quadratic optical phase modulator in time, which is approximated by a portion of a sinusoidal phase modulator. Thus, by using phase modulators as lenses and grating pairs as dispersive elements, complete temporal imaging systems can be constructed in exact duality with spatial imaging systems. A resonant microwave optical phase modulator in LiNbO<sub>3</sub> with multiple passes based on an off-axis path in a stable optical resonator, is demonstrated as a time-lens. At 5.2 GHz operation, 44 radians of phase modulation was obtained at 1.06  $\mu\text{m}$  wavelength for 13 W of microwave power. This corresponds to a time-lens with 31 psec aperture and 1.9 psec resolution. This was confirmed by demonstrating temporal focusing of 45 psec pulses to 1.9 psec.

## Acknowledgements

- Prof. Dave Bloom for his support and guidance.
- Prof. Bert Auld for being my associate advisor and all his help in the thesis writing process.
- Prof. John Gill for serving as my orals committee chairman and third reader.
- Prof. Marty Fejer for being on my orals and always available for answering questions and bouncing ideas.
- Profs. Gordon Kino and Pierre Khuri-Yakub for their initial guidance at Ginzton Lab.
- Profs. John Shaw and Yoon Kim for their interaction and help.
- Sam Hou for his collaboration on the mode-locking of Nd:BEL laser.
- Kurt Weingarten and Marty Gifford of Lightwave Electronics for their collaboration and often loaning me their diode-pumped YAG laser (NPRO).
- New Focus Inc. for their loans of high speed photodiodes.
- Joe Vrehl and Chris Remen of the Crystal shop for their excellent crystal work.
- Kathy Li, Raj Apte, Mike Kauffman, Olav Solgaard, Alistair Black, John Thackara, Mohammad Shakouri, Dan Van Der Weide and Francis Ho for many helpful discussions and general help.
- Dave Patterson and Ken Toyama for their help.
- AFOSR (F49620-92-J-0099) for their financial support.

# Table of Contents

<b>Abstract</b>	<b>v</b>
<b>Acknowledgements</b>	<b>vi</b>
<b>Table of Contents</b>	<b>vii</b>
<b>List of Figures</b>	<b>x</b>
<b>List of Table</b>	<b>xiv</b>
<b>Chapter 1 Introduction</b>	<b>1</b>
<b>Chapter 2 Dielectric Resonator/ Optical Modulator (DROM)</b>	<b>3</b>
2.1 Background and Motivation .....	3
2.2 Electro-optic properties of LiNbO <sub>3</sub> .....	4
2.3 Theory and Design.....	6
2.3.1 Phase Modulation Analysis .....	8
2.3.2 QR Due to Ohmic Losses.....	10
2.3.3 Modulation Frequency Response.....	11
2.4 Construction and Measurement of DROM.....	13
2.5 Material Q of LiNbO <sub>3</sub> .....	16
References .....	20
<b>Chapter 3 Harmonic Mode-locking of Nd:BEL Laser</b>	<b>22</b>
3.1 Background: Mode-locking of Lasers .....	22
3.1.1 Kuizenga-Siegman Theory.....	23

3.1.2 Mode-Locked Diode-Pumped Nd Lasers.....	25
3.2 Diode-Pumped Nd:BEL Laser.....	26
3.3 Harmonic Mode-Locking of Nd:BEL .....	28
References .....	32
<b>Chapter 4 Space-Time Duality &amp; Temporal Imaging</b>	<b>36</b>
4.1 Fresnel Diffraction & Temporal Dispersion.....	36
4.2 Temporal Imaging.....	41
4.3 The Sinusoidal Modulator as a Time-lens.....	45
References .....	48
<b>Chapter 5 Time-Lens</b>	<b>49</b>
5.1 Resonant Microwave Optical Modulator .....	49
5.1.1 Dielectric Loaded Waveguide .....	50
5.1.2 Resonator and Resonance Condition.....	55
5.1.3 Ohmic Loss Q.....	57
5.1.4 Analysis of Optical Modulation.....	59
5.2 Multipass Modulator using Off-axis Optical Resonator .....	62
5.2.1 Multipass Synchronization .....	66
5.2.2 Modulator as Thermal Lens.....	68
5.3 Design & Construction of Time-Lens .....	70
5.3.1 Modulator Characterization.....	71
5.3.2 Microwave Resonator Frequency Tuner.....	77
5.4 Measurement of Multipass Modulator .....	78
References .....	81
<b>Chapter 6 Experiments with Time-Lens</b>	<b>84</b>
6.1 Pulses from CW Light.....	84

6.2 Temporal Focusing .....	86
References .....	93
<b>Chapter 7    Summary &amp; Future Directions</b>	<b>94</b>



## List of Figures

Figure 2.1	Comparison of metal waveguide with high- $\epsilon$ dielectric waveguide. E-field(solid line), H-field (dashed line).	6
Figure 2.2	DROM made of a LiNbO <sub>3</sub> crystal sandwiched between two brass plates and excited via a microwave connector. The E-field lines correspond to the TM <sub>101</sub> resonant mode. Origin of the coordinate system is at the center of the crystal.	8
Figure 2.3	Circuit model of DROM.	12
Figure 2.4	Measured S <sub>11</sub> of the DROM, showing the TM <sub>101</sub> resonance at about 20 GHz.	14
Figure 2.5	Measured and theoretical phase modulation of DROM for an input power of 25 dBm.	15
Figure 2.6	Circuit model showing a transmission line coupled to a resonance.	16
Figure 2.7	S <sub>21</sub> plot showing various relevant parameters for measuring Q <sub>m</sub>	18
Figure 2.8	Material Q of LiNbO <sub>3</sub> measured at various frequencies.	19
Figure 3.1	A laser resonator formed by placing two mirrors (M) around a gain medium. The modulator (amplitude or phase) inside the cavity is used for mode-locking.	24
Figure 3.2	Folded cavity, diode-pumped Nd:BEL laser, with DROM used for harmonic mode-locking. HR, highly reflecting	27
Figure 3.3	237.7 MHz pulse train as observed using a 40 GHz photodetector and a 20 GHz sampling oscilloscope.	29
Figure 3.4	Autocorrelation trace of a pulse at the 237.7 MHz repetition rate	

(solid line) as fit to a 2.9 psec gaussian pulse (dashed line).	29
Figure 3.5 Measured pulse width vs. input microwave power, showing the best fit corresponds to an eighth-root dependence.	30
Figure 3.6 Autocorrelation trace of 3.9 psec pulses at the 19.97 GHz repetition rate.	31
Figure 4.1 Transverse field distribution of monochromatic light propagating through free space $z$ .	38
Figure 4.2 Temporal imaging shown as an analog of spatial imaging.	42
Figure 4.3 A dispersive grating pair showing the various parameters.	44
Figure 4.4 Time-lens approximated by portions of a sinusoidal phase modulation.	46
Figure 5.1 Cross-section of LiNbO <sub>3</sub> loaded waveguide used for the resonator (Fig. 5.2).	51
Figure 5.2 Side-view of resonator showing cutoff guide sections on each side to confine the energy and form a resonator. Light traverses the modulator along the $z$ -axis.	51
Figure 5.3 An off-axis path in a stable optical resonator. The orthogonal dimension $x$ is not shown in the figure.	63
Figure 5.4 Side-view of multipass modulator. HR = highly reflecting.	65
Figure 5.5 Analysis of heat conduction in the modulator.	68
Figure 5.6 S <sub>11</sub> of modulator as measured on a network analyzer. The first seven resonances are labeled by letters A-G. For this measurement, resonance A is not noticeably excited because of weak coupling.	72

Figure 5.7a Change in resonant frequency as a function of the ball position for resonances A, B, C and D.	74
Figure 5.7b Change in resonant frequency as a function of the ball position for resonances E, F and G.	75
Figure 5.8 Modulation as a function of the beam position $y$ for the two resonances E and F. Microwave power = 1 W.	76
Figure 5.9 Resonator with the top removed showing the tuner.	77
Figure 5.10 Measured mutipass modulation as a function of detuning in $d_2$ , for 1 W of cw power at 5.2 GHz.	79
Figure 5.11 Measured spectrum of modulated light. RF power = 1 W cw.	80
Figure 5.12 Measured spectrum of modulated light. RF power = 13 W, 10% duty cycle. The spikes in the spectrum are an anomaly of the measurement setup, using a pulsed laser source and the sampling rate of the spectrum analyzer.	80
Figure 6.1 Pulses at 5.2 GHz, with some background light, as generated from a cw optical input. RF power = 1 W.	85
Figure 6.2 Theoretical calculation of pulses created from cw light. $A = 12$ radians, $\omega_m = 2\pi \times 5.2 \times 10^9$ rad/sec, and $g = 0.77$ . Output normalized with cw intensity.	87
Figure 6.3 Autocorrelation trace of compressed pulse with fit to a 6.7 psec (FWHM) gaussian pulse. RF power = 1 W cw.	88
Figure 6.4 Autocorrelation trace of compressed pulse with fit to a 1.9 psec (FWHM) gaussian pulse. RF power = 13 W, 10% duty cycle.	88
Figure 6.5 Up-shifting and down-shifting of the optical frequency of the	

mode-locked pulses using multipass microwave modulator.  
RF power = 1 W. 91

Figure 6.6 Comparison of measured and theoretically calculated autocorrelation traces. RF power = 1 W,  $A = 12$  radians,  $g = 0.88$  and  $t_p = 45$  psec. 92

Figure 6.7 Comparison of measured and theoretically calculated autocorrelation traces. RF power = 13 W,  $A = 43$  radians,  $g = 0.91$  and  $t_p = 45$  psec. 92

Figure 7.1 Block diagram of a system using temporal focusing to produce picosecond optical pulses at adjustable repetition rates. 96

## List of Tables

Table 4.1	Space-time duality.	37
-----------	---------------------	----

## Chapter 1 Introduction

Since the advent of lasers, there has always been a strong interest in short pulsed lasers for applications in digital communication, fast temporally resolved measurements, and as a means for obtaining higher peak powers for non-linear optical experiments. Digital soliton communication systems using erbium-doped fiber amplifiers are very close to possible commercial installation. However, as soliton sources, there is a need for clean transform-limited pulses of few picosecond to few tens of picosecond width. With increasing communication demand for higher bit rates, pulse repetition rates of few tens of GHz will be required. The second main application of short pulsed lasers is fast temporally resolved measurements. Time resolved spectroscopy is a growing field and is perhaps the last frontier in experimental spectroscopy. Another example, which is very relevant to our laboratory, is the electro-optic voltage probing of very fast GaAs circuits using picosecond optical pulses.

In contrast to argon ion pumped mode-locked Ti:sapphire lasers, there is a need for compact, economical, low-noise, diode-pumped, infrared wavelength short-pulsed sources. In recent years this has led to increased interest in mode-locking of diode-pumped

Nd lasers. In Chapter 2, a 20 GHz dielectric resonator/ optical modulator (DROM) is introduced and developed using  $\text{LiNbO}_3$ . This is used for harmonic mode-locking of a diode-pumped Nd:BEL laser in Chapter 3.

In the second part of the thesis, new ideas, concepts, and techniques are developed for controlling and manipulating short pulses of light. This is the concept of space-time duality and temporal imaging as discussed in Chapter 4. There is an interesting analogy between the spatial problem of Fresnel diffraction and the temporal problem of first order dispersion. This can be extended to introduce the idea of a time-lens as a dual of a spatial lens (regular lens). The time-lens is simply a quadratic optical phase modulator in time, which is approximated by a portion of a sinusoidal phase modulator. Thus, by using phase modulators as lenses and grating pairs as dispersive elements, complete temporal imaging systems can be constructed in exact duality with spatial imaging systems. There is a host of exciting applications of these ideas, such as time reversal, signal processing, active pulse compression, and time-microscopy of fast optical events. The latter application as an instrument can perhaps replace streak cameras. Chapter 5 develops a time-lens based on a resonant microwave optical phase modulator in  $\text{LiNbO}_3$  with multiple passes based on an off-axis path in a stable optical resonator. Results on temporal focusing, or active pulse compression, are presented in Chapter 6. Finally, in Chapter 7, the thesis is summarized and future directions are discussed.

## **Chapter 2    Dielectric Resonator/ Optical Modulator (DROM)**

The concept of using a dielectric resonator, made from an electro-optic crystal as a microwave bulk-optic modulator, is introduced. This device is called a DROM (dielectric resonator/ optical modulator). A specific configuration DROM is developed, and its theory and design are presented. A 20 GHz device made out of  $\text{LiNbO}_3$  is demonstrated with 0.1 radian of phase modulation at 1.06  $\mu\text{m}$  wavelength for 25 dBm of microwave power.

### **2.1 Background and Motivation**

Metal cavities have long been used as microwave resonators, occasionally combined with dielectric materials. However, it has been known for some time that materials of high dielectric constant ( $\epsilon$ ), by themselves, can exhibit high Q microwave resonances [2.1] depending on their shape and size. Such resonators are known as dielectric resonators. Its only recently that materials (usually ceramics) having dielectric constants between 30 and 40 with good temperature stability and low dielectric losses have become available. This has led to numerous applications of dielectric resonators in microwave oscillators and filters. In terms of size, cost, and higher Q there are significant



advantages compared to conventional cavity resonators. The shape of dielectric resonators is usually a short, solid cylinder, with the usual resonant mode being  $TE_{10\delta}$  [2.2, 2.3]. It should be pointed out that dielectric resonators have some radiative losses, and are therefore always enclosed in metal boxes.

Electro-optic crystals like  $LiNbO_3$  (dielectric constants :  $\epsilon_x = \epsilon_y = 44$ ,  $\epsilon_z = 28$ ) and  $LiTaO_3$  ( $\epsilon_x = \epsilon_y = \epsilon_z = 43$ ) have high dielectric constants. In addition, since for  $LiNbO_3$  the loss-tangent at microwave frequencies is fairly low, this material is suitable for dielectric resonators. At the microwave resonance, the electric field inside the crystal is greatly enhanced, and if the field distribution of the resonant mode is appropriate, can be used as an electro-optic modulator. This approach offers an elegant means for realizing microwave frequency optical modulation. The application and motivation for such a modulator will be discussed in the next chapter, where it is used as a mode-locker for a diode-pumped Nd:BEL laser.

## 2.2 Electro-optic properties of $LiNbO_3$

The electro-optic effect is most conveniently described using the impermeability tensor  $b_{ij}$ , which is the inverse of the dielectric tensor  $\epsilon_{ij}$ . Applying an electric field ( $E_k$ ) perturbs [2.4] the impermeability tensor by  $\Delta b_{ij}$  as

$$b_{ij} = b_{ij}^{(0)} + \Delta b_{ij} \quad (2.1)$$

$$\Delta b_{ij} = r_{ijk} E_k \quad (2.2)$$

This relation can be written in contracted tensor notation as

$$\Delta \begin{bmatrix} b_1 \\ b_2 \\ b_3 \\ b_4 \\ b_5 \\ b_6 \end{bmatrix} = \begin{bmatrix} r_{11} & r_{12} & r_{13} \\ r_{21} & r_{22} & r_{23} \\ r_{31} & r_{32} & r_{33} \\ r_{41} & r_{42} & r_{43} \\ r_{51} & r_{52} & r_{53} \\ r_{61} & r_{62} & r_{63} \end{bmatrix} \begin{bmatrix} E_x \\ E_y \\ E_z \end{bmatrix} \quad (2.3)$$

The electro-optic matrix  $\bar{r}$  for LiNbO<sub>3</sub> is [2.5]

$$\begin{bmatrix} 0 & -r_{22} & r_{13} \\ 0 & r_{22} & r_{13} \\ 0 & 0 & r_{33} \\ 0 & r_{51} & 0 \\ r_{51} & 0 & 0 \\ -r_{22} & 0 & 0 \end{bmatrix} \quad (2.4)$$

Now, writing the complete  $b_{ij}$  matrix and noting that  $b_0 = 1/n_0^2$  and  $b_e = 1/n_e^2$ , where  $n_0$  and  $n_e$  are the ordinary and extraordinary refractive indices of LiNbO<sub>3</sub> respectively, yields

$$b_{ij} = \begin{bmatrix} b_0 - r_{22}E_y + r_{13}E_z & -r_{22}E_x & r_{51}E_x \\ -r_{22}E_x & b_0 + r_{22}E_y + r_{13}E_z & r_{51}E_y \\ r_{51}E_x & r_{51}E_y & b_e + r_{33}E_z \end{bmatrix} \quad (2.5)$$

For propagation along x or y-axis, with polarization along z (c-axis) and electric field ( $E_z$ ) applied along the same direction, the change in refractive index is

$$\Delta n_e = \frac{1}{2} n_e^3 r_{33} E_z \quad (2.6)$$

This is the best crystal orientation for phase modulator applications because  $r_{33}$  is the largest electro-optic coefficient for  $\text{LiNbO}_3$  [2.5].

## 2.3 Theory and Design

In addition to choosing a resonant mode with electric field distribution appropriate for electro-optic modulation, the other requirements on a DROM include : (1)  $Q$  limited by the loss-tangent of  $\text{LiNbO}_3$  and not by ohmic or radiative losses, and (2) convenient access for optical beams. The DROM configuration satisfying these requirements, can be introduced by comparing a high- $\epsilon$  dielectric waveguide with a conventional metal waveguide (Fig. 2.1). It can be shown [2.6] that the interface between a high- $\epsilon$  dielectric and air can be approximated by an open-circuit boundary, which is the dual of a short circuit, i.e.  $H_{\text{tan}} = 0$ , and  $E_{\text{norm}} = 0$ . Since the wave equation is identical for magnetic (H) and electric (E) fields, it is clear that within the open-circuit boundary approximation, dielectric waveguide modes are the same as the metal waveguide modes (Fig. 2.1) when E and H are exchanged. In Fig. 2.1, the E and H fields are shown for the  $\text{TE}_{10}$  mode in

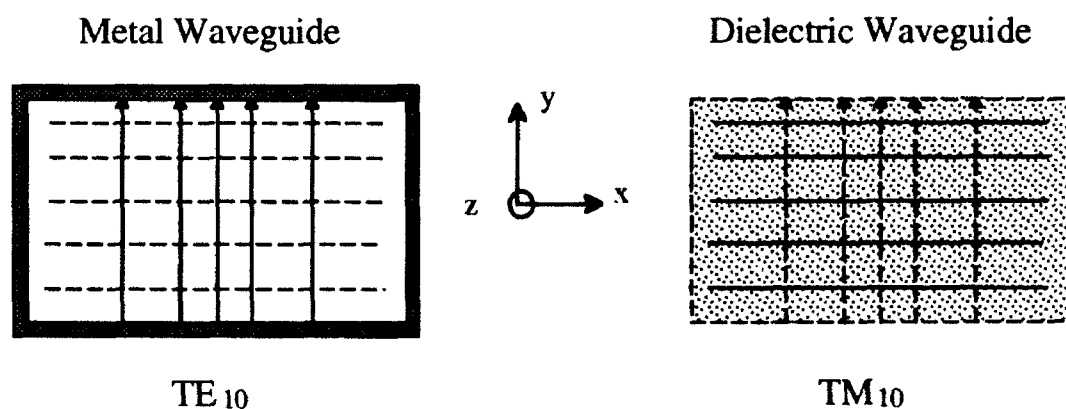


Figure 2.1 Comparison of metal waveguide with high- $\epsilon$  dielectric waveguide. E-field (solid line), H-field (dashed line)

the metal waveguide [2.7] and the corresponding  $TM_{10}$  mode for the dielectric waveguide. In the present analysis,  $LiNbO_3$  is approximated as an isotropic dielectric with a geometric mean  $\epsilon_r$  of 35.

A resonator is formed from the above described dielectric ( $LiNbO_3$ ) waveguide by placing two short-circuit planes half a guide wavelength apart in the  $z$ -direction. This is shown in Fig. 2.2, where gold plated brass plates are used not only as short-circuit planes but also for mechanically holding the crystal. Also shown is the electric field distribution of the  $TM_{101}$  resonant mode. Within the given approximations, the resonant frequency and the field distribution can be expressed as [2.8]

$$f_R = \frac{c_0}{2\sqrt{\epsilon_r}} \sqrt{\frac{1}{a^2} + \frac{1}{c^2}} \quad (2.7)$$

$$E_x = E_0 \cos(\pi x/a) \cos(\pi z/c) \quad (2.8)$$

$$E_y = 0 \quad (2.9)$$

$$E_z = E_0 c/a \sin(\pi x/a) \sin(\pi z/c) \quad (2.10)$$

$$H_x = H_z = 0 \quad (2.11)$$

$$H_y = j2 f_R \epsilon_r \epsilon_0 c E_0 \cos(\pi x/a) \sin(\pi z/c) \quad (2.12)$$

where  $f_R$  is the resonant frequency,  $c_0$  is the speed of light in vacuum,  $\epsilon_r$  is the geometric mean dielectric constant of  $LiNbO_3$  (about 35),  $\epsilon_0$  is the permittivity of free space,  $E_x$  and  $E_z$  are the  $x$  and  $z$  components of electric field inside the crystal,  $H_y$  is the  $y$  component of magnetic field inside the crystal,  $a$ ,  $b$  and  $c$  are the dimensions of the crystal in the  $x$ ,  $y$  and  $z$  directions respectively, and  $E_0$  is a constant. The  $c$ -axis of the crystal is parallel to the  $x$ -axis. Therefore,  $E_x$  leads to phase modulation of the optical beam through the  $r_{33}$  electro-optic coefficient (Eq. 2.6). The fringing field of the SMA connector pin (Fig. 2.2)

overlaps with the evanescent external field of the resonant mode and for the correct spacing gives critical coupling. Thus efficient optical phase modulation is obtained at the resonant frequency,  $f_R$ . The external field is due to the fact that the actual boundary conditions of the physical resonator are not open-circuit as assumed in Fig. 2.1. Note that if the c-axis of the crystal is chosen parallel to the z-axis (Fig. 2.2), the odd parity of  $E_z$  will cause intensity modulation at  $2f_R$  in a single-mode optical system.

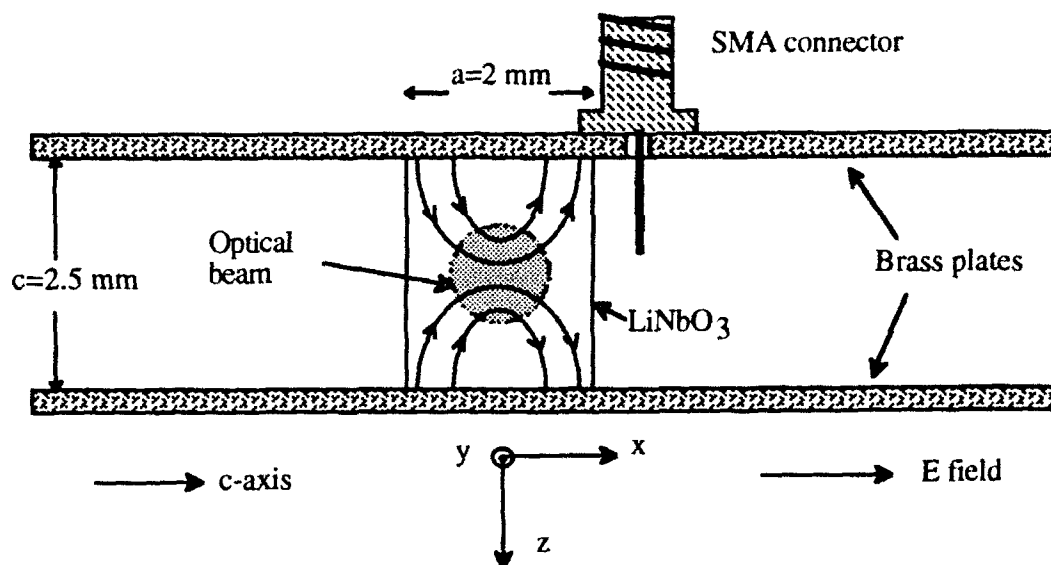


Figure 2.2 DROM made of a  $\text{LiNbO}_3$  crystal sandwiched between two brass plates and excited via a microwave connector. The E-field lines correspond to the  $\text{TM}_{101}$  resonant mode. Origin of the coordinate system is at the center of the crystal.

### 2.3.1 Phase Modulation Analysis

A convenient means for performing resonator calculations is to use the energy

definition of  $Q_0$  (unloaded  $Q$ ).

$$Q_0 = \frac{\omega_R W_0}{P} \quad (2.13)$$

where  $\omega_R$  is the angular resonant frequency,  $W_0$  is the energy stored in the resonator, and  $P$  is the input microwave power. The peak electric field in time can be obtained from the stored energy at the moment when it is entirely electric in form. Assuming that most of the energy is stored inside the crystal and using Eqs. 2.8 - 2.10 gives

$$W_0 = \frac{\epsilon_r \epsilon_0}{2} \iiint_{\text{xtal}} |E|^2 dx dy dz \quad (2.14)$$

$$W_0 = \frac{\epsilon_r \epsilon_0 E_0^2}{8} a b c (1 + c^2/a^2) \quad (2.15)$$

Combining the above with Eq. 2.13, then gives

$$E_0 = \sqrt{\frac{8a^2}{\epsilon_r \epsilon_0 a b c (a^2 + c^2)}} \sqrt{\frac{P Q_0}{\omega_R}} \quad (2.16)$$

In the actual fabricated modulator, as discussed in the next section, a highly reflecting optical coating was applied on one side of the crystal. Consequently, it is the round trip phase modulation,  $\Delta\Phi$ , which must be calculated here from Eq. 2.6. The result is

$$\Delta\Phi = \alpha \beta 2\pi \frac{2b}{\lambda_0} \frac{1}{2} n_e^3 r_{33} E_0 \quad (2.17)$$

where  $\lambda_0$  is the free space optical wavelength, and  $\alpha$  and  $\beta$  are spatial and temporal overlap factors respectively. These factors are less than one because the optical-microwave

interaction is not uniform in space or time. Substituting Eq. 2.16 into 2.17, gives the following complete expression for phase modulation,

$$\Delta\Phi = \alpha\beta \left(2\pi \frac{n_e^3 r_{33}}{\lambda_0}\right) \sqrt{\frac{8a^2b}{\epsilon_r \epsilon_0 a c (a^2 + c^2)}} \sqrt{\frac{PQ_0}{\omega_R}} \quad (2.18)$$

The factors  $\alpha$  and  $\beta$  are given by the following overlap integrals :

$$\alpha = \frac{2}{\pi w_0^2} \int_{-\infty}^{+\infty} \exp(-2x^2/w_0^2) \cos(\pi x/a) dx \int_{-\infty}^{+\infty} \exp(-2z^2/w_0^2) \cos(\pi z/c) dz$$

$$\alpha = \exp[-\pi^2 \frac{w_0^2}{8} (1/a^2 + 1/c^2)] \quad (2.19)$$

$$\beta = \frac{1}{t_r} \int_{-t_r/2}^{+t_r/2} \cos \omega_R t dt = \frac{2}{\omega_R t_r} \sin(\omega_R t_r / 2) \quad (2.20)$$

where  $w_0$  is the waist size of the input Gaussian beam and  $t_r$  is the round-trip transit time through the crystal ( $t_r = 2bn_e/c_0$ ).

### 2.3.2 $Q_R$ Due to Ohmic Losses

The  $Q$  due to ohmic losses in the metal plates,  $Q_R$ , can be evaluated by calculating the resistive power dissipated ( $P_R$ ) in the metal plates. From the definition of  $Q$ , as given in Eq. 2.13, it follows that

$$Q_R = \frac{\omega_R W_0}{P_R} \quad (2.21)$$

The surface current density on the metal plates is equal to the tangential magnetic field at the surface. This leads to [2.8],

$$P_R = \frac{R_s}{2} \left[ 2 \int_{-b/2}^{b/2} \int_{-a/2}^{a/2} |H_y|_{z=c/2}^2 dx dy \right] \quad (2.22)$$

Where  $R_s$  is the surface resistivity of the gold plating. The following is obtained when Eq. 2.12 is substituted in the above equation:

$$P_R = \frac{\epsilon_r^2 \epsilon_0^2 R_s}{2\pi^2} \omega_R^2 a b c^2 E_0^2 \quad (2.23)$$

From Eqs. 2.15, 2.21, and 2.23, the expression for  $Q_R$  is obtained,

$$Q_R = \frac{\pi^2 (1 + c^2/a^2)}{4\epsilon_r \epsilon_0 \omega_R R_s c} \quad (2.24)$$

For a good DROM design,  $Q_R$  should be much greater than  $Q_m$  (material Q of LiNbO<sub>3</sub>, section 2.5). The combined effect of these two losses corresponds to  $Q_0$ , as given by,

$$\frac{1}{Q_0} = \frac{1}{Q_m} + \frac{1}{Q_R} \quad (2.25)$$

### 2.3.3 Modulation Frequency Response

The resonator can be modeled as a parallel RLC circuit, as shown in Fig. 2.3, with



a current source of impedance  $R_s$ . The admittance of the circuit is

$$Y = 1/R_s + 1/R + j(\omega C - 1/\omega L) \quad (2.26)$$

$$Y = \frac{1}{R_s \parallel R} [1 + j(\omega^2 - \omega_R^2) Q_L / \omega^2] \quad (2.27)$$

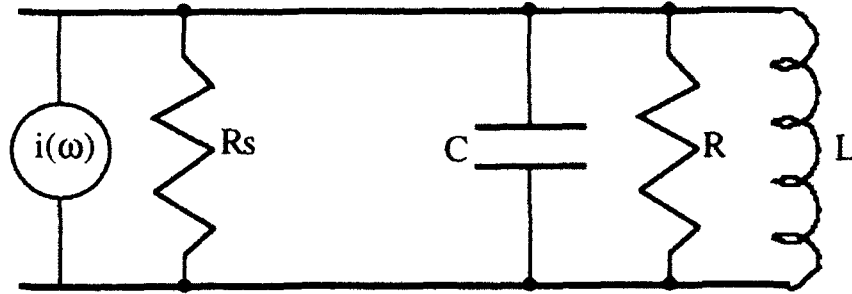


Figure 2.3 Circuit model of DROM.

where  $Q_L$  is the loaded  $Q$  ( $Q_L = \omega C R_s \parallel R$ ) and  $\omega_R = \sqrt{1/LC}$  is the resonant frequency. Phase modulation in the DROM is proportional to the voltage across the capacitor in our model. This in turn is proportional to the impedance  $Z$  ( $1/Y$ ). For a high- $Q$  circuit operating close to resonance,  $\omega - \omega_R \ll \omega_R$  and  $\omega + \omega_R \approx 2\omega_R$ . Under this approximation, the frequency dependence of phase modulation can be easily expressed as

$$\Delta\phi(\omega) = \frac{\Delta\Phi}{1 + j2Q_L(\omega - \omega_R)/\omega_R} \quad (2.28)$$

where  $\Delta\Phi$  is the modulation exactly on resonance as given by Eq. 2.18. For critical coupling of the resonator,  $R = R_s$ , and therefore  $Q_L = Q_0/2$ .

## 2.4 Construction and Measurement of DROM

A DROM was constructed [2.9] from a  $\text{LiNbO}_3$  crystal with the following dimensions :  $a = 2$ ,  $b = 1.8$ , and  $c = 2.5$  (mm). The metal plates (Fig. 2.2) are gold plated brass. From Eq. 2.7 this corresponds to  $f_R = 16.3$  GHz. The resonator is characterized using an HP8510 network analyzer (Fig. 2.4), giving a measured resonant frequency,  $f_R = 20$  GHz. The discrepancy is not unexpected because Eq. 2.7 assumes perfect open-circuit boundary conditions at the  $\text{LiNbO}_3$ -air interfaces and an isotropic dielectric constant, both of which are approximations. The unloaded  $Q$  ( $Q_0$ ) is also inferred from the Smith chart measurement using the model of Fig. 2.3. The impedance looking into the resonator (without the source) near  $\omega_R$  is approximately given as,

$$Z = \frac{R}{1 + j2Q_0(\omega - \omega_R) / \omega_R} \quad (2.29)$$

If the impedance is  $Z = R / (1 \pm j) = R(1 \mp j) / 2$  at frequencies  $\omega_1$  and  $\omega_2$  respectively, then  $Q_0 = \omega_R / (\omega_1 - \omega_2)$ . These frequencies are easily measured on the network analyzer giving a value of  $Q_0 = 500$ . From Eq. 2.24, the  $Q$  due to ohmic losses is  $Q_R = 1530$ . Thus,  $Q_0$  is largely limited by the material  $Q$  of  $\text{LiNbO}_3$  as discussed further in Section 2.5.

One facet of the crystal is anti-reflection coated, and the opposite facet is a 97% reflector for  $1.07 \mu\text{m}$  wavelength. The DROM is used as both output coupler and mode-locker for a diode-pumped Nd:BEL laser, as will be discussed in the next chapter. The round-trip optical phase modulation is measured by looking at the sidebands produced on

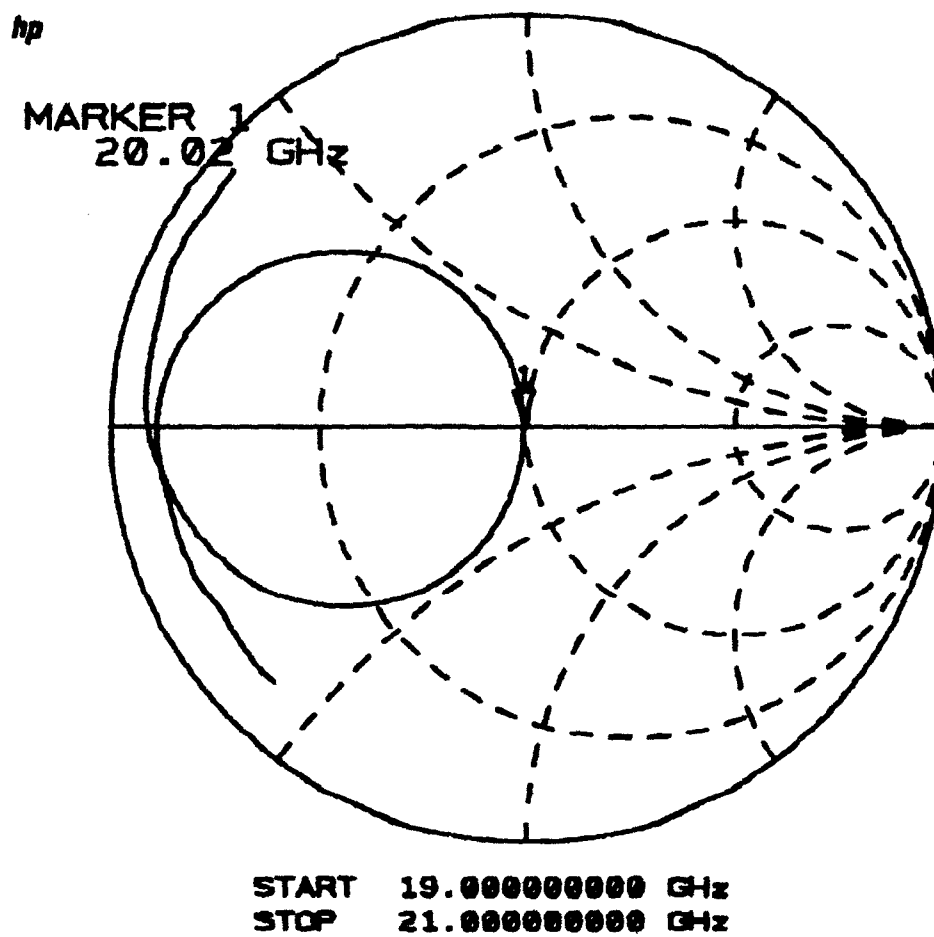


Figure 2.4 Measured  $S_{11}$  of the DROM, showing the  $TM_{101}$  resonance at about 20 GHz.

a single-frequency ( $\omega_0$ ) laser using a scanning Fabry-Perot cavity as an optical spectrum analyzer. Phase modulation  $\Delta\phi$  at frequency  $\omega$  produces sidebands on the optical carrier ( $\omega_0$ ) as follows,

$$\exp j(\omega_0 t + \Delta\phi \sin \omega t) = \sum_{q=-\infty}^{+\infty} J_q(\Delta\phi) \exp j(\omega_0 + q\omega)t \quad (2.30)$$

where  $J_q$  is the  $q$ th order Bessel function. Modulation is inferred by measuring  $J_1^2/J_0^2$  using the scanning Fabry-Perot cavity, and is plotted in Fig. 2.5 for 25 dBm of microwave input power. The theoretical prediction is also shown in the figure using Eqs. 2.18-2.20, 2.28, with  $Q_0 = 600$  providing the best fit to the measured data. For the given

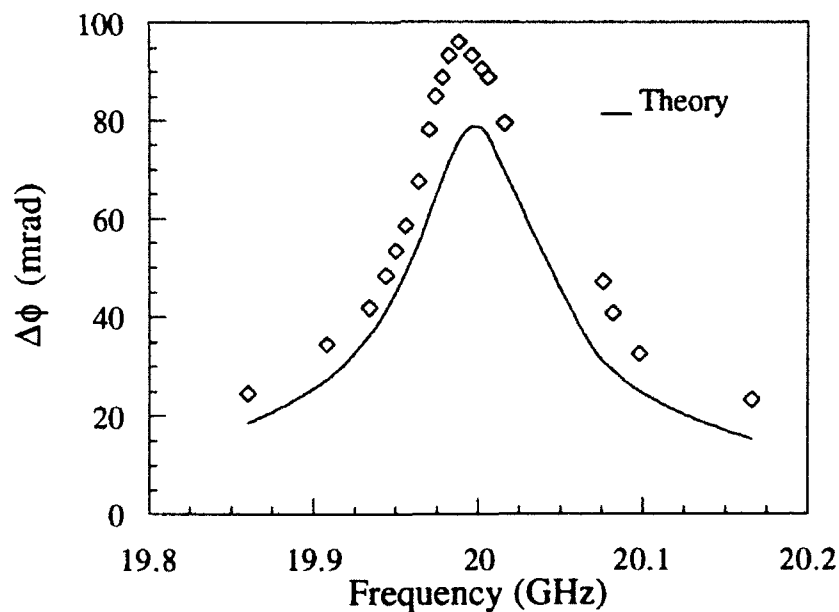


Figure 2.5 Measured and theoretical phase modulation of DROM for an input power of 25 dBm.

parameters, the spatial and temporal overlap factors are  $\alpha = 0.96$  and  $\beta = 0.61$  respectively. The peak optical phase shift is measured to be 0.1 radian with a 3 dB bandwidth of 60 MHz for 25 dBm of input power.

## 2.5 Material Q of LiNbO<sub>3</sub>

Dielectric losses in LiNbO<sub>3</sub> have been measured to some extent previously [2.10-2.12]. However, precise measurements of the material Q ( $Q_m$ ) of LiNbO<sub>3</sub> in the frequency range of interest (5 - 25 GHz) were not found in the published literature. The technique used for measuring  $Q_m$  is briefly described in reference [2.13]. The setup involves a microwave metal waveguide, with a small piece of LiNbO<sub>3</sub> of varying size, suspended inside using Styrofoam. Looking at the transmitted wave through the waveguide ( $S_{21}$ ) on a network analyzer, shows strong resonances corresponding to different dielectric resonator modes in the LiNbO<sub>3</sub> piece. It is known that for high- $\epsilon$  dielectric resonators, most of the electrical energy is confined in the dielectric. Consequently, the Q of the resonance inferred from  $S_{21}$  measurements is the same as the material Q of LiNbO<sub>3</sub>. The circuit model [2.14] for the experiment is shown below in Fig. 2.6.

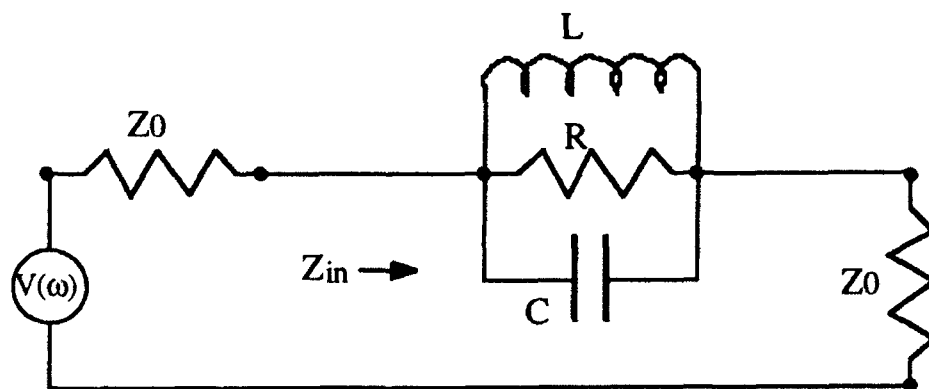


Figure 2.6 Circuit model showing a transmission line coupled to a resonance.

The waveguide is represented by a transmission line of impedance  $Z_0$ , which is coupled to the  $\text{LiNbO}_3$  dielectric resonator represented by an RLC circuit. The value of  $R$  is proportional to the coupling. Impedance  $Z_{in}$  (Fig. 2.6) is given by,

$$Z_{in} = Z_0 + Z = Z_0 + \frac{R}{1 + j2Q_0(\omega - \omega_R) / \omega_R} \quad (2.31)$$

From this,  $S_{21}$  is

$$S_{21} = \frac{2Z_0}{Z + 2Z_0} \quad (2.32)$$

$$S_{21} = \frac{1 + j2Q_0(\omega - \omega_R) / \omega_R}{1 + R/2Z_0 + j2Q_0(\omega - \omega_R) / \omega_R} \quad (2.33)$$

On resonance :

$$S_{21}(\omega_R) = \frac{1}{1 + R/2Z_0} = -L \text{ [dB]} \quad (2.34)$$

where  $-L$  is  $S_{21}(\omega_R)$  on a dB scale,

$$L = 20 \log(1 + R/2Z_0) \quad (2.35)$$

Now, at frequencies  $\omega = \omega_R \pm \Delta\omega' / 2$ , such that  $j2Q_0(\omega - \omega_R) / \omega_R = \pm j$ , then  $S_{21}$  is

$$S_{21}(\omega_R \pm \Delta\omega' / 2) = \frac{1 \pm j}{(1 + R/2Z_0) \pm j} = -L' \text{ [dB]} \quad (2.36)$$

where  $L'$  is expressed as,

$$L' = -20 \log |S_{21}| = 10 \log \left[ \frac{(1 + R/2Z_0)^2 + 1}{2} \right] \quad (2.37)$$

$$L' = 10 \log [(1 + 10^{L/10}) / 2] \quad (2.38)$$

The general features of  $S_{21}$  are shown in Fig. 2.7. First  $L$  is measured and then  $L'$  is inferred from Eq. 2.38. The  $Q$  directly follows from the measured value of  $\Delta\omega'$ ,

$$Q_0 = Q_m = \omega_R / \Delta\omega' \quad (2.39)$$

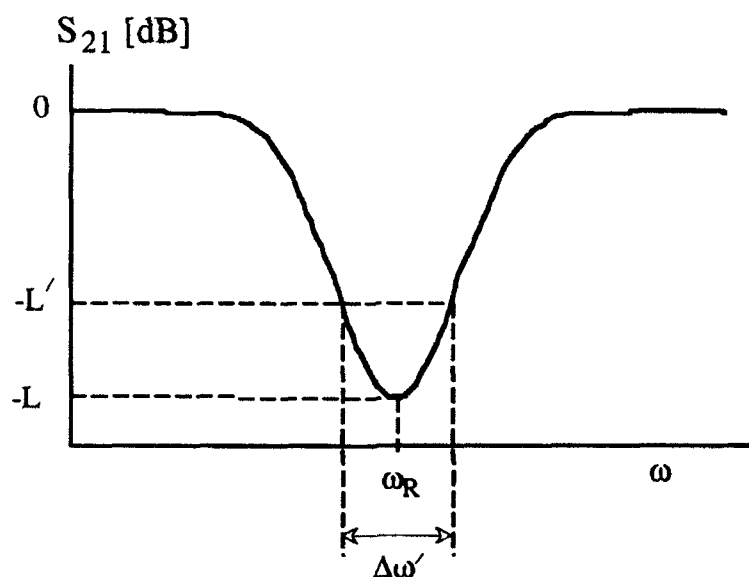


Figure 2.7  $S_{21}$  plot showing various relevant parameters for measuring  $Q_m$

The material  $Q$  is measured at various points over a large frequency range, using different waveguides and  $\text{LiNbO}_3$  pieces of varying sizes. The results are shown in Fig. 2.8. At 20 GHz  $Q_m$  is about 900, while a  $Q_0$  of about 500 was measured earlier for the DROM. This inconsistency was resolved by realizing that a different stock of  $\text{LiNbO}_3$  was used for the two experiments. Measuring  $Q_m$  for the DROM stock of  $\text{LiNbO}_3$ , indeed gave a value of about 500 at 20 GHz.

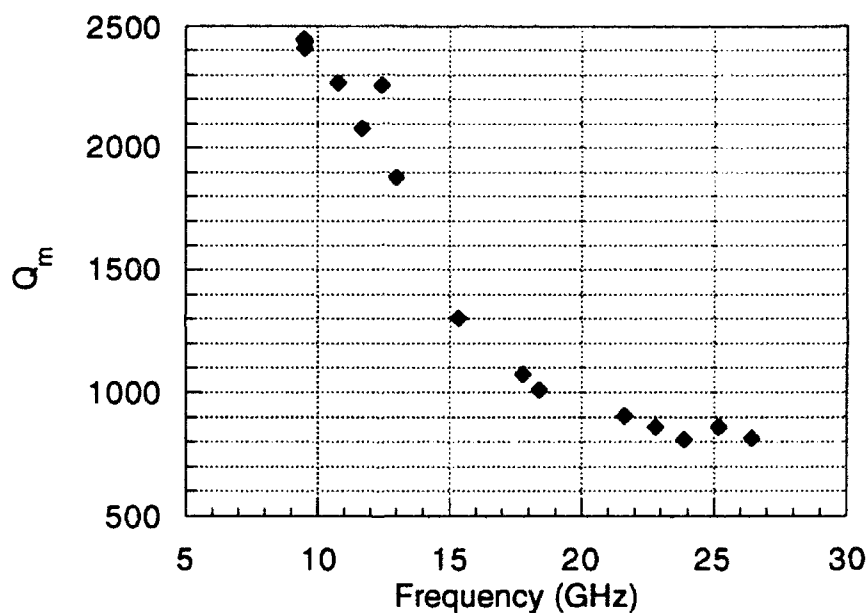


Figure 2.8 Material  $Q$  of  $\text{LiNbO}_3$  measured at various frequencies.



**References**

- 2.1 R. D. Richtmyer, "Dielectric resonator," *J. Appl. Phys.*, vol. 10, pp. 391-398, 1939.
- 2.2 J. C. Sethares and S. J. Naumann, "Design of microwave dielectric resonators," *IEEE Trans. Microwave Theory and Techniques*, vol. MTT-14, pp. 2-7, 1966.
- 2.3 S. B. Cohn, "Microwave bandpass filters containing high-Q dielectric resonators," *IEEE Trans. Microwave Theory and Techniques*, vol. MTT-16, pp. 218-227, 1968.
- 2.4 S. Harris, Class notes on non-linear optics, Stanford University.
- 2.5 A. Yariv, *Optical Electronics*, New York: Holt, Rinehart and Winston, 1985, ch. 9.
- 2.6 D. Kajfez and P. Guillon, *Dielectric Resonators*, Oxford, Mississippi: Vector Fields, 1990, p. 114.
- 2.7 S. Ramo, J. R. Whinnery, and T. Van Duzer, *Fields and Waves in Communication Electronics*, New York : John Wiley & Sons, Inc., 1984, ch. 8.
- 2.8 S. Ramo, J. R. Whinnery, and T. Van Duzer, *Fields and Waves in Communication Electronics*, New York : John Wiley & Sons, Inc., 1984, ch. 10.
- 2.9 A. A. Godil, A. S. Hou, B. A. Auld, and D. M. Bloom, "Harmonic mode locking of a Nd:BEL laser using a 20 GHz dielectric resonator/ optical modulator," *Opt. Lett.*, vol. 16, pp. 1765-1767, 1991.
- 2.10 W. M. Robertson, G. Arjavalingam, and G. V. Kopcsay, "Broadband microwave dielectric properties of Lithium Niobate," *Electron. Lett.*, vol. 27, pp. 175-176, 1991.

- 2.11 B. H. Ahn, "Measurement of the indices of refraction and the absorption coefficients of dielectric materials in the millimeter wave region," *J. Appl. Phys.*, vol. 54, pp. 2123-2124, 1983.
- 2.12 D. R. Bosomworth, "The far infrared optical properties of  $\text{LiNbO}_3$ ," *Appl. Phys. Lett.*, vol. 9, pp. 330-331, 1966.
- 2.13 M. Onoda, J. Kuwata, K. Kaneta, K. Toyama, and S. Nomura, " $\text{Ba}(\text{Zn}_{1/3}\text{Nb}_{2/3})\text{O}_3$  -  $\text{Sr}(\text{Zn}_{1/3}\text{Nb}_{2/3})\text{O}_3$  solid solution ceramics with temperature-stable high dielectric constant and low microwave loss," *Jpn. J. Appl. Phys.*, vol. 21, pp. 1707-1710, 1982.
- 2.14 A. Khanna and Y. Garault, "Determination of loaded, unloaded, and external quality factors of a dielectric resonator coupled to a microstrip line," vol. MTT-31, pp. 261-264, 1983.

## **Chapter 3   Harmonic Mode-locking of Nd:BEL Laser**

Harmonic mode-locking of a 238 MHz diode-pumped Nd:BEL laser cavity is demonstrated at the 84th harmonic, using the 20 GHz dielectric resonator/optical modulator (DROM) introduced and developed in the last chapter. An overview of mode-locking of lasers is presented, followed by a description of the experimental setup and the results obtained. Depending on the DROM drive frequency, two distinct regimes of mode-locking were observed: (1) 2.9 psec pulses at a repetition-rate of 238 MHz, (2) 3.9 psec pulses at a repetition-rate of 20 GHz. These are the shortest pulses ever reported for active mode-locking of a Nd laser [3.1, 3.2].

### **3.1 Background: Mode-locking of Lasers**

Phase locking of a large number of axial cavity modes of a laser resonator, using an active modulator or some nonlinear interaction, is known as mode-locking. In the time domain this generates short pulses of light at a repetition rate corresponding to the axial mode-spacing frequency ( $f_{ax}$ ). Mode-locking was first theoretically discussed by DiDomenico [3.3] and first demonstrated in a He-Ne laser by Hargrove et al. [3.4] in

1964. Since then the field has expanded very rapidly. Many different techniques of mode-locking have been developed and applied to various laser systems. At the same time, theoretical understanding and prediction have advanced considerably, even though the theory is far from complete because of the complex laser dynamics involved. A good review of the early history of mode-locking is given in reference [3.5]. Broadly speaking, mode-locking can be divided into two types : active and passive. In the first case, the coupling mechanism between the axial modes is a phase or intensity modulator driven at the axial mode-spacing frequency ( $f_{ax}$ ). It is possible to drive the modulator at some integer multiple of this frequency, or  $f_m = N \times f_{ax}$ , in what is referred to as harmonic mode-locking [3.6]. Here the modulator couples every Nth axial mode. However, gain saturation and spatial hole burning may provide some coupling at  $f_{ax}$ . For passive mode-locking the coupling is caused by an index or absorption change that is a nonlinear function of intensity. In the last few years, many interesting techniques for passive mode-locking of solid-state lasers have developed. In this chapter, however, the discussion will be limited to active mode-locking.

### 3.1.1 Kuizenga-Siegman Theory

Over the years, many different theories of active mode-locking have been presented [3.7, 3.8, 3.9, 3.10, 3.11]. The simple model developed by Kuizenga and Siegman for homogeneously broadened lasers [3.12, 3.13], best lends itself to intuitive understanding and straightforward calculation. This theory is briefly described here. Consider a laser resonator with an intracavity phase or amplitude modulator, as shown in Fig. 3.1. The modulator is driven sinusoidally at a frequency  $f_m$  adjusted to the axial mode-spacing  $f_{ax} = c_0/2L$ , or some harmonic (N) thereof. A complex (including chirp) gaussian pulse is tracked through the cavity over one complete round trip, passing twice

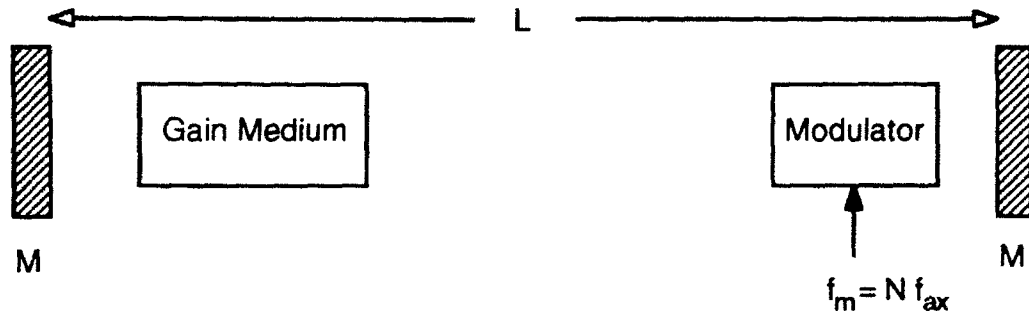


Figure 3.1 A laser resonator formed by placing two mirrors (M) around a gain medium. The modulator (amplitude or phase) inside the cavity is used for mode-locking.

through the gain medium and the modulator. For a stable steady-state solution, the pulse shape should remain unchanged from one complete round trip to another. Omitting details of the analysis, the mode-locked pulse width (intensity FWHM) for amplitude modulation can be simply stated as [3.12],

$$\tau_{p,AM} = 0.45 \left( \frac{g_0}{\Delta_m} \right)^{1/4} \sqrt{\frac{1}{f_m \Delta f_a}} \quad (3.1)$$

where  $g_0$  is the saturated round trip gain,  $\Delta_m$  is the peak amplitude modulation,  $f_m$  is the modulation frequency, and  $\Delta f_a$  is the bandwidth of the homogeneous gain medium. The pulses are transform limited with a time-bandwidth product of 0.442. For mode-locking with a phase modulator, the pulse width is slightly larger :

$$\tau_{p,FM} = 0.53 \left( \frac{g_0}{\Delta_m} \right)^{1/4} \sqrt{\frac{1}{f_m \Delta f_a}} \quad (3.2)$$

where  $\Delta_m$  is the peak phase modulation. However, for FM mode-locking, the pulses are chirped with a time-bandwidth product of  $0.442 \times \sqrt{2} = 0.626$ .

### 3.1.2 Mode-Locked Diode-Pumped Nd Lasers

In recent years, there has been a tremendous amount of interest in diode-pumped Nd:YAG lasers, partly because of their significant advantages over flashlamp-pumped YAG lasers. High power diode arrays in the 1-10 W range are now available from several manufacturers. The arrays have good electrical to optical conversion efficiency, about 30%, but the different stripes of the array emit independently with random phases in several axial modes. Therefore, diode arrays by themselves are not very useful lasers. However it makes a very convenient and efficient pump for Nd:YAG lasers with efficiencies of about 30%, giving a total wall-plug efficiency (electrical to YAG output) of about 10%. The output of such lasers is usually a TEM<sub>00</sub> spatial mode, with single-frequency operation for some designs. In addition, compared to flashlamp-pumped systems, these lasers offer compact size, stable low-noise performance, and longer lifetime.

Advances in diode pumping has also led to much interest in mode-locking of diode-pumped Nd lasers, partly because of the advantages discussed above. Pulse widths of 7-12 psec have been demonstrated with active mode-locking of diode-pumped Nd:YAG [3.14], Nd:YLF [3.15, 3.16, 3.17], and Nd:glass [3.18, 3.19] lasers. The modelocker is either an acousto-optic intensity modulator or an electro-optic phase modulator made out of LiNbO<sub>3</sub> or LiTaO<sub>3</sub>. Pulsed FM-mode-locking [3.20] and conventional acousto-optic mode-locking [3.21] of a diode-pumped Nd:BEL laser have both produced 7.5 psec

pulses. By using an acousto-optic modulator in the Raman-Nath regime, 3.8 psec pulses were recently obtained from a Nd:glass laser [3.22]. Pulse widths of 1.5 to 4 psec have been obtained using nonlinear, coupled-cavity, passive mode-locking schemes with Nd:YAG [3.23] and Nd:YLF [3.24, 3.25] lasers. Active mode-locking in the 1-5 GHz repetition rate with diode-pumping has been demonstrated by several groups using both amplitude and phase modulators [3.26, 3.27, 3.28, 3.29].

### 3.2 Diode-Pumped Nd:BEL Laser

It is known from Eqs.(3.1, 3.2) that the mode-locked pulse width is inversely proportional to the square root of the laser linewidth. Nd:YAG has a linewidth of  $6.5 \text{ cm}^{-1}$ , in comparison to  $12 \text{ cm}^{-1}$  and about  $180 \text{ cm}^{-1}$  for YLF and glass respectively. Even though Nd:glass has an extremely large bandwidth, it is plagued by a small stimulated-emission cross section and thermal problems. Nd doped Lanthanum beryllate ( $\text{La}_2\text{Be}_2\text{O}_5$  or BEL) has a stimulated-emission cross section about half that of YAG, with a linewidth of  $30 \text{ cm}^{-1}$  [3.30]. Therefore, it is a good compromise host for mode-locked Nd lasers. An additional advantage to BEL is its relatively broad absorption band. With the absorption peak centered at 810 nm, diode lasers suitable for pumping YAG can also be used for BEL, but with less stringent requirements on wavelength [3.31].

The design of the diode-pumped Nd:BEL laser is based on an astigmatically compensated folded cavity, as shown in Fig. 3.2, which has become popular for diode-pumped lasers [3.14]. The pump diode is a 1 W array [3.32] with an emitting region of  $200 \mu\text{m} \times 1 \mu\text{m}$ . It is imaged into as small a spot as possible on the BEL rod using a spherical ( $f=3.3 \text{ mm}$ ) and two cylindrical ( $f=-12.7$  and  $+12.7 \text{ mm}$ ) lenses. The length of the BEL rod was chosen to be 5 mm to absorb most of the pump, whose wavelength was

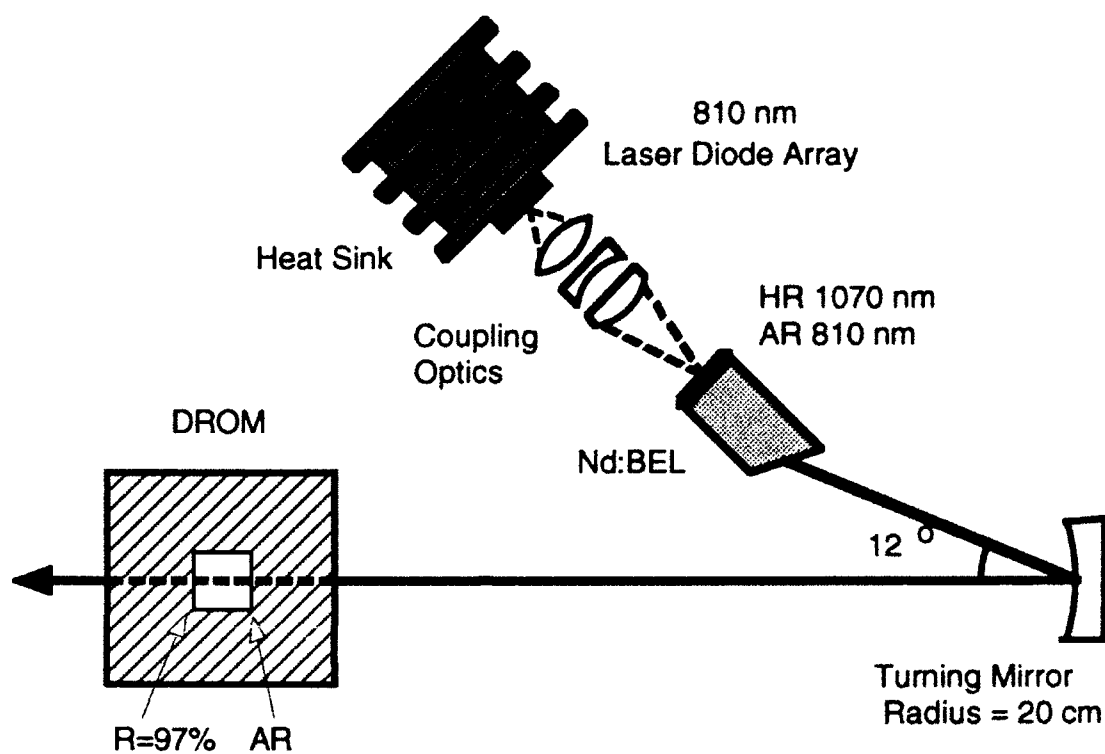


Figure 3.2 Folded cavity, diode-pumped Nd:BEL laser, with DROM used for harmonic mode-locking. HR, highly reflecting; AR, antireflecting.



selected and temperature controlled for operation near 810 nm. The other side of the BEL rod is brewster cut, with astigmatism compensated by the 12° fold in the cavity. The cavity length was chosen to give  $f_{ax} = 238$  MHz. At 1.6 A of diode current, about 800 mW of pump light is emitted of which about 660 mW reaches the BEL. First the laser was setup with a standard 3% output coupler, giving 90 mW output power at 1.07  $\mu$ m wavelength.

### 3.3 Harmonic Mode-Locking of Nd:BEL

Next, the standard output coupler of the laser cavity was conveniently replaced (Fig. 3.2) by the 20 GHz DROM developed in the last chapter. One facet of the DROM crystal is anti-reflection-coated, and the opposite facet is a 97% reflector for 1.07  $\mu$ m wavelength. Thus, it serves the dual function of output coupler and mode-locker. The two faces of the crystal are wedged about 1 deg to eliminate any detrimental etalon effects. The laser cavity axial frequency is about 237.7 MHz and the DROM is operated on resonance at the 84th harmonic of that, about 19.97 GHz. The mode-locker drive frequency could be fine-tuned to give two distinct regimes of mode-locking. For one range of drive frequencies, surprisingly, mode-locked pulses at a repetition rate of 237.7 MHz are obtained as shown in Fig. 3.3. This measurement was made with a fast photodetector [3.33] and a 20 GHz sampling oscilloscope [3.34]. The corresponding autocorrelation trace [3.35] of a typical pulse is shown in Fig. 3.4. The pulses had minimal wings, as evidenced by the excellent fit [3.36] to a 2.9 psec (FWHM) gaussian pulse. The FWHM spectral width, as measured using an optical spectrum analyzer [3.37], was 0.61 nm. This translates into a time-bandwidth product of 0.48, which is 1.1 times transform-limited. We observed an eighth-root dependence of pulse width on microwave power into the DROM (Fig. 3.5), as expected from the Kuizenga-Siegman theory (Eq. 3.2). A time-

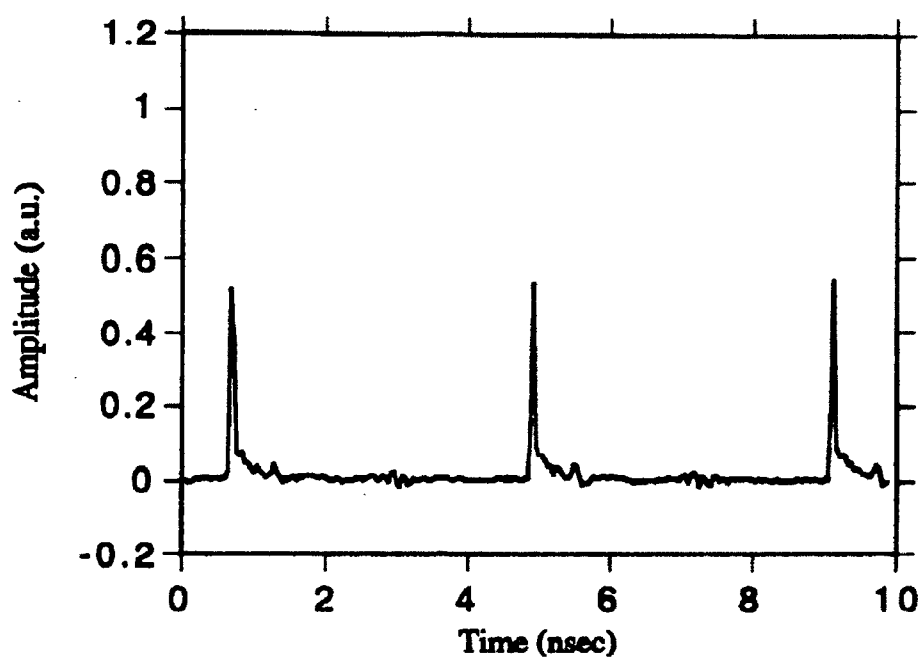


Figure 3.3 237.7 MHz pulse train as observed using a 40 GHz photodetector and a 20 GHz sampling oscilloscope.

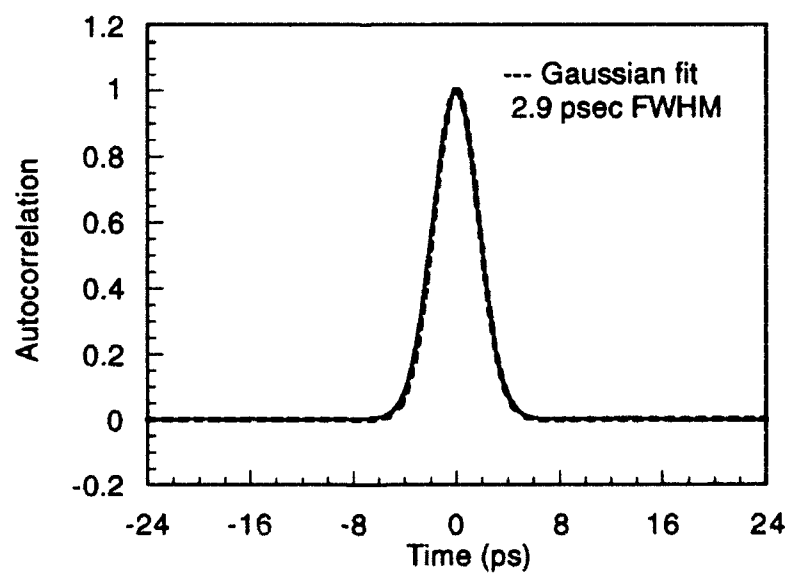


Figure 3.4 Autocorrelation trace of a pulse at the 237.7 MHz repetition rate (solid line) as fit to a 2.9 psec gaussian pulse (dashed line).

bandwidth product of 0.626 for FM mode-locking and 0.44 for AM mode-locking is expected from theory [3.12]. The possibility of AM playing a role in our experiments is unlikely, for that would have given a fourth-root dependence of pulse width on microwave power. Stable mode-locking was obtained with microwave power as low as 70 mW. Increasing the mode-locker drive frequency about 30 KHz yields another mode-locking regime, with pulses at 19.97 GHz repetition rate. The corresponding autocorrelation trace, along with a fit to 3.9 psec gaussian pulses, is shown in Fig. 3.6. The spectrum in this case is shifted -0.5 nm relative to the first mode-locked regime, with a spectral width of 0.95 nm. Mode-locking at 19.97 GHz also occurred when the mode-locker drive frequency was decreased by about 70 KHz, in which case 5.5 psec pulses with a 0.99-nm-wide spectrum, this time shifted +0.5 nm relative to the first regime, were seen. In each regime, the laser remains stably mode-locked for tens of minutes without

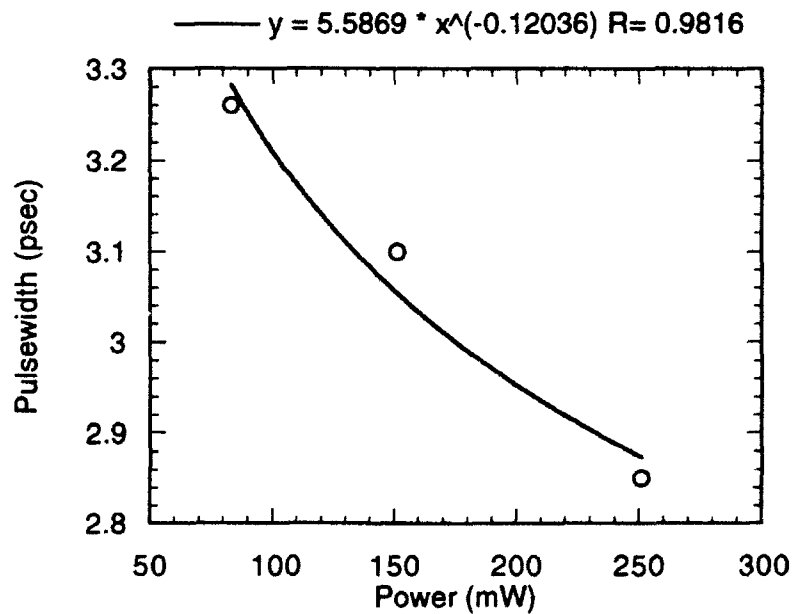


Figure 3.5 Measured pulse width vs. input microwave power, showing the best fit corresponds to an eighth-root dependence.

any feedback control. With 660 mW of diode pump power incident on the BEL rod, 50 mW average output power is obtained.

Becker et al. [3.6] demonstrated harmonic mode-locking of a Nd:YAG laser up to the 5th harmonic and always observed the pulse repetition rate to be the same as the mode-locker drive frequency, even though under certain conditions all axial modes of the laser cavity were observed in the optical spectrum. Mode-locking behavior similar to ours was reported for 2nd harmonic mode-locking [3.38]. For mode-locking at 19.97 GHz as discussed above, a  $\pm 0.5$  nm shift in the optical spectrum combined with dispersion in the gain medium, qualitatively accounts for the  $\pm 30$ –70 KHz detuning in the drive frequency for the two regimes. From Eq. 3.2, the predicted pulse width is 4 psec. However, beyond that, our understanding of FM harmonic mode-locking is incomplete.

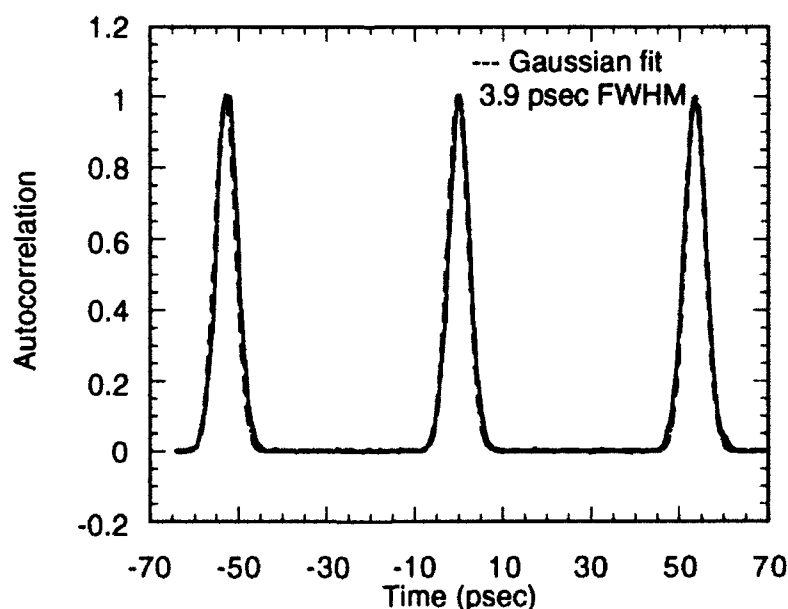


Figure 3.6 Autocorrelation trace of 3.9 psec pulses at the 19.97 GHz repetition rate.

**References**

- 3.1 A. A. Godil, A. S. Hou, B. A. Auld, and D. M. Bloom, "Harmonic mode locking of a Nd:BEL laser using a 20 GHz dielectric resonator/optical modulator," *Opt. Lett.*, vol. 16, pp. 1765-1767, 1991.
- 3.2 A. A. Godil, A. S. Hou, B. A. Auld, and D. M. Bloom, "Harmonic mode locking of a Nd:BEL laser using a 20 GHz dielectric resonator/optical modulator," IEEE Lasers and Electro-optic Society Annual Meeting, San Jose, CA, 1991.
- 3.3 M. DiDomenico, "Small-signal analysis of internal (coupling type) modulation of lasers," *J. Appl. Phys.*, vol. 35, pp. 2870-2876, 1964.
- 3.4 L. E. Hargrove, R. L. Fork, and M. A. Pollack, "Locking of He-Ne laser modes induced by synchronous intracavity modulation," *Appl. Phys. Lett.*, vol. 5, pp. 4-5, 1964.
- 3.5 P. W. Smith, "Mode-locking of lasers," *Proc. IEEE*, vol. 58, pp. 1342-1357, 1970.
- 3.6 M. F. Becker, D. J. Kuizenga, and A. E. Siegman, "Harmonic mode locking of the Nd:YAG laser," *IEEE J. Quantum Electron.*, vol. QE-7, pp. 95-97, 1971.
- 3.7 O. P. McDuff and S. E. Harris, "Nonlinear theory of the internally loss-modulated laser," *IEEE J. Quantum Electron.*, vol. QE-3, pp. 101-111, 1967.
- 3.8 H. Haken and M. Pauthier, "Nonlinear theory of multimode action in loss modulated lasers," *IEEE J. Quantum Electron.*, vol. QE-4, pp. 445-459, 1968.
- 3.9 J. R. Fontana, "Theory of spontaneous mode locking in lasers using a circuit model," *IEEE J. Quantum Electron.*, vol. QE-8, pp. 699-703, 1972.
- 3.10 D. M. Kim, S. Marathe, and T. A. Rabson, "Eigenfunction analysis of mode-

- locking process," *J. Appl. Phys.*, vol. 44, pp. 1673-1675, 1973.
- 3.11 H. A. Haus, "A theory of forced mode locking," *IEEE J. Quantum Electron.*, vol. QE-11, pp. 323-330, 1975.
- 3.12 D. J. Kuizenga and A. E. Siegman, "FM and AM mode locking of the homogeneous laser - Part I: Theory," *IEEE J. Quantum Electron.*, vol. QE-6, pp. 694-708, 1970.
- 3.13 D. J. Kuizenga and A. E. Siegman, "FM and AM mode locking of the homogeneous laser - Part II: Experimental results in a Nd:YAG laser with internal FM modulation," *IEEE J. Quantum Electron.*, vol. QE-6, pp. 709-715, 1970.
- 3.14 G. T. Maker and A. I. Ferguson, "Frequency-modulation mode locking of a diode-pumped Nd:YAG laser," *Opt. Lett.*, vol. 14, pp. 788-790, 1989.
- 3.15 U. Keller, K. D. Li, B. T. Khuri-Yakub, D. M. Bloom, K. J. Weingarten, and D. C. Gerstenberger, "High-frequency acousto-optic mode locker for picosecond pulse generation," *Opt. Lett.*, vol. 15, pp. 45-47, 1990.
- 3.16 T. Juhasz, S. T. Lai, and M. A. Pessot, "Efficient short-pulse generation from a diode-pumped Nd:YLF laser with a piezoelectrically induced diffraction modulator," *Opt. Lett.*, vol. 15, pp. 1458-1460, 1990.
- 3.17 G. T. Maker and A. I. Ferguson, "Frequency modulation mode-locking and Q-switching of diode-laser-pumped Nd:YLF laser," *Electron. Lett.*, vol. 25, pp. 1025-1026, 1989.
- 3.18 S. Basu and R. L. Byer, "Continuous-wave mode-locked Nd:glass laser pumped by a laser diode," *Opt. Lett.*, vol. 13, pp. 458-460, 1988.
- 3.19 D. W. Hughes, J. R. M. Barr, and D. C. Hanna, "Mode locking of a diode-laser-pumped Nd:glass laser by frequency modulation," *Opt. Lett.*, vol. 16, pp. 147-149, 1991.

- 3.20 A. A. Godil, K. D. Li, and D. M. Bloom, "Pulsed FM-modelocking of a Nd:BEL laser," *Opt. Lett.*, vol. 16, pp. 1243-1245, 1991.
- 3.21 K. D. Li, J. A. Sheridan, and D. M. Bloom, "Picosecond pulse generation in Nd:REL with a high-frequency acousto-optic mode-locker," *Opt. Lett.*, vol. 16, pp. 1505-1507, 1991.
- 3.22 F. Krausz, L. Turi, C. S. Kuti, and A. J. Schmidt, "Active mode locking of lasers by piezoelectrically induced diffraction modulation," *Appl. Phys. Lett.*, vol. 56, pp. 1415-1417, 1990.
- 3.23 J. Goodberlet, J. Jacobson, J. G. Fujimoto, P. A. Schulz, and T. Y. Fan, "Self-starting additive-pulse mode-locked diode-pumped Nd:YAG laser," *Opt. Lett.*, vol. 15, pp. 504-506, 1990.
- 3.24 U. Keller, T. K. Woodward, D. L. Sivco, and A. Y. Cho, "Coupled-cavity resonant passive mode-locked Nd:yttrium lithium fluoride laser," *Opt. Lett.*, vol. 16, pp. 390-392, 1991.
- 3.25 G. P. A. Malcolm, P. F. Curley, and A. I. Ferguson, "Additive-pulse mode locking of a diode-pumped Nd:YLF laser," *Opt. Lett.*, vol. 15, pp. 1303-1305, 1990.
- 3.26 K. J. Weingarten, D. C. Shannon, R. W. Wallace, and U. Keller, "Two gigahertz repetition rate, diode-pumped, mode-locked, Nd:YLF laser," *Opt. Lett.*, vol. 15, pp. 962-964, 1990.
- 3.27 F. Zhou, G. P. A. Malcolm, and A. I. Ferguson, "1-GHz repetition-rate frequency-modulation mode-locked neodymium lasers at 1.3  $\mu\text{m}$ ," *Opt. Lett.*, vol. 16, pp. 1101-1103, 1991.
- 3.28 P. A. Schulz and S. R. Henion, "5-GHz mode locking of a Nd:YLF laser," *Opt. Lett.*, vol. 16, pp. 1502-1504, 1991.

- 3.29 K. J. Weingarten, A. A. Godil, and M. Gifford, "FM mode-locking at 2.85 GHz using a microwave resonant optical modulator," *IEEE Photon. Techn. Lett.*, vol. 4, pp. 1106-1109, 1992.
- 3.30 H. P. Jenssen, R. F. Begley, R. Webb, and R. C. Morris, "Spectroscopic properties and laser performance of Nd<sup>3+</sup> in lanthanum beryllate," *J. Appl. Phys.*, vol. 47, pp. 1496-1500, 1976.
- 3.31 R. Scheps, J. Myers, E. J. Schimitschek, and D. F. Heller, "End-pumped Nd:BEL laser performance," *Optical Eng.*, vol. 27, pp. 830-834, 1988.
- 3.32 Spectra Diode Laboratories, SDL-2462-P1.
- 3.33 New Focus Inc., model 101X.
- 3.34 Hewlett Packard, model 54120A.
- 3.35 Inrad, model 5-14B, Autocorrelator.
- 3.36 J. M. Diels, J. J. Fontaine, I. C. McMichael, and F. Simoni, "Control and measurement of ultrashort pulse shapes (in amplitude and phase) with femtosecond accuracy," *Appl. Opt.*, vol. 24, pp. 1270-1282, 1985.
- 3.37 Advantest, model Q8381, optical spectrum analyzer.
- 3.38 U. Keller, J. A. Valdmanis, M. C. Nuss, and A. M. Johnson, "53 ps pulses at 1.32  $\mu\text{m}$  from a harmonic mode-locked Nd:YAG laser," *IEEE J. Quantum Electron.*, vol. 24, pp. 427-430, 1988.



## **Chapter 4    Space-Time Duality & Temporal Imaging**

This chapter first introduces the concept of space-time duality, which is then extended to the idea of temporal imaging. There is an interesting analogy between the spatial problem of Fresnel diffraction and the temporal problem of first order dispersion. This can be extended to introduce the idea of a time-lens as a dual of a spatial lens (regular lens). The time-lens is simply a quadratic optical phase modulator in time, which is approximated by a portion of a sinusoidal phase modulator. Thus, by using phase modulators as lenses and grating pairs as dispersive elements, complete temporal imaging systems can be constructed in exact duality with spatial imaging systems. There is a host of exciting applications of these ideas like time reversal, signal processing, active pulse compression, and time-microscopy of fast optical events. The ideas and results presented in this chapter on the space-time duality are summarized in Table 4.1.

### **4.1    Fresnel Diffraction & Temporal Dispersion**

There exists an interesting analogy between the spatial problem of Fresnel

SPACE	TIME
Transverse coordinate, $x$	Time, $t$
Spatial frequency, $k_x$	Frequency of envelope, $(\omega - \omega_0)$
Propagation constant, $k_0$	Carrier frequency, $\omega_0$
Fresnel propagation to distance $z$ : tran. func. = $\exp(-j z k_x^2 / 2k_0)$ $z$	First order temporal dispersion, $\mu^{-1}$ : tran. func. = $\exp[-j(\omega - \omega_0)^2 / 2\mu]$ $k_0\mu^{-1} = \omega_0\mu^{-1}$
Lens : transmittance = $\exp(-j \frac{k_0}{2f} x^2)$ $f$ = focal-length	Time-lens : transmittance = $\exp(-j \frac{\omega_0}{2f_T} t^2)$ $f_T$ = focal-time
Law of Imaging : $\frac{1}{d_1} + \frac{1}{d_2} = \frac{1}{f}$	Law of temporal imaging : $\mu_1 + \mu_2 = \frac{\omega_0}{f_T}$

Table 4.1 Space-time duality.

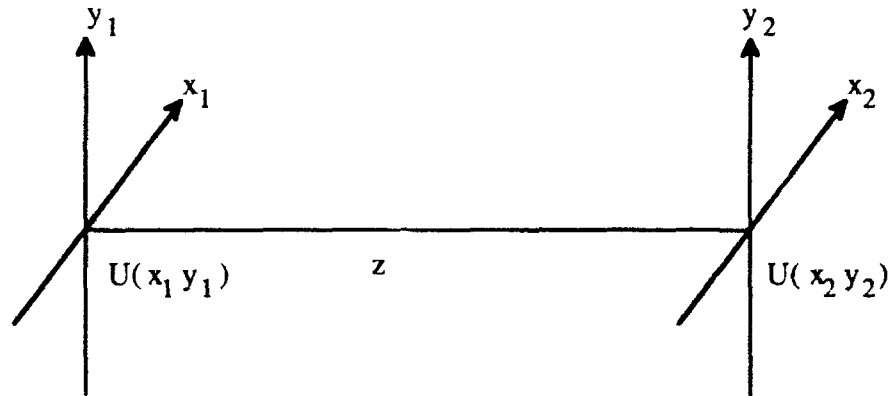


Figure 4.1 Transverse field distribution of monochromatic light propagating through free space  $z$ .

diffraction and the temporal problem of first order dispersion, first realized by Treacy [4.1]. Fresnel diffraction is an approximation to the general Rayleigh-Sommerfeld diffraction formula [4.2]. Consider (Fig. 4.1) a field distribution  $U(x_1, y_1)$  of monochromatic light at some plane  $x_1 y_1$ , then after propagating a distance  $z$  to the plane  $x_2 y_2$ , the field distribution is given within the Fresnel approximation as [4.2],

$$U(x_2, y_2) = \frac{\exp(jk_0 z)}{j\lambda_0 z} \int \int_{-\infty}^{\infty} U(x_1, y_1) \exp\left\{j \frac{k_0}{2z} [(x_2 - x_1)^2 + (y_2 - y_1)^2]\right\} dx_1 dy_1 \quad (4.1)$$

where  $\lambda_0$  is the optical wavelength and  $k_0$  is the propagation constant,  $2\pi/\lambda_0$ . To illustrate the duality between this phenomenon and temporal dispersion, the discussion will now be limited to one transverse dimension. Assuming  $U(x_1, y_1) = U(x_1)U(y_1)$  and writing only the  $x$  part,

$$U(x_2) = \exp(jk_0 z) \frac{1}{\sqrt{j\lambda_0 z}} \int_{-\infty}^{\infty} U(x_1) \exp\left[j\frac{k_0}{2z}(x_2 - x_1)^2\right] dx_1 \quad (4.2)$$

The above is simply a convolution integral representing a linear space-invariant system. Hence Fresnel diffraction can be expressed as a transfer function in the spatial frequency domain by Fourier transforming the impulse response. This yields

$$H(k_x) = \exp(jk_0 z) \exp(-j \frac{z}{2k_0} k_x^2) \quad (4.3)$$

Here,  $k_x$  is the propagation constant in the  $x$  direction and is given by  $2\pi f_x$ , where  $f_x$  is the spatial frequency in the  $x$  direction. Ignoring the constant phase term, the transfer function is simply a quadratic phase shift in  $k_x$ . In other words, space propagation is dispersive for spatial frequencies. This is the basis for the analogy with temporal dispersion discussed later in this section. The above equation can also be derived by considering plane-wave propagation in the spatial frequency domain. Since each spatial frequency (plane wave) is an eigen-solution of the wave equation, propagation through a distance  $z$  is very simply written as

$$U(k_x, z) = \exp(jk_z z) U(k_x, 0) \quad (4.4)$$

where  $k_z$ , the propagation constant in the  $z$  direction, is given as

$$k_z = \sqrt{k_0^2 - k_x^2} = k_0 \sqrt{1 - k_x^2/k_0^2} \quad (4.5)$$

The paraxial approximation,  $k_x^2/k_0^2 \ll 1$ , yields

$$k_z = k_0 - \frac{k_x^2}{2k_0} \quad (4.6)$$

Substituting the above in Eq. 4.4, gives

$$U(k_x, z) = \exp(jk_0 z) \exp(-j \frac{z}{2k_0} k_x^2) U(k_x, 0) \quad (4.7)$$

The above equation immediately leads to Eq. 4.3, showing that the paraxial approximation is the same as the Fresnel approximation.

Now, Fresnel diffraction is compared with temporal dispersion. A purely dispersive linear system has no loss and hence the general form of its transfer function is  $\exp[j\phi(\omega)]$ . For an optical pulse centered at the carrier frequency  $\omega_0$ ,  $\phi(\omega)$  is expressed as a Taylor series [4.1]. This yields

$$\phi(\omega) = \phi_0 + \tau(\omega - \omega_0) - \frac{(\omega - \omega_0)^2}{2\mu} \quad (4.8)$$

where  $\phi_0$  is a constant phase,  $\tau$  is the group delay, and  $\mu^{-1}$  is the group delay dispersion. For pulses more than a few hundred femtosecond wide and dispersion from grating pairs, prism pairs or fibers all higher order dispersion terms are completely negligible. The input and output pulses to the temporal dispersion system are expressed as

$$A(t) = u_1(t) \exp(-j\omega_0 t) \quad (4.9)$$

$$B(t) = u_2(t) \exp(-j\omega_0 t) \quad (4.10)$$

where  $u_1(t)$  and  $u_2(t)$  are the envelopes of the respective pulses and are complex in

general. Comparing Eq. 4.8 with the exponent in Eq. 4.3 shows that, except for a pulse delay, the envelope of the input pulse sees a similar transfer function to that for Fresnel diffraction but with  $k_x$  and  $x$  corresponding to  $\omega - \omega_0$  and  $t$  respectively. In the spatial case the beam displacement corresponding to pulse delay is zero as expected. To obtain the output pulse from the input, we take the Fourier transform of the input, multiply by  $\exp[j\phi(\omega)]$  (Eq. 4.8), and then take the inverse transform. The complete result is [4.1]

$$B(t' + \tau) = \sqrt{\frac{\mu}{2\pi}} \exp\left\{j\left[\phi_0 - \frac{\pi}{4} - \omega_0(t' + \tau)\right]\right\} \int u_1(t) \exp\left[j\frac{\mu}{2}(t - t')^2\right] dt \quad (4.11)$$

For grating dispersion  $\mu^{-1}$  is proportional to the grating pair separation, which in the space-time analogy corresponds to the propagation distance  $z$ . The space-time duality is made very clear and striking by comparing Eqs. 4.11 and 4.2. Except for a pulse delay, the envelope of the output pulse in time ( $t$ ) behaves exactly like Fresnel diffraction in space ( $x$ ).

## 4.2 Temporal Imaging

Analyzing nonlinear optical interactions with short pulses, Akhmanov [4.3, 4.4] first realized the analogy between fields modulated in time (pulses) and space (finite spatial beams). Optical pulse compression was later compared with focusing in time [4.1]. Recently, Kolner and Nazarathy [4.5] took the space-time analogy one step further and proposed a time-domain analog to spatial imaging that allows for the distortionless expansion or compression of optical waveforms in time. This process is called temporal imaging. The ideas and analysis in this section follow from references [4.5 and 4.6]. Figure 4.2 shows a spatial imaging system and the corresponding analog in the time-

domain. Temporal dispersion, the analog of free space propagation, is realized by grating pairs in the figure. A spatial lens is ideally a quadratic phase shift in  $x$ . However, in practice it is usually approximated by a spherical surface. The corresponding analog in time-domain would be a quadratic phase modulator in time ( $t$ ). This is called a time-lens. In principle, this element can be realized by applying a voltage waveform, quadratic in time, to an electro-optic modulator. Temporal imaging is valid within the slowly varying envelope approximation (SVEA) and the analogy with spatial imaging also requires the paraxial approximation.

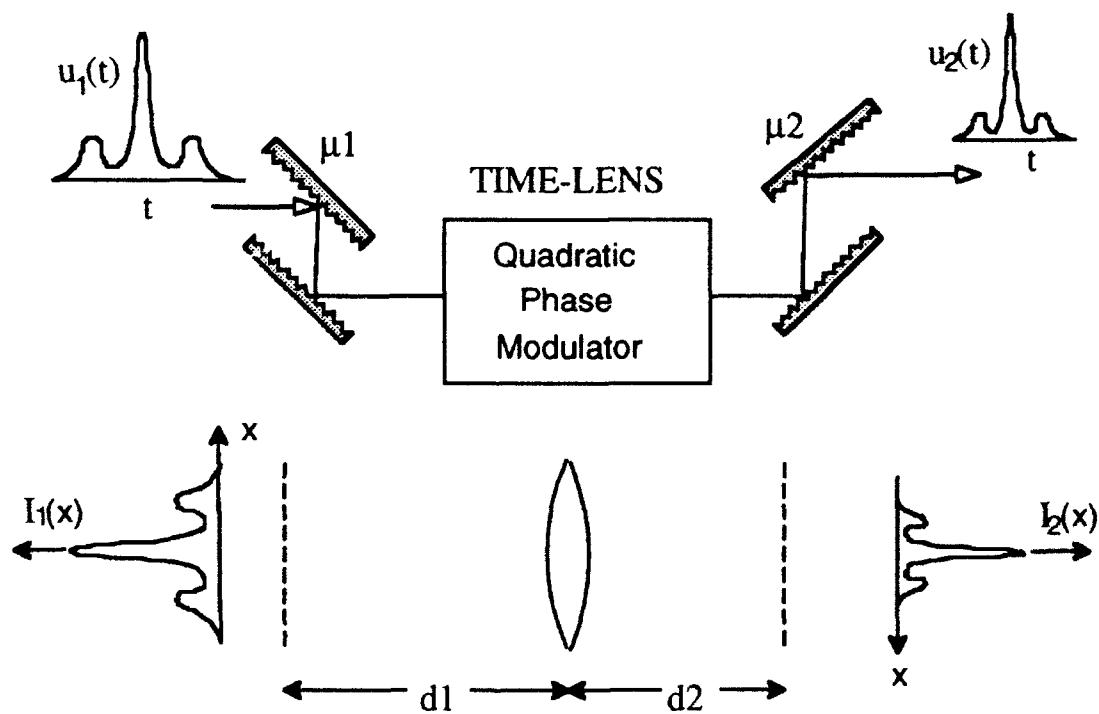


Figure 4.2 Temporal imaging shown as an analog of spatial imaging.

On the basis of this space-time analogy, temporal imaging is analyzed mathematically and the corresponding lens law is obtained. The transmission function of the time-lens, in analogy with a spatial lens [4.6], is written as

$$T_l(t) = \exp[-j \frac{\omega_0}{2f_T} t^2] \quad (4.12)$$

where  $f_T$  is defined as the focal-time of the lens. The envelope of the object pulse,  $u_1(t)$ , sees the dispersion on the object side ( $\mu_1^{-1}$ ), passes through the time-lens, and is followed by the dispersion on the image side ( $\mu_2^{-1}$ ). Using Eqs. 4.11 and 4.12, the envelope of the image pulse  $u_2(t)$  is obtained (ignoring a constant phase term),

$$u_2(t'' + \tau_1 + \tau_2) = \frac{\sqrt{\mu_1 \mu_2}}{2\pi} \int \exp(-j \frac{\omega_0}{2f_T} t'^2) \exp[j \frac{\mu_2}{2} (t' - t'')^2] \cdot \int u_1(t) \exp[j \frac{\mu_1}{2} (t - t')^2] dt dt' \quad (4.13)$$

where  $\tau_1$  and  $\tau_2$  are group delays on the object and image sides respectively. Now assume the condition

$$\mu_1 + \mu_2 = \omega_0 / f_T \quad (4.14)$$

Considerable simplification follows from Eq. 4.14, that is

$$u_2(t'' + \tau_1 + \tau_2) = \frac{\sqrt{\mu_1 \mu_2}}{2\pi} \exp(j \frac{\mu_2}{2} t''^2) \iint u_1(t) \exp(j \frac{\mu_1}{2} t^2) \exp(j \mu_1 t t') \exp(j \mu_2 t' t'') dt dt' \quad (4.15)$$



After considerable manipulation, the final result is

$$u_2(t'' + \tau_1 + \tau_2) = \sqrt{\frac{\mu_2}{\mu_1}} \exp\left[j \frac{\mu_2}{2\mu_1} (\mu_1 + \mu_2) t''^2\right] u_1\left(-\frac{\mu_2}{\mu_1} t''\right) \quad (4.16)$$

In the intensity, the exponential chirp function disappears, and a distortionless expansion or compression of the input pulse is obtained. This is called temporal imaging and Eq. 4.14 gives the corresponding law of temporal imaging. Magnification is simply given as,

$$M = -\mu_1/\mu_2 \quad (4.17)$$

For completeness, a formula for the dispersion of a grating pair is included here [4.1]. Consider the grating pair shown in Fig. 4.3. The dispersion ( $\mu^{-1}$ ) is

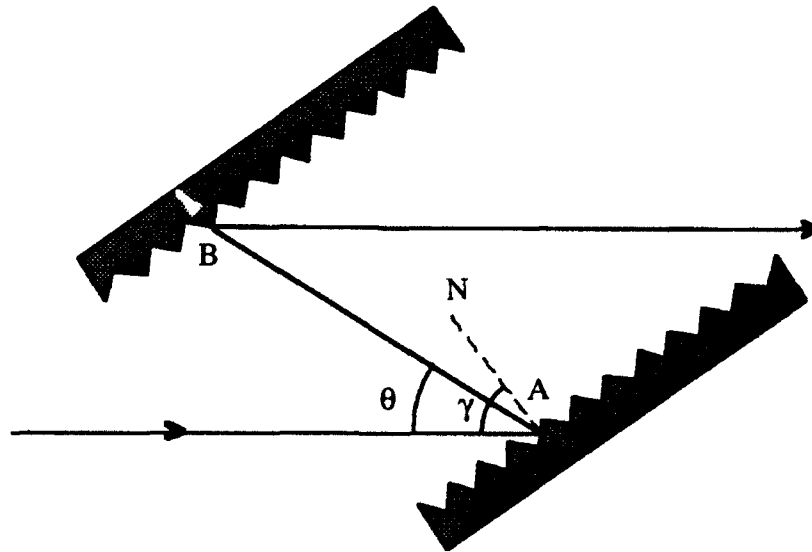


Figure 4.3 A dispersive grating pair showing the various parameters.

$$\mu^{-1} = \frac{b\lambda_0^3}{2\pi c_0^2 d^2 [1 - (\lambda_0/d - \sin \gamma)^2]} \quad (4.18)$$

where  $b$  is the slant distance AB between the gratings,  $c_0$  is the speed of light, and  $d$  is the grating period. The relation between angles  $\gamma$  and  $\theta$  for first-order diffraction is

$$\sin(\gamma - \theta) = \lambda_0/d - \sin \gamma \quad (4.19)$$

In practice, a single grating with retro-reflecting prism(s) is used in a 2-pass (grating-pair) or 4-pass (two grating-pairs) configuration.

### 4.3 The Sinusoidal Modulator as a Time-lens

It is not practically possible to realize the true quadratic phase modulation needed for an ideal time-lens. However, the required modulation can be approximated by a portion of a sinusoidal phase modulation. Near any extremum of the sinusoid, the modulation is essentially quadratic. Consider a sinusoidal phase modulation with frequency  $\omega_m$  and  $A$  radians of peak phase modulation (Fig. 4.4),

$$\phi(t) = A \cos(\omega_m t) \quad (4.20)$$

The corresponding quadratic approximation around  $t=0$  is

$$\phi(t) \approx A \left( 1 - \frac{\omega_m^2 t^2}{2} \right) \quad (4.21)$$

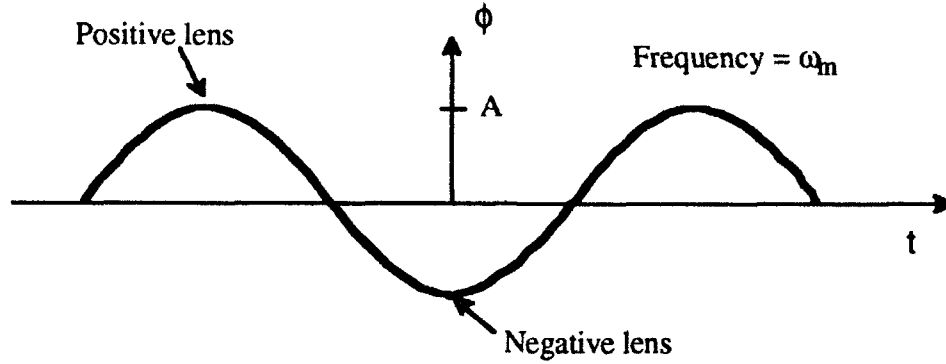


Figure 4.4 Time-lens approximated by portions of a sinusoidal phase modulation.

Comparing Eq. 4.21 with 4.12 gives the equivalent focal-time

$$f_T = \frac{\omega_0}{A\omega_m^2} \quad (4.22)$$

Assuming the time-lens has an effective FWHM (intensity) aperture [4.5, 4.7] of  $T_A = 1/\omega_m$ , the equivalent f-number is

$$f^\# = f_T \omega_m = \frac{\omega_0}{A\omega_m} \quad (4.23)$$

To calculate the resolution or minimum pulsewidth of the lens consider temporal focusing, time analog of gaussian beam focusing, of an input gaussian pulse of width  $\tau_p$  equal to  $1/\omega_m$ . This pulse completely fills the lens and is focused to a minimum pulsewidth  $\tau_0$ . In the usual convention, adopted in this thesis, pulsewidth is specified in intensity FWHM and gaussian beam size by  $w$  (center to intensity  $1/e^2$ ). Noting this difference, the formula for focusing of gaussian beams [4.8] is easily adopted to the temporal case. This gives,

$$\tau_0 = \frac{2.77}{A\omega_m} \quad (4.24)$$

As an example of a time-lens, consider a phase modulator with 10 radians of peak modulation at 5 GHz operating at 1.06  $\mu\text{m}$  wavelength. The parameters of such a lens are  $f_T = 0.18 \mu\text{sec}$ ,  $f^\# = 5,670$  and  $\tau_0 = 8.8 \text{ psec}$ . Thus, for practically useful time-lenses, large phase modulation is required at fairly high frequencies. Realizing these conditions in practice is far from trivial, as will be discussed in the next chapter, where the design and construction of a practical time-lens is presented.

**References**

- 4.1 E. B. Treacy, "Optical pulse compression with diffraction gratings," *IEEE J. Quantum Electron.*, vol. QE-5, pp. 454-458, 1969.
- 4.2 J. W. Goodman, *Introduction to Fourier Optics*, New York: McGraw-Hill, 1968, ch. 3 and 4.
- 4.3 S. A. Akhmanov, A. S. Chirkin, K. N. Drabovich, A. I. Kovrigin, R. V. Khokhlov, and A. P. Sukhorukov, "Nonstationary nonlinear optical effects and ultrashort light pulse formation," *IEEE J. Quantum Electron.*, vol. QE-4, pp. 598-605, 1968.
- 4.4 S. A. Akhmanov, A. P. Sukhorukov, and A. S. Chirkin, "Nonstationary phenomena and space-time analogy in nonlinear optics," *Soviet Physics JETP*, vol. 28, pp. 748-757, 1969.
- 4.5 B. H. Kolner and M. Nazarathy, "Temporal imaging with a time-lens," *Opt. Lett.*, vol. 14, pp. 630-632, 1989.
- 4.6 J. W. Goodman, *Introduction to Fourier Optics*, New York: McGraw-Hill, 1968, ch. 5.
- 4.7 B. H. Kolner, "Active pulse compression using an integrated electro-optic phase modulator," *Appl. Phys. Lett.*, vol. 52, pp. 1122-1124, 1988.
- 4.8 A. E. Siegman, *Lasers*, Mill Valley, CA : University Science Books, 1986, p. 675.

## Chapter 5 Time-Lens

As discussed in the last chapter, a time-lens is simply a quadratic phase modulator approximated by a portion of a sinusoidal phase modulator. For practically useful time-lenses, considerable modulation is required at fairly high frequencies. The approach taken here is to design a resonant microwave optical phase modulator in LiNbO<sub>3</sub> with multiple passes, based on an off-axis path in a stable optical resonator. In this chapter, the theory, design and construction of such a time-lens is presented. With 1 W of microwave power, 12 radians of phase modulation is obtained at 5.2 GHz and 1.06  $\mu\text{m}$  wavelength. This corresponds to a time-lens with 31 psec aperture and 6.7 psec resolution [5.1, 5.2]. Increasing the drive power to 13 W, improved the resolution to 1.9 psec. It should be noted that an optically resonant modulator is not a useful practical approach for time lenses, partly because of its inability to accept pulses at varied repetition rates.

### 5.1 Resonant Microwave Optical Modulator

Resonant microwave modulators based on electro-optic crystal loaded microwave

waveguides have been known for some time [5.3-5.11]. A modified design, presented here, leads to simpler construction and coupling. The lowest order mode of a  $\text{LiNbO}_3$ -loaded waveguide (Fig. 5.1) is  $\text{TE}_{10}$ , in which the electric field is parallel to the y-axis and is almost uniform inside the crystal. With the c-axis of the  $\text{LiNbO}_3$  parallel to the y-axis, phase modulation is obtained through the  $r_{33}$  electro-optic coefficient, for an optical beam traveling down the axis (z-axis) of the guide. By properly choosing the guide dimensions a and d, the phase velocity of the microwave mode is matched to that of the optical wave in the crystal. This phase-matching condition permits operation with a sufficiently long crystal to generate the required phase modulation. With the guide dimensions of Fig. 5.1, the  $\text{TE}_{10}$  mode is cutoff in the unloaded guide. Unloaded sections of guide at both ends of the crystal effectively confine the microwave resonance to the crystal-loaded region (Fig. 5.2). The optical beam traverses the resonator through the openings at both ends. The length L of the crystal is chosen such that a round trip in the resonator gives  $p \times 2\pi$  phase shift (resonance condition), where p is an integer and gives the order of the resonance ( $\text{TE}_{10p}$ ). An SMA launcher with its center conductor extended and almost touching the bottom wall (Fig. 5.1), providing a capacitive short, forms an efficient loop coupler. The position of the launcher is adjusted, through a slot on the top wall, to provide critical coupling ( $50 \Omega$ ). In the next few sub-sections, operation and performance of the modulator is analyzed in detail.

### 5.1.1 Dielectric Loaded Waveguide

A general method of obtaining solutions to Maxwell's equations is to consider the problem in terms of magnetic ( $\vec{A}$ ) and electric ( $\vec{F}$ ) vector potentials [5.12]. The relevant set of equations, for a source-free region, is :

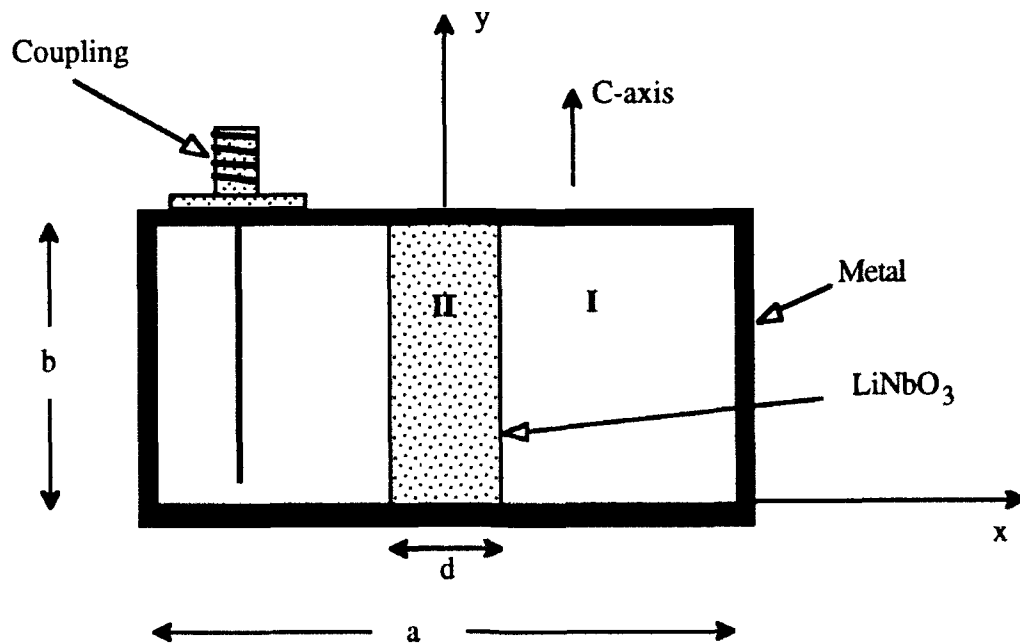


Figure 5.1 Cross-section of LiNbO<sub>3</sub> loaded waveguide used for the resonator (Fig. 5.2).

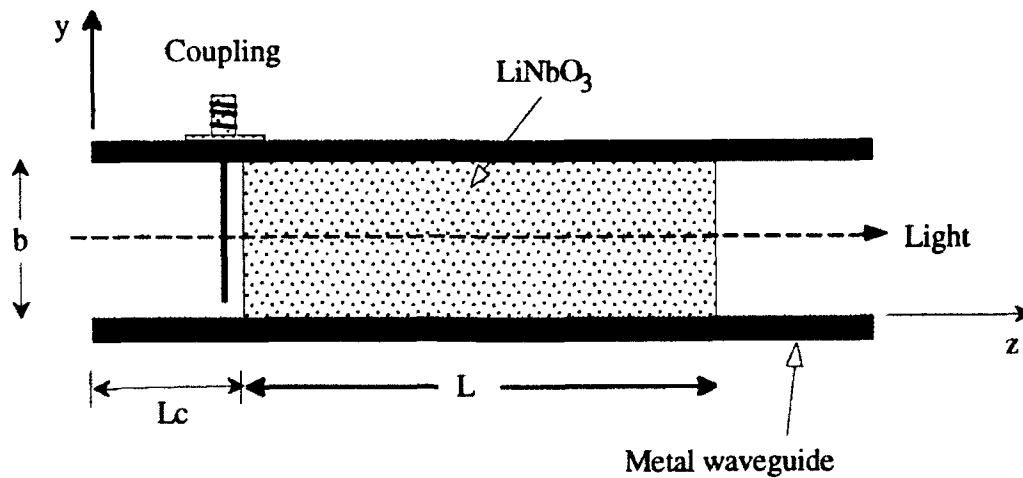


Figure 5.2 Side-view of resonator showing cutoff guide sections on each side to confine the energy and form a resonator. Light traverses the modulator along the  $z$ -axis.



$$\nabla^2 \bar{A} + k^2 \bar{A} = 0 \quad (5.1)$$

$$\nabla^2 \bar{F} + k^2 \bar{F} = 0$$

$$\begin{aligned} \bar{E} &= -\bar{\nabla} \times \bar{F} - j\omega\mu_0 \bar{A} + \frac{1}{j\omega\epsilon_0} \bar{\nabla}(\bar{\nabla} \cdot \bar{A}) \\ \bar{H} &= \bar{\nabla} \times \bar{A} - j\omega\epsilon_0 \bar{F} + \frac{1}{j\omega\mu_0} \bar{\nabla}(\bar{\nabla} \cdot \bar{F}) \end{aligned} \quad (5.2)$$

where  $k$  is the free-space propagation constant,  $k^2 = \omega^2 \mu_0 \epsilon_0$ . The modes in the LiNbO<sub>3</sub>-loaded waveguide of Fig. 5.1 are appropriately classified as transverse electric (TE<sup>x</sup>) and transverse magnetic (TM<sup>x</sup>) with respect to  $x$  [5.11, 5.12]. With respect to the propagation direction ( $z$ ), these are hybrid modes containing in general both  $E_z$  and  $H_z$ . An attempt to find TE<sup>z</sup> or TM<sup>z</sup> modes will prove unsuccessful, except for the TE<sup>z</sup><sub>m0</sub> case which is the same as TE<sup>x</sup><sub>m0</sub>. The analysis here, using vector potentials, will be limited to the mode of interest, TE<sub>10</sub> (= TE<sup>x</sup><sub>10</sub> = TE<sup>z</sup><sub>10</sub>). However, it is easily adaptable to other modes [5.11]. The TE<sup>x</sup> modes are expressed by the  $x$ -component of the electric vector potential, i.e.  $\bar{A} = 0$  and  $\bar{F} = \psi \bar{u}_x$ , where

$$\psi = \begin{cases} \psi_1, & \text{region I, } x > 0 \\ \psi_2, & \text{region II} \end{cases} \quad (5.3)$$

with region II the LiNbO<sub>3</sub> and region I the surrounding air (Fig. 5.1). The corresponding field distribution is,

$$E_x = 0, \quad E_y = -\frac{\partial \psi}{\partial z}, \quad E_z = \frac{\partial \psi}{\partial y} \quad (5.4)$$

$$H_x = \frac{1}{j\omega\mu_0} \left( \frac{\partial^2}{\partial x^2} + \omega^2\mu_0\epsilon \right) \psi \quad (5.5)$$

$$H_y = \frac{1}{j\omega\mu_0} \frac{\partial^2 \psi}{\partial x \partial y}, \quad H_z = \frac{1}{j\omega\mu_0} \frac{\partial^2 \psi}{\partial x \partial z}$$

Now  $\psi$  for the TE<sub>10</sub> mode, satisfying the boundary condition at the conducting walls, is chosen to be

$$\psi = \begin{cases} c_1 \sinh k_{x1}(a/2 - x) \exp(-jk_z z) & \text{--- I} \\ c_2 \cos(k_{x2}x) \exp(-jk_z z) & \text{--- II} \end{cases} \quad (5.6)$$

where  $c_1$  and  $c_2$  are unknown coefficients,  $k_z$  is the propagation constant in the  $z$  direction, and  $k_{x1}$  and  $k_{x2}$  are  $x$ -propagation constants in the two regions. This gives

$$k_z^2 = \omega^2\mu_0\epsilon_0 + k_{x1}^2 = \omega^2\mu_0\epsilon_2\epsilon_0 - k_{x2}^2 \quad (5.7)$$

Assuming isotropic dielectric behavior,  $\epsilon_2$  is the dielectric constant of LiNbO<sub>3</sub>. This assumption is only valid for TE<sub>m0</sub> modes, where the E-field (as given below) only has a component parallel to the  $c$ -axis of the LiNbO<sub>3</sub>. The E and H fields are, from Eqs. 5.4 and 5.5,

$$E_x = E_z = 0 \quad (5.8)$$

$$E_y = \begin{cases} jk_z c_1 \sinh k_{x1}(a/2 - x) \exp(-jk_z z) & \text{--- I} \\ jk_z c_2 \cos(k_{x2}x) \exp(-jk_z z) & \text{--- II} \end{cases} \quad (5.9)$$

$$H_x = \frac{k_z^2}{j\omega\mu_0} \begin{cases} c_1 \sinh k_{x1}(a/2 - x) \exp(-jk_z z) & \text{--- I} \\ c_2 \cos(k_{x2}x) \exp(-jk_z z) & \text{--- II} \end{cases} \quad (5.10)$$

$$H_y = 0 \quad (5.11)$$

$$H_z = \frac{k_z}{\omega\mu_0} \begin{cases} k_{x1}c_1 \cosh k_{x1}(a/2 - x) \exp(-jk_z z) & \text{--- I} \\ k_{x2}c_2 \sin(k_{x2}x) \exp(-jk_z z) & \text{--- II} \end{cases}$$

Matching the fields,  $E_y$  and  $H_z$  at  $x=d/2$ , gives the following two equations:

$$c_1 \sinh k_{x1}(a/2 - d/2) = c_2 \cos k_{x2} d/2 \quad (5.12)$$

$$k_{x1}c_1 \cosh k_{x1}(a/2 - d/2) = k_{x2}c_2 \sin k_{x2} d/2 \quad (5.13)$$

Dividing Eq. 5.13 by 5.12,

$$k_{x1} \coth k_{x1}(a - d)/2 = k_{x2} \tan k_{x2} d/2 \quad (5.14)$$

The propagation constant  $k_z$  is obtained by numerically solving Eqs. 5.7 and 5.14. Assuming a peak electric field of unity, the constants  $c_1$  and  $c_2$  follow from Eqs. 5.9 and 5.12.

$$c_1 = \frac{-j \cos(k_{x2} d/2)}{k_z \sinh k_{x1}(a - d)/2} \quad (5.15)$$

$$c_2 = -j/k_z$$

This completes the specification for the  $TE_{10}$  mode in terms of propagation constant and field distribution for a given set of parameters  $a$ ,  $d$ ,  $\epsilon_2$  and frequency  $\omega$ . The dielectric constant parallel to the  $c$ -axis of  $\text{LiNbO}_3$  is  $\epsilon_2 = 28$ . To maximize the modulation, especially with long crystals, it is essential to match the phase velocity of the microwave

mode to that of the optical wave in the crystal. This phase-matching condition gives,

$$k_z = n_e \omega / c_0 \quad (5.16)$$

where  $c_0$  is the speed of light in vacuum and  $n_e$  is the extra-ordinary index of LiNbO<sub>3</sub>. For a given frequency,  $k_z$ ,  $k_{x1}$  and  $k_{x2}$  are fixed by Eqs. 5.16 and 5.7. Thus, Eq. 5.14 simply becomes a relation between  $a$  and  $d$ .

$$\sqrt{n_e^2 - 1} \coth\left[\frac{\omega}{2c_0}(a - d)\sqrt{n_e^2 - 1}\right] = \sqrt{\epsilon_2 - n_e^2} \tan\left[\frac{\omega d}{2c_0}\sqrt{\epsilon_2 - n_e^2}\right] \quad (5.17)$$

### 5.1.2 Resonator and Resonance Condition

To satisfy the phase-matching condition (Eq. 5.16) the TE<sub>10</sub> mode of the microwave resonator formed from the LiNbO<sub>3</sub>-loaded waveguide, described in Sec. 5.1.1, must operate only slightly above cutoff. Thus, without the LiNbO<sub>3</sub> loading, the guide is cutoff for all modes. Therefore, unloaded sections of guide can be used at both ends to effectively confine the microwave energy to the crystal-loaded region (Fig. 5.2), forming a microwave resonator. The field attenuation coefficient for a cutoff TE<sub>10</sub> mode in these empty sections is [5.13],

$$\gamma = \frac{\pi}{a} \sqrt{1 - \left(\frac{\omega a}{c_0 \pi}\right)^2} \quad (5.18)$$

How much cutoff guide length ( $L_c$ ) is required on each side ? This can be estimated by considering radiative losses ( $P_r$ ) from the two open ends following the cutoff sections. The  $Q$  limited by radiative losses ( $Q_r = \omega W_0 / P_r$ ) should be, say, 10,000. The energy

stored in the resonator is,  $W_0 \sim \epsilon_2 \epsilon_0 E_0^2 V/2$ , where  $E_0$  is the field inside the crystal and  $V$  is the volume of the crystal. The radiated power is,  $P_r \sim abE_0^2 \exp(-2\gamma L_c)/\eta_0$ , where  $\eta_0$  is the free-space impedance. Using these estimates in the definition of  $Q_r$ , gives an upper estimate of  $L_c$ .

$$L_c \approx \frac{1}{2\gamma} \ln \left( \frac{2ac_0 Q_r}{\omega \epsilon_2 dL} \right) \quad (5.19)$$

where  $L$  is the length of the  $\text{LiNbO}_3$  crystal and  $Q_r$  is say 10,000.

The length  $L$  of the crystal is chosen such that a round trip in the resonator (Fig. 5.2) gives a  $p \times 2\pi$  phase shift, where  $p$  is an integer and gives the order of the resonance. This is known as the resonance condition and the corresponding resonant mode is labeled as  $\text{TE}_{10p}$ . There is an additional phase shift associated with the discontinuity ( $z=0, L$ ) between the  $\text{LiNbO}_3$ -loaded and the cutoff guide. Precisely speaking, the situation at the discontinuity is very complicated because many cutoff modes are excited to match the fields. However, assuming only a  $\text{TE}_{10}$  mode on each side, gives a simple solution here. A standing wave with a certain phase  $\phi$  exists in the  $\text{LiNbO}_3$ -loaded region with exponential tails in the cutoff sections. On the two sides of the discontinuity at  $z=0$ , the field may be written as

$$E_y = \begin{cases} E_L \cos(k_z z - \phi), & z \geq 0 \\ E_C \exp(\gamma z), & z \leq 0 \end{cases} \quad (5.20)$$

where  $k_z$  and  $\gamma$  are given by Eqs. 5.7 and 5.18 respectively and  $-\phi$  is one-half the reflection phase shift at the discontinuity. Matching the field and its derivative at  $z=0$ , gives:

$$\begin{aligned} E_C &= E_L \cos \varphi \\ \gamma E_C &= k_z E_L \sin \varphi \end{aligned} \quad (5.21)$$

Dividing the lower equation by the upper gives

$$\varphi = \tan^{-1}(\gamma/k_z) \quad (5.22)$$

Note that  $\varphi$  is always positive. This leads to the following resonance condition:

$$k_z L - 2\varphi + k_z L - 2\varphi = 2k_z L - 4\varphi = p \times 2\pi \quad (5.23)$$

or in terms of choosing  $L$  for a modulator operating at some frequency  $\omega$  in the  $TE_{10p}$  resonance,

$$L = \frac{p\pi + 2\varphi}{k_z}, \quad p = 0, 1, 2, 3, \dots \quad (5.24)$$

Note that  $TE_{100}$  is a perfectly acceptable resonant mode.

### 5.1.3 Ohmic Loss Q

The unloaded  $Q$  limited by ohmic losses in the metal walls,  $Q_R$ , is now calculated for the resonator described above. The procedure is similar to that described in section 2.3.2.

$$Q_R = \frac{\omega W_0}{P_R} \quad (5.25)$$

where  $W_0$  is the energy stored in the resonator and  $P_R$  is the resistive power dissipated in

the metal walls. To simplify the analysis, ignore end effects in the resonator (Sec. 5.1.2) or, equivalently, assume  $L$  is very large. Consider the stored energy when it is entirely electric in form.

$$W_0 = \frac{\epsilon}{2} \iiint |E_y|^2 dV \quad (5.26)$$

$$W_0 = W_{0C} + W_{0A} \quad (5.27)$$

where  $W_{0C}$  and  $W_{0A}$  are the energies stored in the crystal and the surrounding air respectively. Using Eqs. 5.9 and 5.15, leads to

$$W_{0C} = \frac{\epsilon_2 \epsilon_0}{8} b L d \left( 1 + \frac{\sin k_{x2} d}{k_{x2} d} \right) \quad (5.28)$$

$$W_{0A} = \frac{\epsilon_0}{8} \frac{b L}{k_{x1}} \frac{\cos^2(k_{x2} d/2)}{\sinh^2 k_{x1} (a-d)/2} [\sinh k_{x1} (a-d) - k_{x1} (a-d)] \quad (5.29)$$

The fraction of the electrical energy stored in the crystal is

$$\alpha = W_{0C}/W_0 \quad (5.30)$$

The surface current density on the metal walls is equal to the tangential magnetic field at the surface. This leads to a surface integral for dissipated power [5.14],

$$P_R = \frac{R_s}{2} \iint_S |H_s|^2 dS \quad (5.31)$$

where  $R_s$  is the surface resistivity of the metal wall. Using Eqs. 5.10, 5.11 and 5.15 and

much algebra, Eq. 5.31 is reduced to

$$P_R = \frac{R_s L}{\omega^2 \mu_0^2} \left\{ \frac{\cos^2(k_{x2} d/2)}{\sinh^2 k_{x1} (a-d)/2} \left[ \frac{b}{2} k_{x1}^2 + \frac{k_z^2 + k_{x1}^2}{4 k_{x1}} \sinh k_{x1} (a-d) - \frac{\omega^2 \mu_0 \epsilon_0}{4} (a-d) \right] + \frac{d}{4} \omega^2 \mu_0 \epsilon_2 \epsilon_0 + \frac{d \sin k_{x2} d}{4 k_{x2} d} (k_z^2 - k_{x2}^2) \right\} \quad (5.32)$$

Substituting Eqs. 5.28, 5.29 and 5.32 into Eq. 5.25, gives the  $Q$  due to ohmic losses ( $Q_R$ ). Microwave dielectric loss in  $\text{LiNbO}_3$  is characterized by the material  $Q$  ( $Q_m$ , Sec. 2.5). For  $\alpha$  (Eq. 5.30) very close to unity, the usual case, the combined effect of these two losses gives

$$1/Q_0 = 1/Q_R + 1/Q_m \quad (5.33)$$

#### 5.1.4 Analysis of Optical Modulation

If the electric field inside the crystal is assumed to be uniform in the transverse plane, the modulation field is given as (Eq. 5.20)

$$E_y(z, t) = E_L \cos(k_z z - \varphi) \cos \omega t, \quad 0 \leq z \leq L \quad (5.34)$$

The optical phase modulation  $\phi$  is calculated by following a thin cross-section of the light beam, polarized along the  $y$ -axis, which enters the crystal at time  $t_0$  from the left. This section is represented by the  $\delta$  function:  $\delta(t - t_0 - z n_e / c_0)$ . The incremental phase shift ( $d\phi$ ) over a small incremental distance  $dz$  is then

$$d\phi = \frac{2\pi}{\lambda_0} \Delta n_e(z, t) dz \quad (5.35)$$



where  $\lambda_0$  is the optical wavelength and the change in index  $\Delta n_e(z,t)$  is given by Eq. 2.6.

The total phase modulation for a single pass is

$$\phi(t_0) = \frac{\pi n_e^3 r_{33}}{\lambda_0} \int_0^L \int_{t_0}^{t_0 + n_e L/c_0} E_y(z,t) \delta(t - t_0 - z n_e/c_0) dt dz \quad (5.36)$$

where  $r_{33}$  is an electro-optic coefficient. Substituting Eq. 5.34 into Eq. 5.36 gives

$$\phi(t_0) = \frac{\pi n_e^3 r_{33}}{\lambda_0} \int_0^L E_L \cos(k_z z - \varphi) \cos \omega(t_0 + z n_e/c_0) dz \quad (5.37)$$

or

$$\phi(t_0) = \frac{\pi n_e^3 r_{33} E_L}{2 \lambda_0} \left[ \int_0^L \cos(\omega t_0 + \frac{\omega n_e z}{c_0} + k_z z - \varphi) dz + \int_0^L \cos(\omega t_0 + \frac{\omega n_e z}{c_0} - k_z z + \varphi) dz \right] \quad (5.38)$$

Introducing the two new parameters

$$u^+ = \frac{\omega L}{2} \left( \frac{n_e}{c_0} + \frac{k_z}{\omega} \right) \quad (5.39)$$

$$u^- = \frac{\omega L}{2} \left( \frac{n_e}{c_0} - \frac{k_z}{\omega} \right) \quad (5.40)$$

converts Eq. 5.38 to

$$\phi(t_0) = \frac{\pi n_e^3 r_{33} E_L}{2 \lambda_0} \left[ \int_0^L \cos(\omega t_0 - \varphi + \frac{2u^+}{L} z) dz + \int_0^L \cos(\omega t_0 + \varphi + \frac{2u^-}{L} z) dz \right] \quad (5.41)$$

and

$$\phi(t_0) = \frac{\pi n_e^3 r_{33} E_L L}{2\lambda_0} \left[ \frac{\sin u^+}{u^+} \cos(\omega t_0 - \varphi + u^+) + \frac{\sin u^-}{u^-} \cos(\omega t_0 + \varphi + u^-) \right] \quad (5.42)$$

For  $k_z L \gg 1$  and close to phase-matched operation,  $u^+ \gg 1$  and  $u^-$  is close to zero. The first term in Eq. 5.42 can then be neglected, giving

$$\phi(t_0) \approx \frac{\pi n_e^3 r_{33} E_L L}{2\lambda_0} \frac{\sin u^-}{u^-} \cos(\omega t_0 + \varphi + u^-) \quad (5.43)$$

for the exit modulation of a light beam entering from the left at  $t_0$ . It can be shown similarly that for a light beam entering the crystal from the right at  $t_0$ , the exit modulation is

$$\phi'(t_0) \approx \frac{\pi n_e^3 r_{33} E_L L}{2\lambda_0} \frac{\sin u^-}{u^-} \cos(\omega t_0 - \varphi - u^- + \frac{\omega n_e}{c_0} L) \quad (5.44)$$

Now the field  $E_L$  is related to the microwave power ( $P$ ) delivered to the resonator and the unloaded  $Q$  ( $Q_0$ ). From the energy definition of  $Q_0$ , it follows that

$$W_0 = P Q_0 / \omega \quad (5.45)$$

where  $W_0$  is the energy stored in the resonator. Assuming that the electric field inside the crystal is uniform in the transverse plane,  $W_0$  is evaluated when it is entirely electric in form by using Eq. 5.34. This yields

$$W_0 = \frac{\epsilon_2 \epsilon_0}{2} \frac{bd}{\alpha} \int_0^L E_L^2 \cos^2(k_z z - \varphi) dz \quad (5.46)$$

where  $\alpha$ , the fraction of the electrical energy stored in the crystal, is given by Eq. 5.30 and is almost unity in practice. Combining Eq. 5.46 with Eq. 5.24 gives

$$W_0 = \frac{\epsilon_2 \epsilon_0 b d}{4\alpha} E_L^2 \left[ L + \frac{\sin 2\phi}{k_z} \right] \quad (5.47)$$

Equations 5.47, 5.45 and 5.43 give the final result for peak phase modulation,

$$\phi = \frac{\pi n_e^3 r_{33}}{\lambda_0} \sqrt{\frac{\alpha P Q_0}{\omega \epsilon_2 \epsilon_0 b d [L + \sin(2\phi)/k_z]}} L \frac{\sin u^-}{u^-} \quad (5.48)$$

## 5.2 Multipass Modulator using Off-axis Optical Resonator

An off-axis beam in a stable optical resonator reflects back and forth, creating in general an elliptical pattern of spots on the spherical mirrors [5.15, 5.16]. The beam size is maintained indefinitely upon reflections if the input beam is matched to the resonator eigenmode. In effect, for the right beam size, the focusing power of the resonator exactly compensates the diffraction effect for each round trip. This idea has been used to create a multipass Raman gain cell [5.17, 5.18]. In this section, this concept is extended to create a multipass optical path through the modulator described in Sec. 5.1.

Consider a resonator made-up of a flat mirror and a spherical concave mirror, as shown in Fig. 5.3. A ray is introduced into the resonator in the plane of the flat mirror at

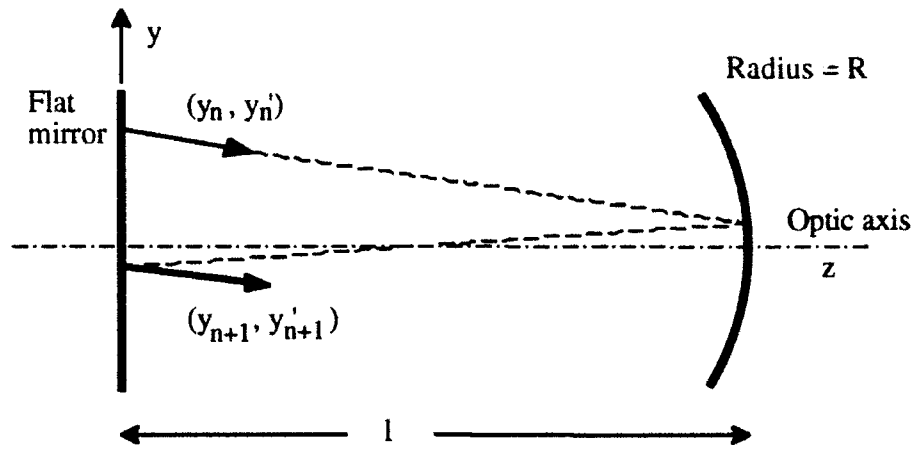


Figure 5.3 An off-axis path in a stable optical resonator. The orthogonal dimension  $x$  is not shown in the figure.

position  $(x_0, y_0)$  in the  $xy$  plane with slopes  $x'_0$  and  $y'_0$  in the two directions with respect to  $z$ . The  $x$  and  $y$  coordinates of the ray in the plane of the flat mirror on the  $n$ th round trip are given within the paraxial approximation as [5.17],

$$x_n = x_0 \cos n\theta + \sqrt{l(R-l)} x'_0 \sin n\theta \quad (5.49)$$

$$y_n = y_0 \cos n\theta + \sqrt{l(R-l)} y'_0 \sin n\theta \quad (5.50)$$

where  $l$  is the length of the resonator,  $R$  is the radius of the curved mirror and  $\theta$  is the angle between successive reflected spots [5.17],

$$\theta = \cos^{-1}(1 - 2l/R) \quad (5.51)$$

The waist size of the resonator eigen-mode at the flat mirror is

$$w_0 = \sqrt{\frac{\lambda_0}{\pi}} [l(R-l)]^{1/4} \quad (5.52)$$

From Eqs. 5.49 and 5.50, it follows that the successive reflected spots on the flat mirror, in general, lie on an ellipse. However if  $x_0 = x'_0 = 0$ , then  $x_n = 0$  and the reflected spots move up and down on a straight line in the  $y$ -direction. Equation 5.50 can be alternatively written in phasor form as,

$$y_n = Y \sin(n\theta + \rho) \quad (5.53)$$

$$\text{where } Y = \sqrt{y_0^2 + l(R-l)y_0'^2} \quad (5.54)$$

$$\rho = \tan^{-1} \frac{y_0}{y_0' \sqrt{l(R-l)}}$$

Thus  $y_n$  is simply the projection on the imaginary axis of a phasor of amplitude  $Y$  starting at angle  $\rho$  and rotating by  $\theta$  for each round trip.

The complete configuration for a mutipass modulator is shown in Fig. 5.4. The beam, mode matched to the optical resonator eigen-mode (Eq. 5.52), clears the top of the flat mirror and enters the modulator from the left. The beam reflects back and forth between the two mirrors, walks down the  $y$ -direction and back up again, finally leaving again at its point of entry. A circulator may be used to separate the exiting beam. The spacings,  $d_1$  and  $d_2$ , between the modulator and the mirrors are properly adjusted to provide constructive modulation between the passes. Comparing Figs. 5.3 and 5.4 shows that the effective length of the resonator is

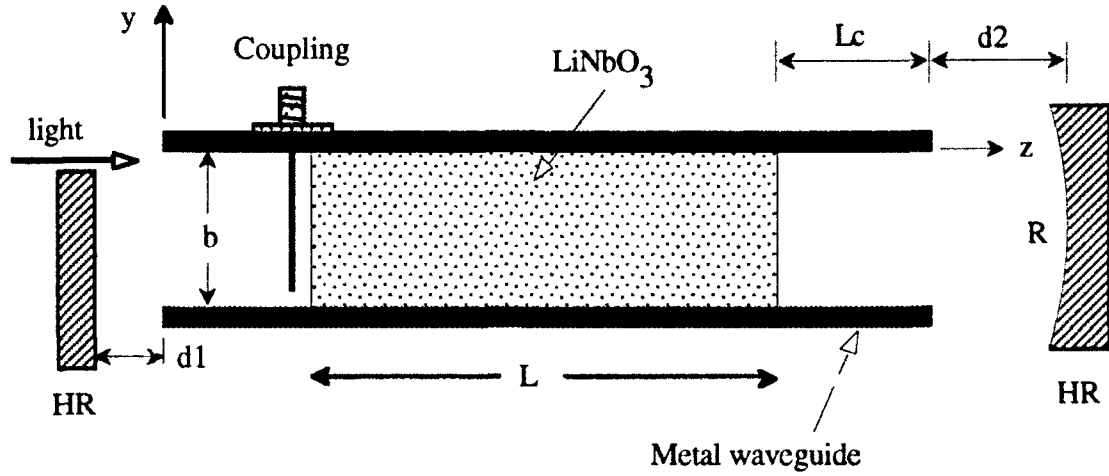


Figure 5.4 Side-view of multipass modulator. HR = highly reflecting.

$$l = d_1 + d_2 + 2L_c + L/n_e \quad (5.55)$$

The following condition is imposed by Eq. 5.53 if  $N$  round trips are obtained.

$$\begin{aligned} y_N &\equiv y_0 \\ \Rightarrow \sin(N\theta + \rho) &= \sin \rho \end{aligned} \quad (5.56)$$

The above is satisfied if  $N\theta + \rho = \pi - \rho$ . Hence  $\rho$  is given as

$$\rho = \frac{1}{2}(\pi - N\theta) \quad (5.57)$$

Now the design equations of this section are combined with the modulator design of Sec. 5.1. It is known that an aperture of  $4.6w_0$  (4.6 x waist size) for gaussian beams produces less than 1% diffraction ripple [5.19]. This rule is used for choosing the width  $d$  of the LiNbO<sub>3</sub> crystal and the beam clearance at the top of the flat mirror.

$$d = 4.6w_0 \quad (5.58)$$

$$y_0 - y_1 = Y\theta \cos \rho = 4.6w_0 \quad (5.59)$$

where  $w_0$  is given by Eq. 5.52. The total excursion of the beam is  $Y - y_0 = Y(1 - \sin \rho)$ .

Thus, the height of the crystal is chosen as

$$b = Y(1 - \sin \rho) + 4.6w_0 \quad (5.60)$$

If  $d1$  and  $d2$  are properly adjusted, the total multipass modulation is simply the single pass modulation (Eq. 5.48) multiplied by the number of passes.

$$A = 2N\phi \quad (5.61)$$

A good design should optimize all the parameters to maximize the total modulation  $A$ .

### 5.2.1 Multipass Synchronization

As discussed in the last section,  $d1$  and  $d2$  have to be properly adjusted to provide constructive modulation between all the passes. The proper values of  $d1$  and  $d2$  are calculated in this section. This is carried out in two steps. First  $d2$  is calculated to provide maximum modulation for one round trip. Then  $d1$  is calculated to synchronize the modulation between all the round trips. Consider a cross-section of light which enters the  $\text{LiNbO}_3$  crystal from the left at time  $t_0$ . From Eq. 5.43, maximum phase is accumulated for  $t_0 = (-\phi - u^-)/\omega$ . This cross-section of light after reflecting from the curved mirror enters the crystal from the right at time  $\tau$  given by

$$\tau = \frac{n_e L}{c_0} + \frac{2}{c_0}(L_c + d_2) - \frac{(\varphi + u^-)}{\omega} \quad (5.62)$$

From Eq. 5.44, maximum phase is accumulated from the right if

$$\omega \tau - \varphi - u^- + \omega n_e L / c_0 = m 2\pi \quad (5.63)$$

where  $m$  is an integer. Substituting Eq. 5.62 into 5.63 gives

$$d_2 = \frac{c_0}{\omega}(m\pi + u^- + \varphi) - n_e L - L_c \quad (5.64)$$

The above is simplified further by using Eqs. 5.24 and 5.40.

$$d_2 = (m - p - \frac{u^-}{\pi} - \frac{\varphi}{\pi}) \frac{\lambda_m}{2} - L_c \quad (5.65)$$

where  $\lambda_m$  is the free space microwave wavelength,  $\lambda_m = c_0 / 2\pi\omega$ . This value of  $d_2$  ensures that the round-trip modulation is twice the single-pass modulation. A round trip time around the optical resonator equal to an integer ( $M$ ) multiple of the modulation period, provides constructive modulation between all the round trips. This gives the second synchronization condition.

$$d_1 + d_2 = M \lambda_m / 2 - n_e L - 2L_c \quad (5.66)$$

After satisfying both conditions, the total modulation is simply  $A=2N\phi$  as stated in Eq. 5.61.



### 5.2.2 Modulator as Thermal Lens

In practice, for the design discussed in the next section,  $Q_R$  is much greater than  $Q_m$ . Therefore most of the microwave power is dissipated as heat in the  $\text{LiNbO}_3$  crystal, which is then mostly removed by conduction to the top and bottom metal walls (Fig. 5.1). The heat dissipated by convection to the air around the crystal is negligible, unless cold air is blown through the resonator. The heat conduction to the walls leads to a temperature distribution and hence an index profile. This behaves like a lens in the  $y$ -direction and may greatly disturb the mutipass scheme of Sec. 5.2. The focal length of this thermal lens is calculated here to quantify the problem. Assume heat flow is limited to the  $y$ -dimension as shown in Fig. 5.5. Applying energy conservation to a thin slice of  $\text{LiNbO}_3$ , as depicted in Fig. 5.5, in steady state gives

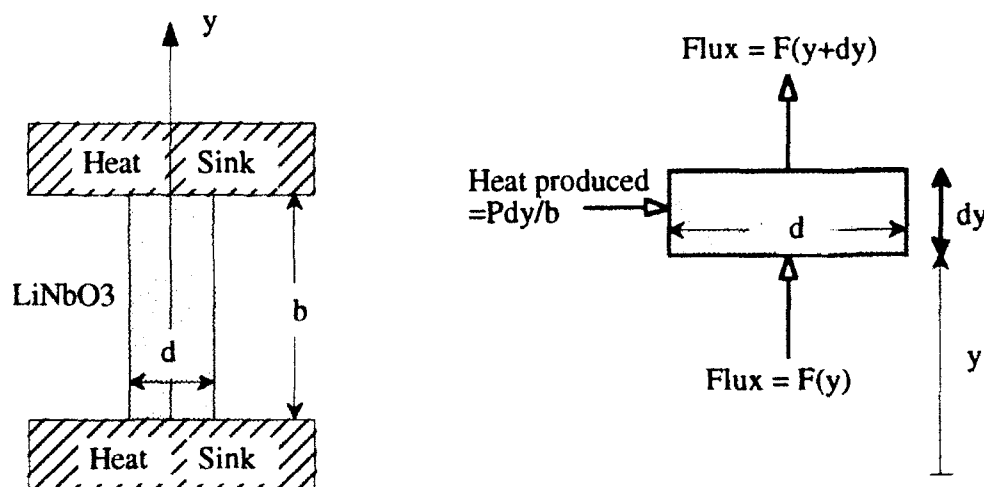


Figure 5.5 Analysis of heat conduction in the modulator.

$$F(y) + \frac{P}{b} dy = F(y + dy) = F(y) + \frac{dF}{dy} dy \quad (5.67)$$

where  $P$  is the microwave power delivered to the modulator and  $F$  is the heat flux given by,

$$F(y) = -\sigma L d \frac{dT}{dy} \quad (5.68)$$

$T$  is the temperature and  $\sigma$  is the thermal conductivity of  $\text{LiNbO}_3$ . Combining the above two equations leads to,

$$\frac{d^2 T}{dy^2} = -\frac{P}{\sigma L b d} \quad (5.69)$$

$$\frac{d^2 n_e}{dy^2} = \frac{dn_e}{dT} \frac{d^2 T}{dy^2} = -\frac{P dn_e/dT}{\sigma L b d} \quad (5.70)$$

Optical phase  $\phi$  and thermal focal-length  $f_{th}$  are related by

$$\phi = 2\pi n_e L / \lambda_0 \quad (5.71)$$

$$\frac{d^2 \phi}{dy^2} = 2\pi \frac{L}{\lambda_0} \frac{d^2 n_e}{dy^2} = -\frac{2\pi}{\lambda_0} \frac{1}{f_{th}} \quad (5.72)$$

Combining Eqs. 5.70 and 5.72, leads to the final result,

$$f_{th} = \frac{\sigma b d}{P dn_e/dT} \quad (5.73)$$

where  $\sigma = 5.6 \text{ W/(m.K)}$  and  $dn_e/dT = 4.3 \times 10^{-5} / \text{K}$  [5.20, 5.21].

### 5.3 Design & Construction of Time-Lens

Based on the ideas and analyses presented in this chapter, a specific design of the time-lens was carried out at 1.06  $\mu\text{m}$  wavelength. This was then constructed and experimentally characterized both in the microwave and optical domains. The departures from theory are pointed out. For this first attempt at making a time-lens, the emphasis was on a workable design and not a thoroughly optimized one.

Keeping some practical constraints in mind and going through the design once, it was quickly decided that the modulator frequency should be around 5 GHz. The largest boule diameter for commercially grown  $\text{LiNbO}_3$  is three inches, and therefore  $L$  should be about 7 cm. Equation 5.17 gives the relation between  $a$  and  $d$  for phase-matching at 5 GHz. This gives  $a = 0.95$  cm and  $d = 0.225$  cm. With  $L = 6.8$  cm, the  $\text{TE}_{104}$  resonance is at  $f = 4.92$  GHz with  $k_z = 2.13$   $\text{cm}^{-1}$ ,  $\phi = 0.974$  radians,  $u^- = 0.29$  and  $\sin(u^-)/u^- = 0.985$ . Cutoff guide length on each side is  $L_c = 1.25$  cm. Optimum values of  $d_1$  and  $d_2$  are  $d_1 = d_2 = 0.61$  cm. The waist size of the eigen-mode should be  $w_0 = d/4.6 = 0.49$  mm. This gives the radius of the curved mirror, which is rounded-off to  $R = 700$  cm. The corresponding  $\theta = 0.2$  radians and the height of the crystal is chosen as  $b = 1.15$  cm (Eq. 5.60). The  $Q$  limited by ohmic losses is  $Q_R = 5900$  and the fraction of the electrical energy stored in the crystal is  $\alpha = 0.97$ . From Chapter 2, the estimated value of  $Q_m$  (material  $Q$ ) at 5 GHz is about 4000, and thus a  $Q_0$  of about 2400 is expected. For 1 W of microwave power,  $\phi = 0.76$  radians is given by Eq. 5.48. The number of round trips that will fit inside the crystal is about  $N = 13$ . Thus the expected total multipass modulation is  $A = 19.8$  radians. The  $\text{LiNbO}_3$  crystal was slightly wedged between the input and output faces to eliminate spurious reflections. The metal waveguide was constructed from two different

pieces. The bottom and the two side-walls were machined out of one aluminum piece. The top plate, as a separate piece, comes down between the side-walls and is held in place by eight screws on each side. Both pieces were plated with  $2.5\text{ }\mu\text{m}$  of gold. The construction is carefully done to minimize the contact resistance between the two pieces. This is an important consideration. Poor contact can severely affect the  $Q$  of the resonator. The assembly is carried out by first placing the  $\text{LiNbO}_3$  crystal in the bottom piece and holding it in position by two small dabs of Krazy glue. Any extra glue will noticeably lower the  $Q$ . The top plate is lowered in and while some pressure is applied, the eight screws are tightened from each side. An SMA launcher is introduced into the resonator through the top plate (Figs. 5.1, 5.2). Its center conductor is extended to almost touch the bottom wall of the resonator. This provides a capacitive short and effectively forms a loop coupler. The area of the loop, hence coupling, is adjusted by moving the  $x$ -position of the launcher in a slot in the top plate. Usually the  $z$ -position of the loop is chosen at a place of maximum  $H_z$ . After the modulator is assembled, microwave characterization is carried out as discussed in the next section.

### 5.3.1 Modulator Characterization

The  $S_{11}$  parameter of the modulator is measured on a network analyzer [5.22] and is shown in Fig. 5.6. All the various observed resonances could not at first be clearly identified and there was some uncertainty even about the desired  $\text{TE}_{104}$  resonance. An interesting technique based on perturbation methods is used to identify the different resonances. It can be shown very elegantly [5.23] that the shift in the resonant frequency ( $\omega_0$ ) of a cavity resonant mode  $(\vec{E}_0, \vec{H}_0)$  when the surface of the cavity is perturbed (deformed) at one place by a small volume  $\Delta V$ , is given by

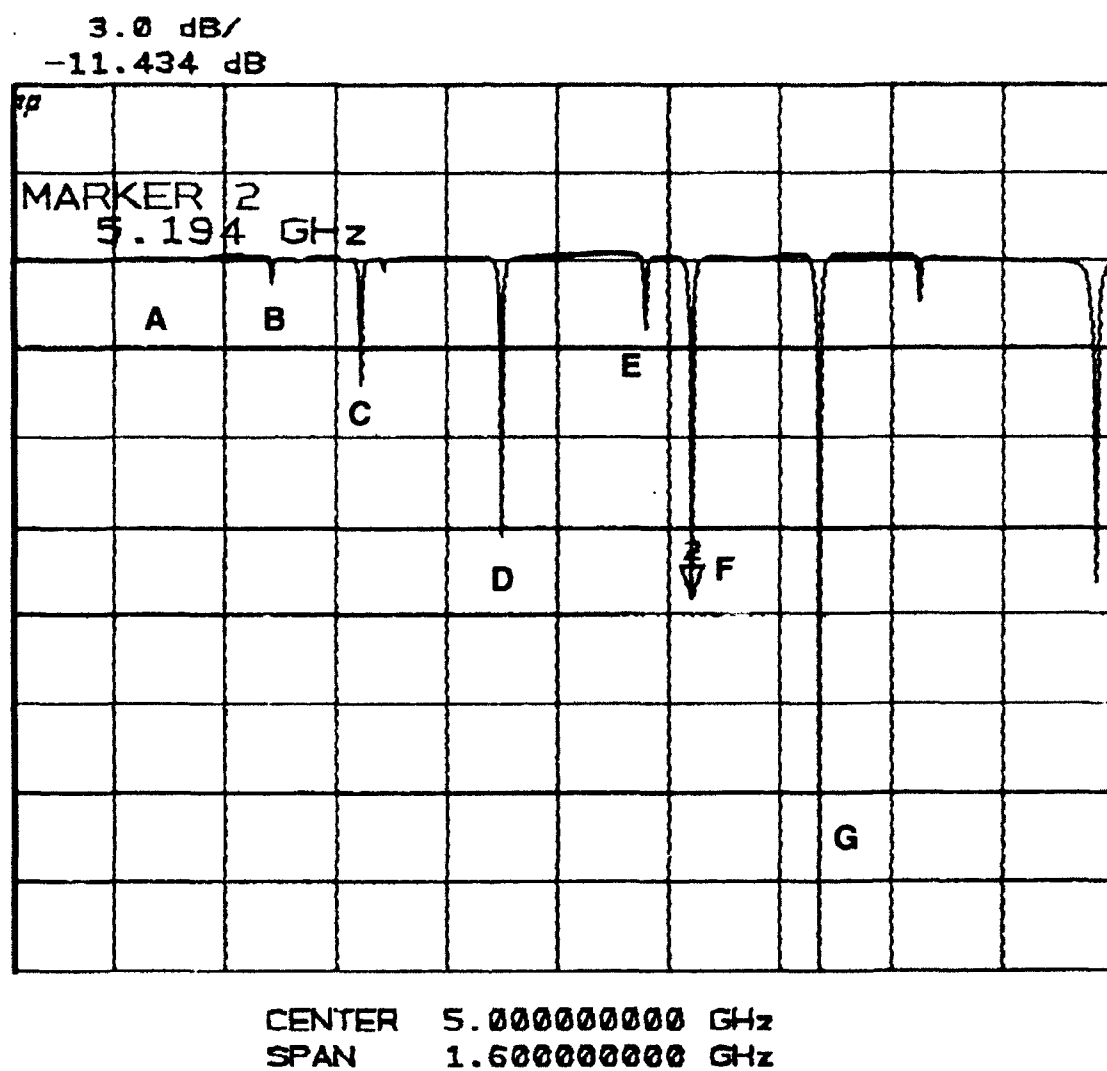


Figure 5.6  $S_{11}$  of modulator as measured on a network analyzer. The first seven resonances are labeled by letters A-G. For this measurement, resonance A is not noticeably excited because of weak coupling.

$$\Delta\omega = \omega - \omega_0 \approx \frac{\omega_0}{4W_0}(\mu|H_0|^2 - \epsilon|E_0|^2)\Delta V \quad 5.74$$

where  $W_0$  is the energy stored in the resonant mode and  $|H_0|$  and  $|E_0|$  are the magnitudes of the magnetic and electric fields respectively in the perturbed region  $\Delta V$ . A stainless-steel ball bearing of 1.5 mm diameter is glued to a thread and slid along the length of the resonator by one of the side-walls. The ball represents the small perturbation  $\Delta V$ . The change in resonant frequency of various resonances is measured as a function of the z-position of the ball along the length of the resonator. This is proportional to  $|H_z|^2$  for  $TE_{10p}$  modes because all other fields are zero at the side-walls. Seven resonances are identified in Fig. 5.6 by letters A-G. The measured change in resonant frequency of these resonances as a function of the ball position is shown in Figs. 5.7a and 5.7b. It is clear from this measurement that resonances A, B, C, D and G correspond to resonant modes  $TE_{100}$ ,  $TE_{101}$ ,  $TE_{102}$ ,  $TE_{103}$  and  $TE_{105}$  respectively. Both the resonances E and F have five humps in their profile. This is very surprising because there is only one  $TE_{104}$  mode and therefore both resonances can not be accounted for. This mystery was finally resolved when optical modulation measurements were made, as discussed next.

The modulator was driven with a microwave synthesizer and a solid state amplifier. About 1 W of power was delivered. Phase modulation is measured (Sec. 2.4) by observing the sidebands produced on a single-frequency laser, using a scanning Fabry-Perot cavity as an optical spectrum analyzer. Single-pass modulation was measured on resonance for the resonances E and F as a function of the beam position  $y$  in the crystal. For a pure  $TE_{10}$  mode, there should be no variation with respect to  $y$ . The measured results are shown in Fig. 5.8. The large modulation variation with  $y$  proves that neither of them is a pure  $TE_{104}$  resonance. This led to investigating the possibility of

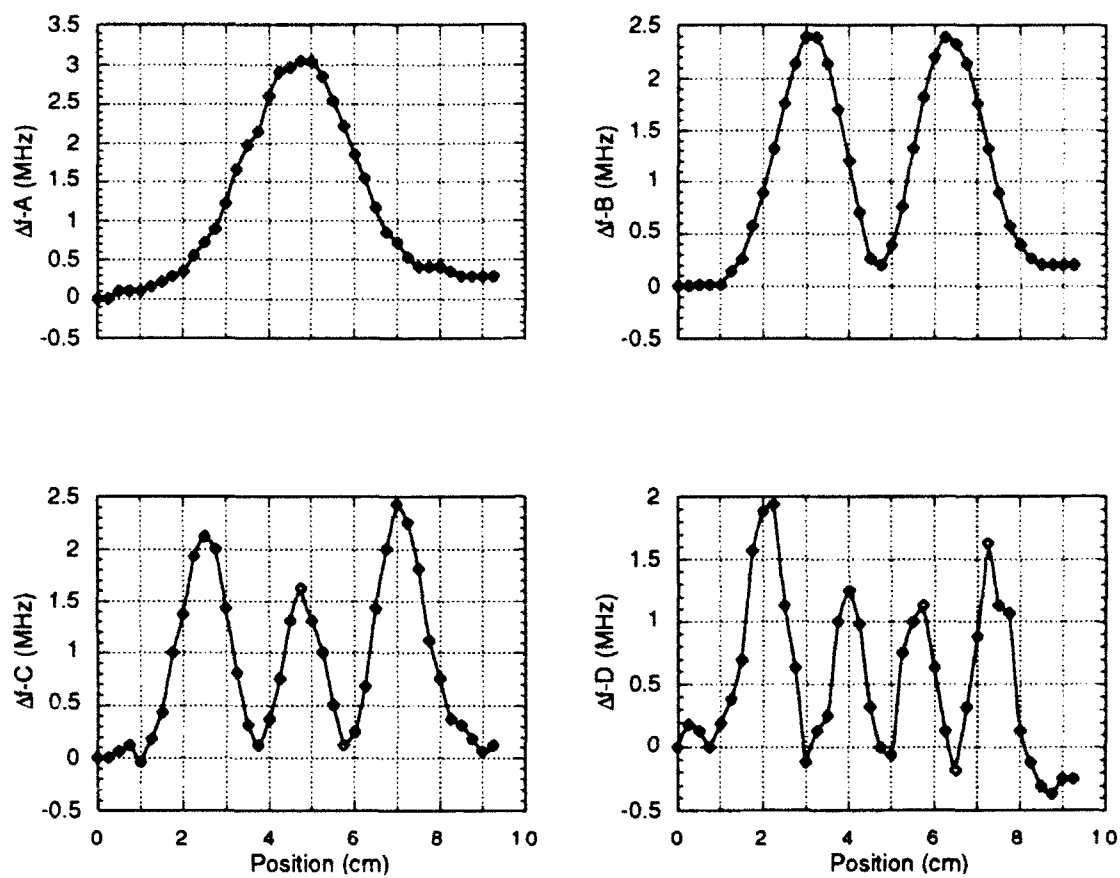


Figure 5.7a Change in resonant frequency as a function of the ball position for resonances A, B, C and D.

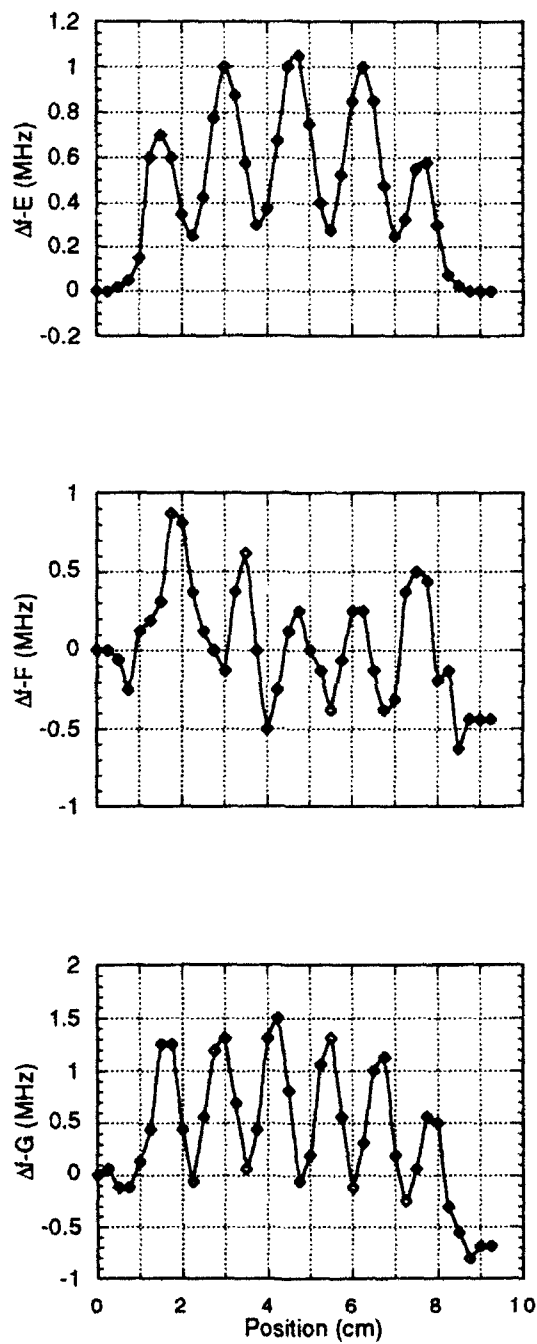


Figure 5.7b Change in resonant frequency as a function of the ball position for resonances E, F and G.



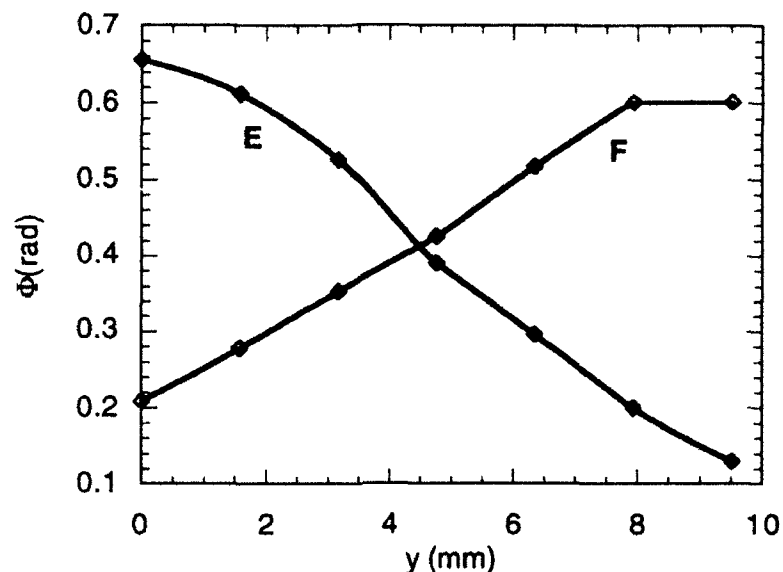


Figure 5.8 Modulation as a function of the beam position  $y$  for the two resonances E and F. Microwave power = 1 W.

mixed modes [5.24]. If there is a resonant mode not far in frequency from the  $TE_{104}$  mode, then for sufficient coupling between the two, significant mode-mixing is possible. Thus the resonant frequencies of some other families of modes is now approximately calculated [5.11]. The cutoff frequencies of some other waveguide modes are:  $TM_{01}^x = 9.9$  GHz,  $TE_{11}^x = 5.31$  GHz,  $TE_{12}^x = 7.55$  GHz, and  $TE_{20}^x = 13.5$  GHz. The resonant frequency of the  $TE_{110}^x$  mode is about 5.33 GHz. The actual frequency of this mode will be lower because the  $z$ -component of the electric field increases the effective dielectric constant from 28. Therefore, it is most likely that the  $TE_{110}^x$  mode is close enough to the  $TE_{104}$  mode that the resultant mixed-modes ( $TE_{110}^x + \kappa TE_{104}$ ,  $\kappa TE_{110}^x - TE_{104}$ ) are indeed resonances E and F, where  $\kappa$  is a mode-mixing coefficient. This conclusion also qualitatively predicts the results of Figs. 5.7b and 5.8. From Fig. 5.6, resonances E and F

are at 5.12 GHz and 5.194 GHz respectively. The unloaded  $Q$  ( $Q_0$ ) of both resonances was measured, using the procedure described in Sec. 2.4, to be about 1900. This is not far from the expected value of 2400 as discussed earlier. It was realized that resonance F was more uniform and reproducible, and hence was used for the multipass modulator. In retrospect, the mode-mixing problem could have been avoided by choosing the guide dimensions more carefully.

### 5.3.2 Microwave Resonator Frequency Tuner

Applications of the time-lens, as discussed in the next chapter, require a frequency tuning of the resonance over a range of about 80 MHz. In addition, the tuner should be low loss. Thus, it was decided to implement a dielectric tuner as shown in Fig. 5.9. A 0.2 cm thick, 1 cm diameter  $\text{LiNbO}_3$  disk was used as a dielectric perturbation and is moved inside the resonator via a nylon screw. The  $z$ -position of the tuner was chosen at a place of maximum E-field, which in the present case is the center of the resonator. By turning the screw clockwise, the disk could be moved closer to the  $\text{LiNbO}_3$  crystal, causing more

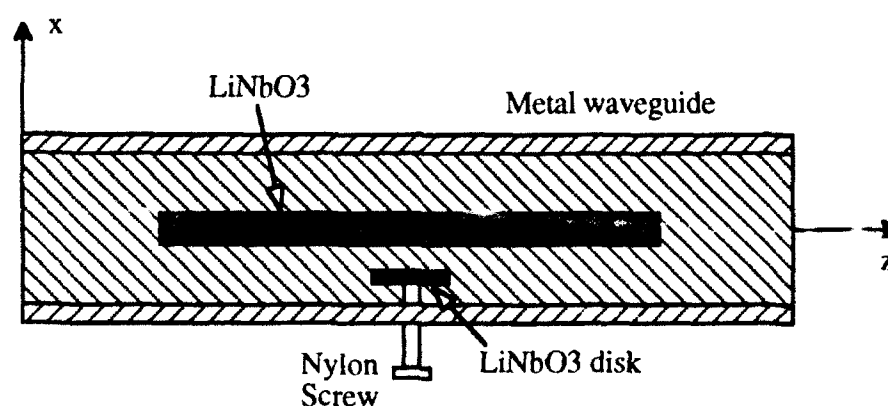


Figure 5.9 Resonator with the top removed showing the tuner.

perturbation of the electric field of the resonant mode, and hence changing the resonant frequency. A tuning range of about 100 MHz was obtained for resonance F, without compromising  $Q_0$ .

## 5.4 Measurement of Multipass Modulator

The multipass modulator (Fig. 5.4) is implemented using an off-axis optical resonator as discussed in Sec. 5.2. A 1.06  $\mu\text{m}$  Nd:YAG laser entered the multipass modulator after mode-matching with one or two lenses. The mode-size was measured by the rotating razor-blade technique [5.25], and the modulated return beam was separated using a Faraday circulator. Multipassing was observed through an IR viewer as the input beam position, angle, and the mirror angles were adjusted. The spacings,  $d_1$  and  $d_2$ , between the modulator and the mirrors were properly chosen and then adjusted to maximize the modulation. Approximately,  $d_1 = 0.2$  cm and  $d_2 = 2.9$  cm. The modulation was measured by looking at the spectrum through a scanning Fabry-Perot cavity. For phase modulation  $A$  at frequency  $\omega$ , the sidebands produced on the optical carrier  $\omega_0$  are given by,

$$\exp j(\omega_0 t + A \sin \omega t) = \sum_{q=-\infty}^{+\infty} J_q(A) \exp j(\omega_0 + q\omega)t \quad (5.75)$$

where  $q$  is an integer and  $J_q$  is the  $q$ th order Bessel function. For 1 W of microwave power at 5.2 GHz, measured phase modulation as a function of detuning in  $d_2$  is shown in Fig. 5.10. It can be shown that zero modulation is obtained for a certain detuning in  $d_2$  ( $\Delta d_2^0$ ). This corresponds to the situation where modulation accumulated in the first  $N/2$  round-trips is exactly canceled in the other half. It can be easily shown that such detuning is given by,

$$\Delta d_2^0 = \lambda_m / 2N \quad (5.76)$$

This is a useful expression for inferring  $N$  from Fig. 5.10. Thus  $N = 12$ .

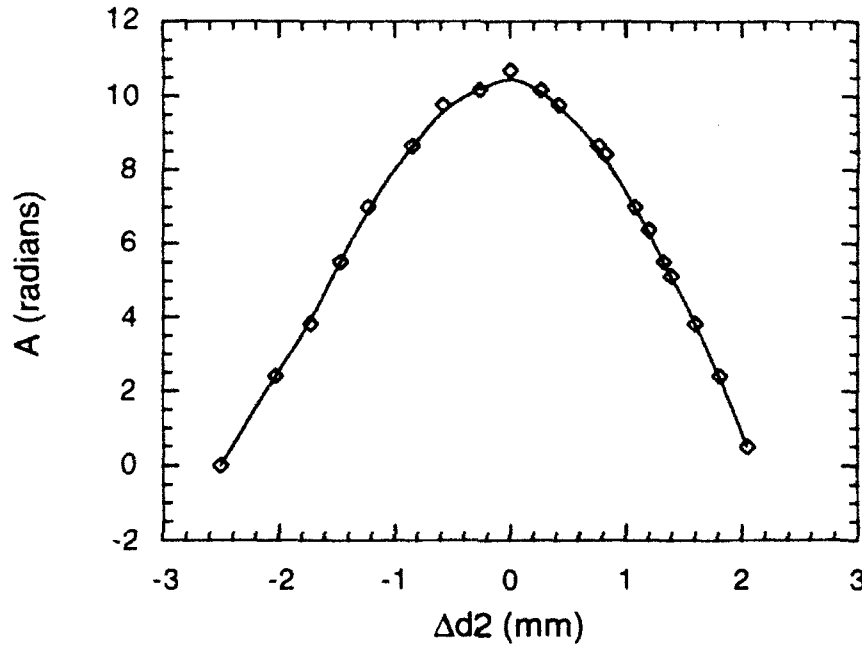


Figure 5.10 Measured multipass modulation as a function of detuning in  $d_2$ , for 1 W of cw power at 5.2 GHz.

The measured spectrum [5.26] of the modulated light is shown in Fig. 5.11. The spacing between the two peaks in the spectrum is  $2A\omega$ . From this,  $A$  is inferred to be 13 radians. Now the modulator is driven with 13 W of microwave power, obtained from a traveling wave tube amplifier. At this power level, the thermal-lens effect (Sec. 5.2.2) disrupted the multipass scheme. Therefore the average power was reduced by duty cycling at 10%. The corresponding spectrum is shown in Fig. 5.12, from which the peak modulation is inferred to be 44 radians. The optical transmission through the multipass modulator is about 50 % and the quality of the exiting beam visually looks very good.

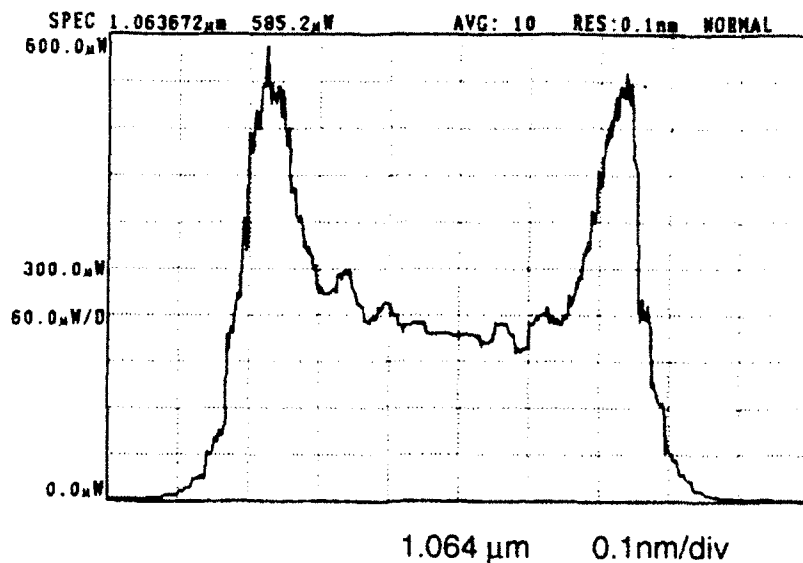


Figure 5.11 Measured spectrum of modulated light. RF power = 1 W cw.

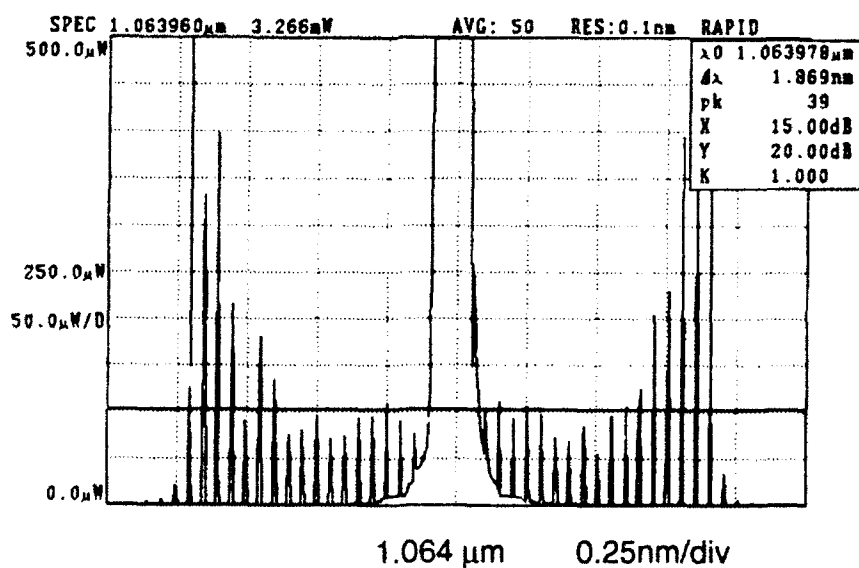


Figure 5.12 Measured spectrum of modulated light. RF power = 13 W, 10% duty cycle. The spikes in the spectrum are an anomaly of the measurement setup, using a pulsed laser source and the sampling rate of the spectrum analyzer.

**References**

- 5.1 A. A. Godil, B. A. Auld, and D. M. Bloom, "Time-lens producing picosecond optical pulses," IEEE Lasers and Electro-optics Society Annual Meeting, Boston, MA, 1992.
- 5.2 A. A. Godil, B. A. Auld, and D. M. Bloom, "Time-lens producing 1.9 psec optical pulses," Submitted to *Appl. Phys. Lett.*, July 1992.
- 5.3 H. Brand, B. Hill, E. Holtz, and G. Wencker, "External light modulation with low microwave power," *Electron. Lett.*, vol. 2, pp. 317, 1966.
- 5.4 M. E. El-Shandwily and S. M. El-Dinary, "Traveling-wave coherent light-phase modulator," *IEEE Trans. Microwave Theory and Techniques*, vol. MTT-20, pp. 132-137, 1972.
- 5.5 G. M. Carter, "Tunable high-efficiency microwave frequency shifting of infrared lasers," *Appl. Phys. Lett.*, vol. 32, pp. 810-812, 1978.
- 5.6 N. H. Tran, T. F. Gallagher, J. P. Watjen, G. R. Janik, and C. B. Carlisle, "High efficiency resonant cavity microwave optical modulator," *Appl. Opt.*, vol. 24, pp. 4282-4284, 1985.
- 5.7 T. F. Gallagher, N. H. Tran, and J. P. Watjen, "Principles of a resonant cavity optical modulator," *Appl. Opt.*, vol. 25, pp. 510-514, 1986.
- 5.8 E. Bonek, G. Schiffner, R. Pisecker, and F. Kohl, "Proposed CO<sub>2</sub>-laser standing-wave intracavity coupling modulator for a 53-GHz cw signal," *IEEE J. Quantum Electron.*, vol. QE-10, pp. 128-130, 1974.
- 5.9 G. Magerl and E. Bonek, "Broadband electronically tunable resonant microwave modulators for CO<sub>2</sub> lasers," *Appl. Phys. Lett.*, vol. 34, pp. 452-454, 1979.

- 5.10 E. Bonek, M. Knecht, G. Magerl, K. Preis, and K. R. Richter, "Coupling and tuning of trapped-mode microwave resonators," *AEU*, vol. 32, pp. 209-214, 1978.
- 5.11 E. Bonek and G. Magerl, "Propagation characteristics of dielectrically loaded rectangular waveguides for laser beam modulators," *AEU*, vol. 28, pp. 499-506, 1974.
- 5.12 R. F. Harrington, *Time-Harmonic Electromagnetic Fields*, New York : McGraw-Hill book company, Inc., 1961, p. 129-130.
- 5.13 S. Ramo, J. R. Whinnery, and T. Van Duzer, *Fields and Waves in Communication Electronics*, New York : John Wiley & Sons, Inc., 1984, ch. 8.
- 5.14 S. Ramo, J. R. Whinnery, and T. Van Duzer, *Fields and Waves in Communication Electronics*, New York : John Wiley & Sons, Inc., 1984, ch. 10.
- 5.15 D. Herriott, H. Kogelnik, and R. Kompfner, "Off-axis paths in spherical mirror interferometers," *Appl. Opt.*, vol. 3, pp. 523-526, 1964.
- 5.16 D. R. Herriott and H. J. Schulte, "Folded optical delay lines," *Appl. Opt.*, vol. 4, pp. 883-889, 1965.
- 5.17 W. R. Trutna and R. L. Byer, "Multiple-pass Raman gain cell," *Appl. Opt.*, vol. 19, pp. 301-312, 1980.
- 5.18 B. Perry, R. O. Brickman, A. Stein, E. B. Treacy, and P. Rabinowitz, "Controllable pulse compression in a multiple-pass-cell Raman laser," *Opt. Lett.*, vol. 5, pp. 288-290, 1980.
- 5.19 A. E. Siegman, *Lasers*, Mill Valley, CA : University Science Books, 1986, p. 667.
- 5.20 M. J. Weber, *Handbook of Laser Science and Technology*, Boca Raton, Florida:

CRC Press, Inc., 1986, vol. 4, part 2, p. 52.

- 5.21 M. J. Weber, *Handbook of Laser Science and Technology*, Boca Raton, Florida: CRC Press, Inc., 1986, vol. 3, part 1, p. 187.
- 5.22 Hewlett-Packard, 8510B, network analyzer.
- 5.23 R. F. Harrington, *Time-Harmonic Electromagnetic Fields*, New York : McGraw-Hill book company, Inc., 1961, p. 317-319.
- 5.24 W. H. Louisell, *Coupled mode and parametric electronics*, New York : John Wiley & Sons, Inc., 1960.
- 5.25 Y. Suzaki and A. Tachibana, "Measurement of the  $\mu\text{m}$  sized radius of Gaussian laser beam using the scanning knife-edge," *Appl. Opt.*, vol. 14, pp. 2809-2810, 1975.
- 5.26 Advantest, model Q8381, optical spectrum analyzer.



## **Chapter 6    Experiments with Time-Lens**

Space-time duality and temporal imaging were discussed in Chapter 4, which led to the concept of time-lenses. The theory, design and construction of a multipass microwave modulator, as a time-lens, was presented in Chapter 5. Here, temporal focusing with the time-lens is experimentally demonstrated. With 1 W of cw microwave power at 5.2 GHz, 45 psec pulses at 1.06  $\mu\text{m}$  were temporally focused to 6.7 psec (FWHM). Increasing the drive power to 13 W, at 10% duty cycle, produced 1.9 psec pulses [6.1, 6.2]. The aperture of the time-lens is about 31 psec.

### **6.1   Pulses from CW Light**

As a first demonstration of the time-lens, pulses are created from cw light. A 1.06  $\mu\text{m}$  single-frequency laser [6.3] is passed through the multipass modulator, followed by a 4-pass grating (1700 ln/mm) dispersion [6.4], adjusted close to the focal-time of the time-lens. Parts of the cw light, which fall within the positive time-lens part of the sinusoidal modulation, are focused in time and create a pulse train. The grating dispersion is adjusted to optimize the pulsewidth. This pulse train at 5.2 GHz, with some background light, is

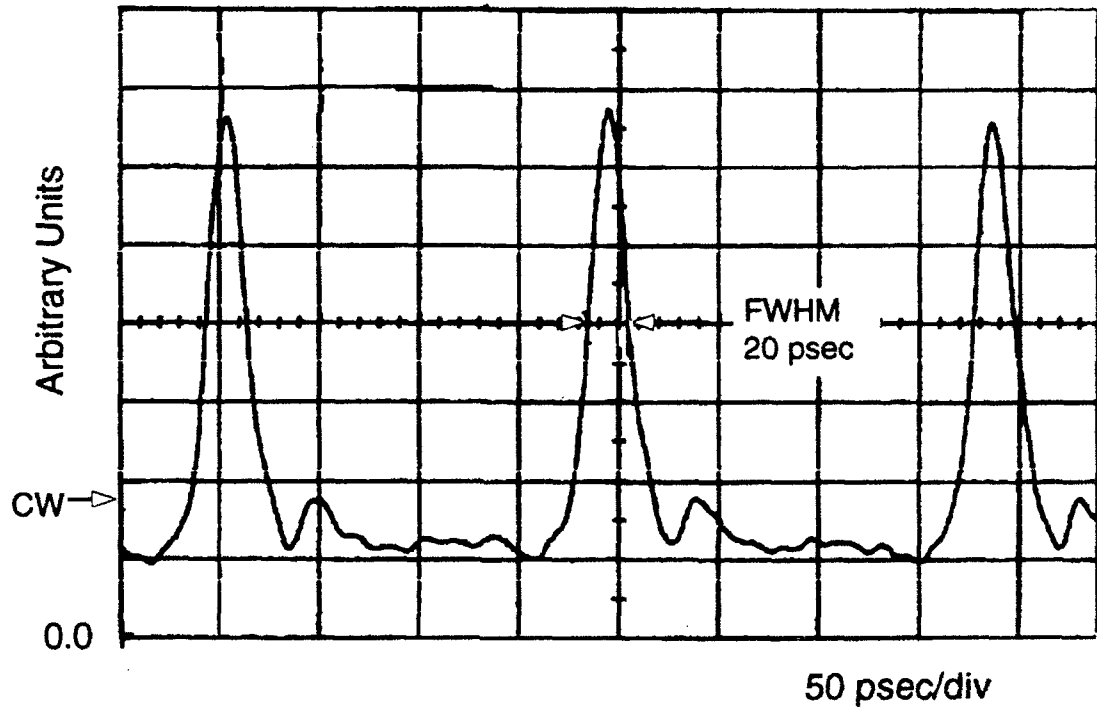


Figure 6.1 Pulses at 5.2 GHz, with some background light, as generated from a cw optical input. RF power = 1 W.

shown in Fig. 6.1, as measured by a fast photodiode [6.5] on a microwave transition analyzer [6.6]. The measured pulsewidth of 20 psec (FWHM) is limited by the photodiode response time. The actual pulsewidth is about 5.5 psec, as discussed next.

The electric field of the input cw light is  $E_0 \exp(j\omega_0 t)$ . After passing through the modulator (A radians at frequency  $\omega_m$ ) and the grating dispersion (Eq. 4.8, Sec. 4.1), the output electric field is given by,

$$E_o(t - \tau_0) = E_0 \exp j(\omega_0 t + \phi_0 - \omega_0 \tau_0) \sum_q J_q(A) \exp(jq\omega_m t) \exp(-jq^2 \omega_m^2 / 2\mu)$$

(6.1)

where  $\phi_0$  is a constant phase,  $\tau_0$  is the group delay, and  $\mu^{-1}$  is the group delay dispersion. The output intensity is given as,

$$I_o(t) = E_o(t)E_o^*(t)$$

$$I_o(t) = I_0 \left| \sum_q J_q(A) \exp(jq\omega_m t) \exp(-jq^2\omega_m^2/2\mu) \right|^2 \quad (6.2)$$

where  $I_0$  is the cw intensity. From Chapter 4, let  $\mu = g\omega_0/f_T = gA\omega_m^2$ , where  $g$  is a parameter close to one and  $g=1$  corresponds to the focal-time plane. Equation 6.2 is numerically evaluated for  $A = 12$  radians and  $\omega_m = 2\pi \times 5.2 \times 10^9$  rad/sec, corresponding to 1 W of microwave power. The parameter  $g$  is adjusted to maximize the peak intensity. The resulting waveform, for  $g = 0.77$ , is shown in Fig. 6.2. After accounting for the photodiode response time, this compares well with Fig. 6.1. Thus, the actual pulsewidth obtained is about 5.5 psec.

## 6.2 Temporal Focusing

In the next experiment active pulse compression, or focusing in time of a pulse, is demonstrated. The spatial analog of temporal focusing is well known. A beam passes through a lens and is focused in the transverse spatial coordinates after propagating about the focal-length of the lens. Forty-five psec (FWHM) gaussian pulses are available from a mode-locked Nd:YAG laser at a repetition rate of 82.6 MHz. The modulator is driven at its 5.2 GHz resonance by the 63rd harmonic of the pulse repetition frequency, using an external synthesizer phase-locked to the mode-locking synthesizer. The resonant-frequency-tuner, described in Sec. 5.3.2, is adjusted to match the resonant frequency

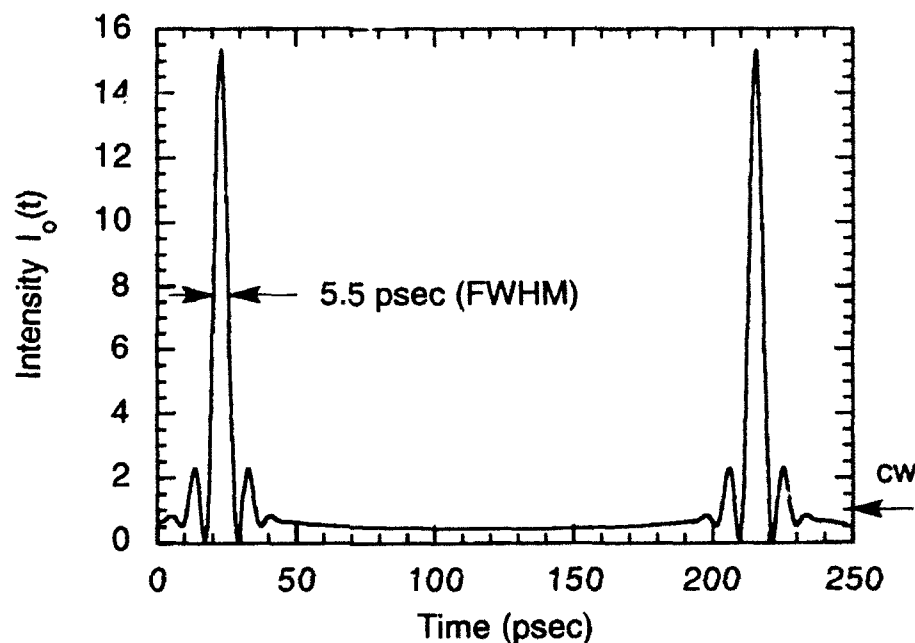


Figure 6.2 Theoretical calculation of pulses created from cw light.  $A = 12$  radians,  $\omega_m = 2\pi \times 5.2 \times 10^9$  rad/sec, and  $g = 0.77$ . Output normalized with cw intensity.

with the harmonic frequency. An adjustable microwave delay line is used to position the pulses in the center of the positive time-lens. This is again followed by a 4-pass grating dispersion adjusted to near the focal-time of the time-lens. Compressed (or focused) pulses are observed on an autocorrelator [6.7] and optimized by adjusting the dispersion and the microwave delay line. The autocorrelation trace obtained is shown in Fig. 6.3, with a fit [6.8] to a 6.7 psec (FWHM) gaussian pulse, for 1 W of microwave power. The incident pulsewidth (45 psec) is a little larger than the aperture of the time-lens (31 psec), leaving slight wings on the compressed pulse. Next, the microwave drive power is increased to 13 W at 10% duty cycle, using a traveling wave tube amplifier. The

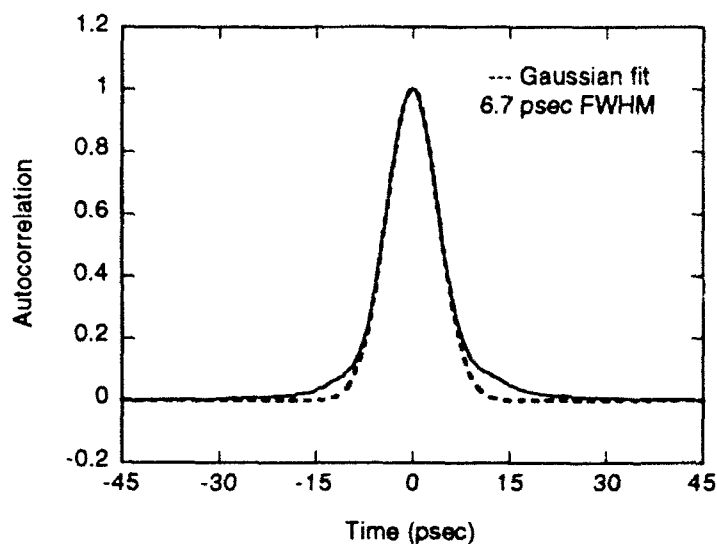


Figure 6.3 Autocorrelation trace of compressed pulse with fit to a 6.7 psec (FWHM) gaussian pulse. RF power = 1 W cw.

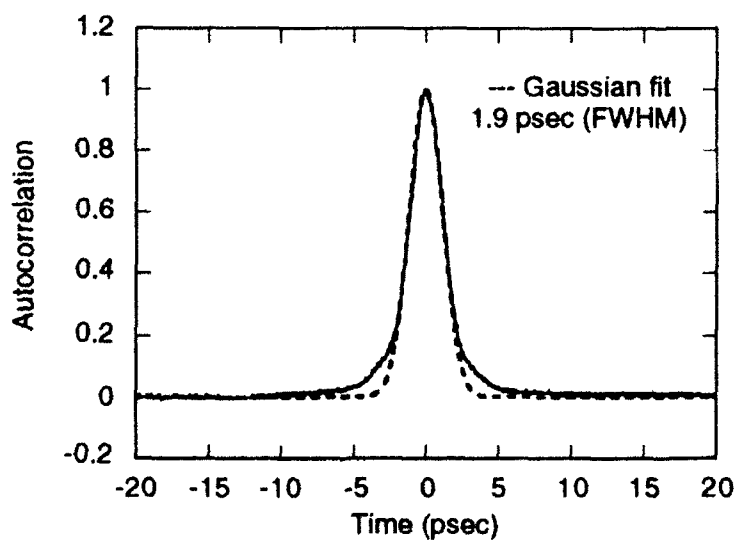


Figure 6.4 Autocorrelation trace of compressed pulse with fit to a 1.9 psec (FWHM) gaussian pulse. RF power = 13 W, 10% duty cycle.

dispersion after the time-lens is correspondingly reduced and optimized. The autocorrelation trace of the corresponding pulse with a fit [6.8] to a 1.9 psec gaussian pulse is shown in Fig. 6.4. Another application of this setup is the ability to tune the optical frequency of a mode-locked laser. By adjusting the microwave delay line, pulses can be positioned in the region of maximum positive or negative slope in the sinusoidal modulation curve, and hence the optical frequency is up-shifted or down-shifted respectively. This is experimentally demonstrated in Fig. 6.5, where a frequency shift of  $\pm 60$  GHz is obtained as expected.

If the aperture of the time-lens ( $1/\omega_m = 31$  psec) is completely filled, then the FWHM of the focused pulse, as discussed in Sec. 4.3, is given by  $\tau_0 = 2.77/A\omega_m$ . For 1 W microwave power,  $A = 12$  radians and hence  $\tau_0 = 7$  psec. At 13 W power,  $A = 43$  radians and hence  $\tau_0 = 1.97$  psec. This matches well with the experimental results, except for the deviation from a gaussian pulse. With an ideal lens, a gaussian is always focused to a gaussian. The incident pulsewidth of 45 psec is little larger than the defined aperture of the time-lens. This overfilling of the lens causes aberration and therefore the focused pulse deviates from a true gaussian. This can be analyzed numerically using ideas and equations from Chapter 4. The field distribution of a gaussian pulse of intensity FWHM  $\tau_p$  is given by

$$E_i(t) = \exp[-1.38(t/\tau_p)^2] \quad (6.3)$$

After passing through the sinusoidal modulator and the dispersion  $\mu^{-1}$ , the electric field of the focused pulse is given as

$$E_f(t) = \sqrt{\frac{\mu}{2\pi}} \int E_i(t') \exp(jA \cos \omega_m t') \exp[j \frac{\mu}{2}(t - t')^2] dt' \quad (6.4)$$

The intensity  $I_f(t)$  of the focused pulse is simply the absolute-square of the electric field.

The autocorrelation of the pulse is calculated as,

$$I_{AC}(t) = \int I_f(\tau) I_f(\tau + t) d\tau \quad (6.5)$$

Again let  $\mu = gA\omega_m^2$ , where  $g$  is a parameter close to one. Eqs. 6.3-6.5 are numerically evaluated and the parameter  $g$  is adjusted to maximize the peak intensity. The results for 1 W and 13 W power are shown in Figs. 6.6 and 6.7 respectively. The calculated autocorrelation traces agree well with measured ones.

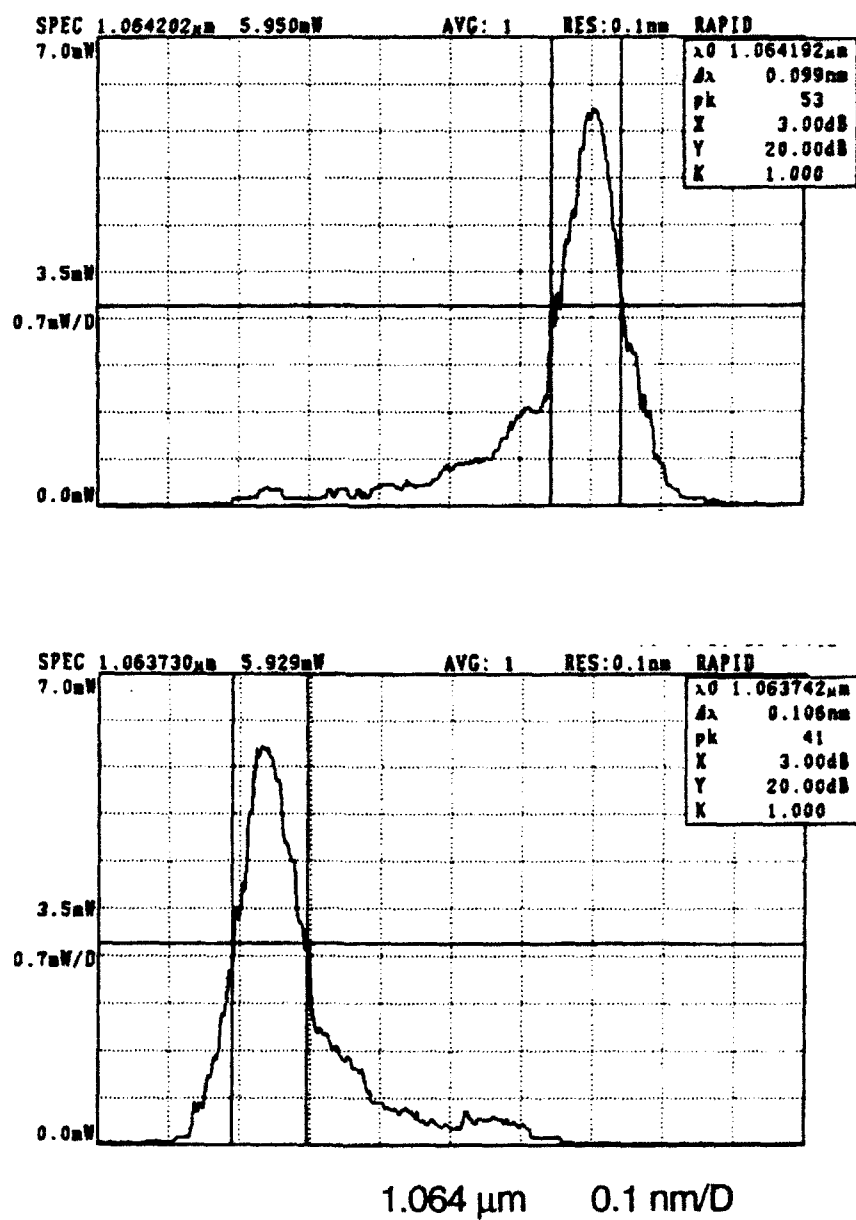


Figure 6.5 Up-shifting and down-shifting of the optical frequency of the mode-locked pulses using multipass microwave modulator. RF power = 1 W.



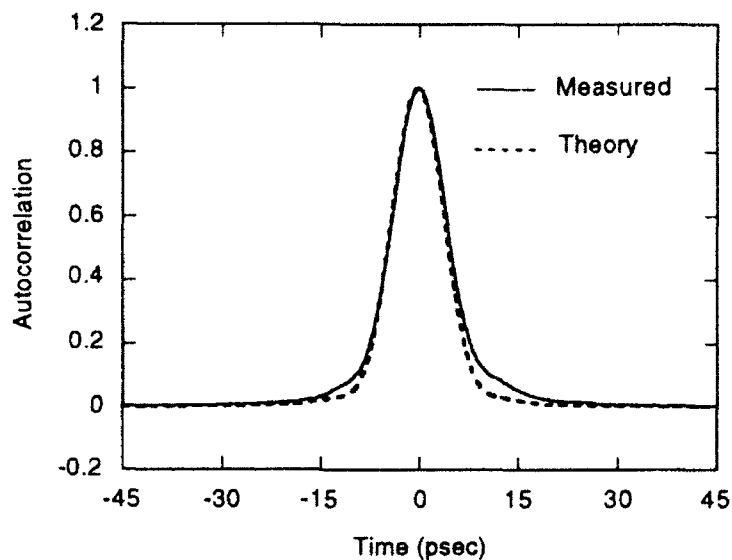


Figure 6.6 Comparison of measured and theoretically calculated autocorrelation traces. RF power = 1W,  $A = 12$  radians,  $g = 0.88$  and  $\tau_p = 45$  psec.

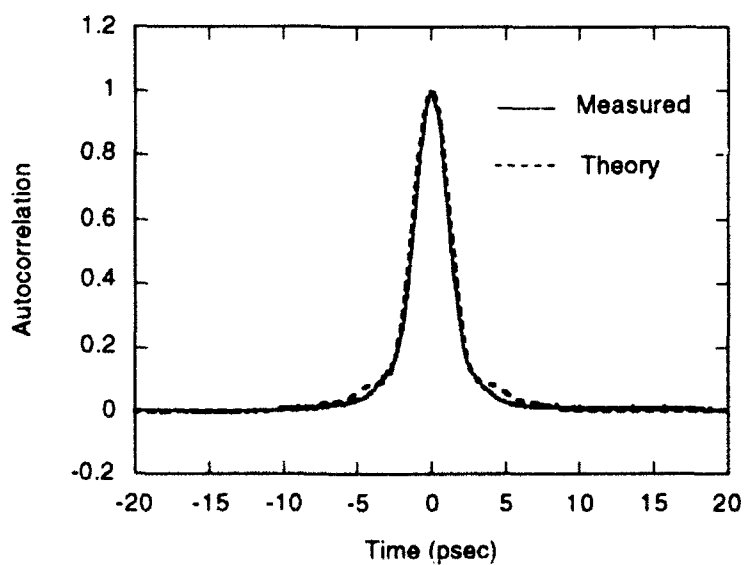


Figure 6.7 Comparison of measured and theoretically calculated autocorrelation traces. RF power = 13 W,  $A = 43$  radians,  $g = 0.91$  and  $\tau_p = 45$  psec.

## References

- 6.1 A. A. Godil, B. A. Auld, and D. M. Bloom, "Time-lens producing picosecond optical pulses," IEEE Lasers and Electro-optics Society Annual Meeting, Boston, MA, 1992.
- 6.2 A. A. Godil, B. A. Auld, and D. M. Bloom, "Time-lens producing 1.9 psec optical pulses," Submitted to *Appl. Phys. Lett.*
- 6.3 Lightwave Electronics, model 122, single-frequency Nd:YAG laser.
- 6.4 A. M. Johnson, R. H. Stolen, and W. M. Simpson, "80X single-stage compression of frequency doubled Nd:yttrium aluminum garnet laser pulses," *Appl. Phys. Lett.*, vol. 44, pp. 729-731, 1984.
- 6.5 New Focus Inc., model 1404, High speed photodiode.
- 6.6 Hewlett-Packard, model 70820A, Microwave transition analyzer.
- 6.7 Inrad, model 5-14B, Autocorrelator
- 6.8 J. M. Diels, J. J. Fontaine, I. C. McMichael, and F. Simoni, "Control and measurement of ultrashort pulse shapes (in amplitude and phase) with femtosecond accuracy," *Appl. Opt.*, vol. 24, pp. 1270-1282, 1985.

## Chapter 7    Summary & Future Directions

Dielectric resonators made from electro-optic crystals have been developed as microwave bulk-optic modulators. This device is called a DROM (dielectric resonator/optical modulator). A 20 GHz DROM in  $\text{LiNbO}_3$  was demonstrated with 0.1 radian of phase modulation at 1.06  $\mu\text{m}$  wavelength for 25 dBm of microwave power. The modulator was developed for harmonic mode-locking of a diode-pumped Nd:BEL laser. The laser cavity axial frequency was about 238 MHz and the DROM was operated on resonance at the 84th harmonic of that, about 20 GHz. Depending on the DROM drive frequency, two distinct regimes of mode-locking were observed: (1) 2.9 psec pulses at a repetition-rate of 238 MHz, (2) 3.9 psec pulses at a repetition-rate of 20 GHz. These are the shortest pulses yet reported for active mode-locking of a Nd laser. With 660 mW of diode pump incident on the BEL rod, about 50 mW average output power was obtained at 1.07  $\mu\text{m}$  wavelength. The DROM design presented in Chapter 2 can be easily scaled for 5-50 GHz operation. In addition, by simply choosing an orthogonal orientation of the c-axis of the  $\text{LiNbO}_3$ , the same design produces intensity modulation at twice the drive frequency in a single-mode optical system. Thus, with the ideas presented in Chapters 2 and 3, a solid-state laser can be actively mode-locked in the 100 MHz to 100 GHz regime.

Furthermore, this mode-locker can be applied to other laser materials, particularly ones with large gain bandwidths such as Ti:sapphire and Nd:glass.

In the second half of the thesis, space-time duality was discussed leading to the concept of temporal imaging. The well known analogy between Fresnel diffraction and first order temporal dispersion was recently extended to introduce the idea of a time-lens as a dual of a spatial lens (regular lens). The time-lens is simply a quadratic optical phase modulator in time, which was approximated by a portion of a sinusoidal phase modulator. Thus, by using phase modulators as lenses and grating pairs as dispersive elements, complete temporal imaging systems can be constructed in exact duality with spatial imaging systems. However, for practically useful time-lenses, considerable modulation is required at fairly high frequencies. This was addressed in Chapter 5 where a resonant microwave modulator was developed based on a LiNbO<sub>3</sub> loaded waveguide. Multiple passes were obtained through the modulator using an off-axis path in a stable optical resonator. At 5.2 GHz operation, 44 radians of phase modulation was obtained at 1.06  $\mu\text{m}$  wavelength for 13 W of microwave power. This corresponds to a time-lens with 31 psec aperture and 1.9 psec resolution. This was confirmed by demonstrating temporal focusing of 45 psec pulses to 1.9 psec, as presented in Chapter 6. By optimizing the design of the time-lens and better thermal engineering, it may be possible to obtain picosecond or sub-picosecond resolution. An attractive feature of temporal focusing is the suppression of timing jitter in the input pulse train. This can be easily understood by considering the space analog of timing jitter. The focused spot does not move by transversely displacing the input beam. This suppression of timing jitter needs to be experimentally characterized.

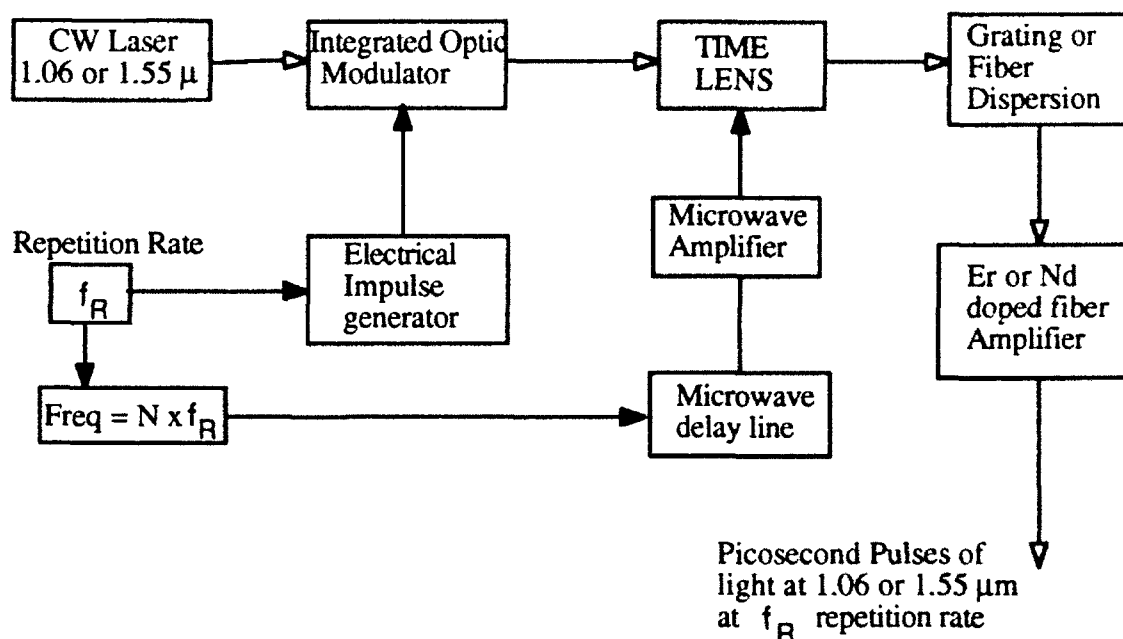


Figure 7.1 Block diagram of a system using temporal focusing to produce picosecond optical pulses at adjustable repetition rates.

The idea of temporal imaging and the technology of time-lenses, presented here, offer many exciting practical applications. A complete system can be engineered around temporal focusing to produce picosecond, and perhaps sub-picosecond, optical pulses in a clean stable way with adjustable repetition rates. A block diagram of such a system is shown in Fig. 7.1. The integrated optical modulator should be fast enough to chop slices of light of less than 50 psec duration. These slices are temporally focused with a time-lens and then amplified optically to boost the average power. The pulse repetition rate  $f_R$  can be adjusted continuously between DC and the maximum frequency-tuning of the resonator. Beyond that,  $f_R$  can only be adjusted discretely to a sub-harmonic of the microwave resonator frequency. This kind of a system can be very useful in test equipment for soliton communication systems. Another very interesting application of temporal imaging is time-

microscopy of fast optical events. The fastest commercially available photodiode and oscilloscope give a combined time response of about 15 psec. This can be extended to picosecond or less by combining with, as an example, a 30X temporal imaging system built around a picosecond or sub-picosecond resolution time-lens. This approach as an instrument can perhaps replace streak cameras. Imaging with one lens always produces an inverted image. In the time-domain this corresponds to time-reversal, which may have many applications in optical signal processing.